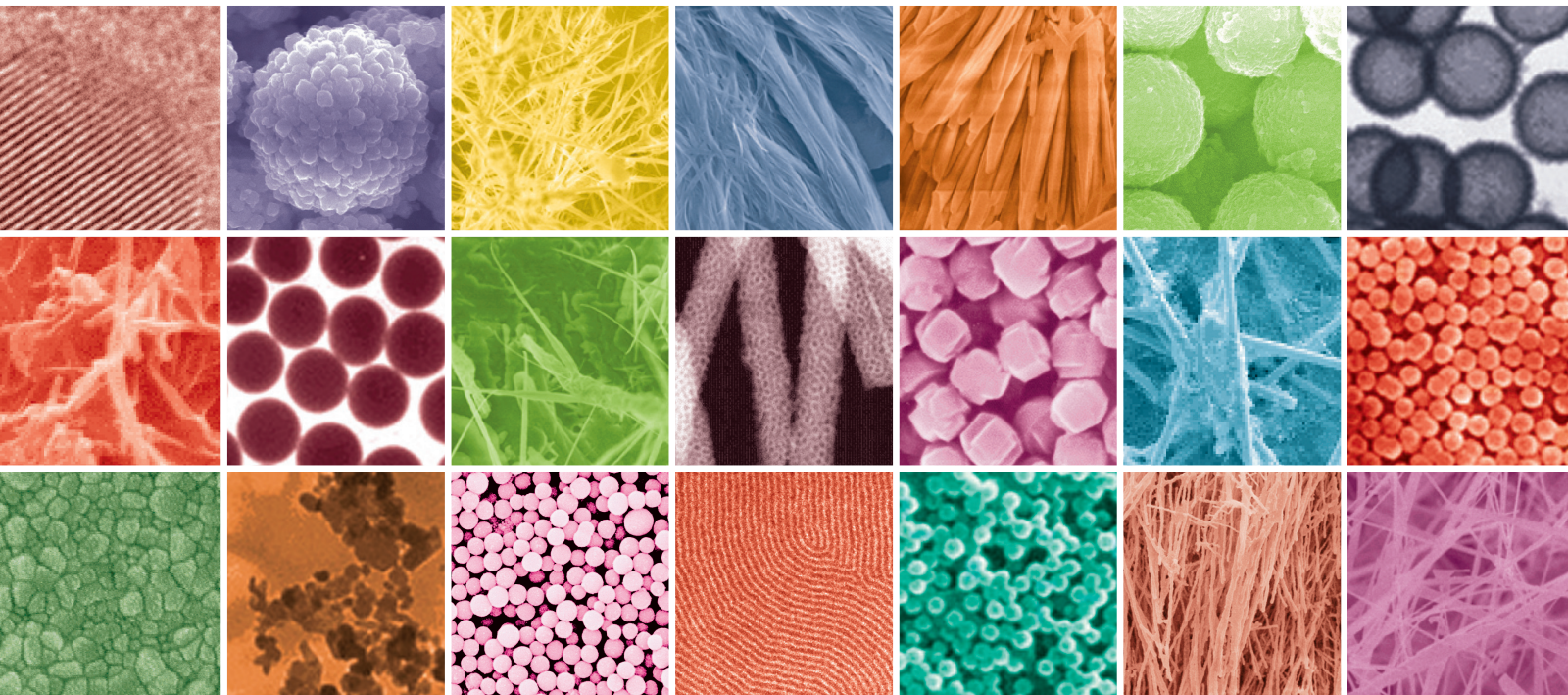


Nanostructured Magnetic Materials

Guest Editors: Weichang Hao, Ji Shi, Gang Xiang, and Yi Du





Nanostructured Magnetic Materials

Journal of Nanomaterials

Nanostructured Magnetic Materials

Guest Editors: Weichang Hao, Ji Shi, Gang Xiang, and Yi Du



Copyright © 2013 Hindawi Publishing Corporation. All rights reserved.

This is a special issue published in "Journal of Nanomaterials." All articles are open access articles distributed under the Creative Commons Attribution License, which permits unrestricted use, distribution, and reproduction in any medium, provided the original work is properly cited.

Editorial Board

- Katerina Aifantis, Greece
Nageh K. Allam, USA
Margarida Amaral, Portugal
Xuedong Bai, China
L. Balan, France
Enrico Bergamaschi, Italy
Theodorian Borca-Tasciuc, USA
C. Jeffrey Brinker, USA
Christian Brosseau, France
Xuebo Cao, China
Shafiul Chowdhury, USA
Kwang-Leong Choy, UK
Cui ChunXiang, China
Miguel A. Correa-Duarte, Spain
Shadi A. Dayeh, USA
Claude Estournes, France
Alan Fuchs, USA
Lian Gao, China
Russell E. Gorga, USA
Hongchen Chen Gu, China
Mustafa O. Guler, Turkey
John Zhanhu Guo, USA
Smrati Gupta, Germany
Michael Harris, USA
Zhongkui Hong, USA
Michael Z. Hu, USA
David Hui, USA
Y.-K. Jeong, Republic of Korea
Sheng-Rui Jian, Taiwan
Wanqin Jin, China
Rakesh K. Joshi, India
Zhenhui Kang, China
Fathallah Karimzadeh, Iran
Alireza Khataee, Iran
- Do Kyung Kim, Korea
Kin Tak Lau, Australia
Burtrand Lee, USA
Benxia Li, China
Jun Li, Singapore
Xing-Jie Liang, China
Shijun Liao, China
Gong Ru Lin, Taiwan
J.-Y. Liu, USA
Jun Liu, USA
Tianxi Liu, China
Songwei Lu, USA
Daniel Lu, China
Jue Lu, USA
Ed Ma, USA
Gaurav Mago, USA
Santanu K. Maiti, Israel
Sanjay R. Mathur, Germany
A. McCormick, USA
Vikas Mittal, UAE
Weihai Ni, Germany
Sherine Obare, USA
Atsuto Okamoto, Japan
Edward Andrew Payzant, USA
Kui-Qing Peng, China
Anukorn Phuruangrat, Thailand
Ugur Serincan, Turkey
Huaiyu Shao, Japan
Donglu Shi, USA
Suprakas Sinha Ray, South Africa
Vladimir Sivakov, Germany
Marinella Striccoli, Italy
Bohua Sun, South Africa
Saikat Talapatra, USA
- Nairong Tao, China
Titipun Thongtem, Thailand
Somchai Thongtem, Thailand
Valeri P. Tolstoy, Russia
Tsung-Yen Tsai, Taiwan
Takuya Tsuzuki, Australia
Raquel Verdejo, Spain
Mat U. Wahit, Malaysia
Shiren Wang, USA
Yong Wang, USA
Ruibing Wang, Canada
Cheng Wang, China
Zhenbo Wang, China
Jinquan Wei, China
Ching Ping Wong, USA
Xingcai Wu, China
Guodong Xia, Hong Kong
Zhi Li Xiao, USA
Ping Xiao, UK
Shuangxi Xing, China
Yangchuan Xing, USA
N. Xu, China
Doron Yadlovker, Israel
Ying-Kui Yang, China
Khaled Youssef, USA
William W. Yu, USA
Kui Yu, Canada
Haibo Zeng, China
Tianyou Zhai, Japan
Renyun Zhang, Sweden
Yanbao Zhao, China
Lianxi Zheng, Singapore
Chunyi Zhi, Japan

Contents

Nanostructured Magnetic Materials, Weichang Hao, Ji Shi, Gang Xiang, and Yi Du
Volume 2013, Article ID 492093, 2 pages

The Physical and Magnetic Properties of Electrodeposited Co-Fe Nanocoating with Different Deposition Times, Koay Mei Hyie, Wan Normimi Roslini Abdullah, Nor Azrina Resali, W. T. Chong, Z. Salleh, and M. A. A. Ghani
Volume 2013, Article ID 680491, 6 pages

The Effect of Reducing Time on the Magnetoresistance of Manganite $\text{La}_{0.67}\text{Sr}_{0.20}\text{Cu}_{0.10}\square_{0.03}\text{MnO}_3$ at a Temperature of 30°C, Hongwei Zhao, Lichun Hu, and Zhanxin Zhang
Volume 2012, Article ID 426037, 5 pages

Spin Waves Excitations of Co/Pt Multilayers, W. Zhou
Volume 2012, Article ID 496519, 4 pages

Magnetic Properties of Co-Fe-B Amorphous Films Thermomagnetically Treated with Different Field Directions, Zhe Liu, Weili Li, Weidong Fei, and Dan Xu
Volume 2012, Article ID 174735, 5 pages

Zinc Vacancy-Induced Room-Temperature Ferromagnetism in Undoped ZnO Thin Films, Hongtao Ren, Gang Xiang, Gangxu Gu, Xi Zhang, Wenjun Wang, Peng Zhang, Baoyi Wang, and Xingzhong Cao
Volume 2012, Article ID 295358, 5 pages

2D Simulation of $\text{Nd}_2\text{Fe}_{14}\text{B}/\alpha\text{-Fe}$ Nanocomposite Magnets with Random Grain Distributions Generated by a Monte Carlo Procedure, Nguyen Xuan Truong, Nguyen Trung Hieu, Vu Hong Ky, and Nguyen Van Vuong
Volume 2012, Article ID 759750, 7 pages

Synthesis, Characterization, and Microwave-Absorbing Properties of Polypyrrole/ MnFe_2O_4 Nanocomposite, Seyed Hossein Hosseini and Ahmad Asadnia
Volume 2012, Article ID 198973, 6 pages

Temperature-Driven Spin Reorientation Transition in CoPt/AlN Multilayer Films, Wupeng Cai, Shinji Muraishi, Ji Shi, Yoshio Nakamura, Wei Liu, and Ronghai Yu
Volume 2012, Article ID 814162, 7 pages

Electronic Structure of $\text{BiFe}_{1-x}\text{Mn}_x\text{O}_3$ Thin Films Investigated by X-Ray Absorption Spectroscopy, Abduleziz Ablat, Emin Muhemmed, Cheng Si, Jiaou Wang, Haijie Qian, Rui Wu, Nian Zhang, Rong Wu, and Kurash Ibrahim
Volume 2012, Article ID 123438, 7 pages

Effects of Annealing Temperature on Structure and Magnetic Properties of $\text{Tb}_x\text{Y}_{3-x}\text{Fe}_5\text{O}_{12}$ ($x = 0.2$ and 0.4) Thin Films, N. B. Ibrahim, Ftema W. Aldbea, and Mustaffa Hj Abdullah
Volume 2012, Article ID 154192, 5 pages

Dilute Magnetic Semiconductor $\text{Cu}_2\text{FeSnS}_4$ Nanocrystals with a Novel Zinblende Structure, Xiaolu Liang, Xianhua Wei, and Daocheng Pan
Volume 2012, Article ID 708648, 5 pages

Editorial

Nanostructured Magnetic Materials

Weichang Hao,¹ Ji Shi,² Gang Xiang,³ and Yi Du⁴

¹ Centre of Materials Physics and Chemistry, Beihang University, Beijing 100191, China

² Department of Metallurgy and Ceramics Science, Tokyo Institute of Technology, Tokyo 152-8552, Japan

³ Department of Physics, Sichuan University, Chengdu 610064, China

⁴ Institute for Superconducting & Electronic Materials, University of Wollongong, Wollongong, NSW 2522, Australia

Correspondence should be addressed to Weichang Hao; whao@buaa.edu.cn

Received 20 January 2013; Accepted 20 January 2013

Copyright © 2013 Weichang Hao et al. This is an open access article distributed under the Creative Commons Attribution License, which permits unrestricted use, distribution, and reproduction in any medium, provided the original work is properly cited.

The saga of nanostructured magnetic materials (NMMs) has prevailed since the discovery of the first giant magnetoresistance (GMR) effect in metals in 1988. NMMs represent a unique system that incorporates the interplay between the properties associated with spin degrees of freedom and the nanoscaled structures, which provide a very strong platform for exploring both basic science and technical applications in the fields of solid-state physics, chemistry, materials science, and engineering. In fact, an active research field called “spintronics,” which has a big overlap with NMMs, has emerged and prevailed very recently. Through manipulation of spin of electrons in solids, a wide variety of NMMs and devices have been playing a prominent role in information processing and transport in our modern life. A rich variety of materials, such as transition metals, manganite, wide bandgap semiconductors, and nanocomposites, have already been developed for generating well-controlled nanostructures with new functionalities. Many scientists believe that the 21st century will be a “Century of Spin.” Nanomaterials and nanotechnologies have provided historical opportunities for research and development of novel spintronics materials and devices. NMMs manifest fascinating properties compared to the bulks because of size effect and quantum effect. Nanotechnologies have been proven to be an effective way to fabricate devices with fine nanostructures. The combination of spintronics and nanomaterials will undisputedly open new pathways in solid-state physics. The present special issue focuses on the recent development in the understanding of the synthesis, the studies on magnetic properties of nanostructures, and their potential applications based on the multiple functionalities.

In this special issue, we have a series of contributed papers that are addressing current status of the fundamental issues related to different NMMs, from either experimental or theoretical points of view. The front edge and hot spot of materials science and condensed matter physics, dilute magnetic semiconductors (DMSs), has been covered: X. Liang et al. demonstrated a successful synthesis and characterization of DMS $\text{Cu}_2\text{FeSnS}_4$ nanocrystals with a novel zinc blende structure; G. Xiang’s group spotlighted the wide bandgap semiconductor ZnO nanocrystals and discovered that the zinc vacancies themselves could induce ferromagnetism in undoped ZnO at room temperature. Some of the papers illustrate the research on the manganite: A. Ablat et al.’s paper studied the electronic structures of multi-ferroic $\text{BiFe}_{1-x}\text{Mn}_x\text{O}_3$ using X-ray absorption spectroscopy; H. Zhao et al. demonstrated the effect of reducing time on the colossal magnetoresistance of $\text{La}_{0.67}\text{Sr}_{0.20}\text{Cu}_{0.10}\text{Mn}_{0.10}\text{O}_3$. In the meantime, some of the papers cover the traditional transition-metal-based nanostructures: the paper by W. Zhou investigated the optically excited spin waves in traditional transition metal systems (Co/Pt nanostructures); K. M. Hyie et al.’s paper studied the influence of deposition time on the magnetic properties of Co-Fe nanostructures; W. Li’s group spotlighted the effect of thermomagnetic treatment on the magnetic properties of Co-Fe-B systems. N. B. Ibrahim et al. reported the synthesis and magnetic property characterization of Tb-YIG. The remaining papers illustrate nanocomposite systems; S. H. Hosseini and A. Asadnia studied the synthesis and microwave absorbing properties of polypyrrole/ MnFe_2O_4 nanocomposite; N. X. Truong et al.’s paper demonstrated a theoretical simulation of magnetic

properties of $\text{Nd}_2\text{Fe}_{14}\text{B}/\alpha\text{-Fe}$, revealing the importance of the details of microstructures; W. Cai et al. studied the nanoscaled heterostructures based on transition metals and wide bandgap semiconductors (CoPt/AlN) and illustrated that the spin reorientation transitions could be caused by anisotropy variations driven by temperature change.

Acknowledgments

We would like to express our sincere appreciation to all the authors and coauthors and all the reviewers for their contribution to this special issue. We also thank the reviewers for their time and valuable comments.

Weichang Hao
Ji Shi
Gang Xiang
Yi Du

Research Article

The Physical and Magnetic Properties of Electrodeposited Co-Fe Nanocoating with Different Deposition Times

Koay Mei Hyie,¹ Wan Normimi Roslini Abdullah,¹ Nor Azrina Resali,¹
W. T. Chong,² Z. Salleh,¹ and M. A. A. Ghani¹

¹ Faculty of Mechanical Engineering, Universiti Teknologi MARA, Selangor, 40450 Shah Alam, Malaysia

² Department of Mechanical Engineering, Faculty of Engineering, University of Malaya, 50603 Kuala Lumpur, Malaysia

Correspondence should be addressed to Koay Mei Hyie; hyie1105@yahoo.com

Received 11 June 2012; Revised 15 December 2012; Accepted 19 December 2012

Academic Editor: Weichang Hao

Copyright © 2013 Koay Mei Hyie et al. This is an open access article distributed under the Creative Commons Attribution License, which permits unrestricted use, distribution, and reproduction in any medium, provided the original work is properly cited.

Using the electrodeposition process, cobalt-iron (Co-Fe) nanocrystalline coatings were successfully synthesized onto stainless steel in deposition times of 30, 60, and 90 minutes. The temperature used throughout the process was 50°C in an acidic environment of pH 3. By changing the deposition time, physical properties such as phase and crystallographic structure, surface morphology, grain size, microhardness, and magnetic properties of Co-Fe coatings were examined. FESEM micrographs showed that the grain sizes of the coatings were in the range from 57.9 nm to 70.2 nm. Dendrite and irregular shapes were found in the microstructure of Co-Fe nanocoating. The Co-Fe nanocrystalline coating prepared in a deposition time of 90 minutes achieved the highest microhardness of 339 HVN. The magnetic properties associated with Co-Fe nanocoating at longer deposition times show greater coercivity, H_c , and saturation magnetization, M_s , values of 56.43 Oe and 70.45 μg , respectively. The M-H curves for all the Co-Fe coatings exhibited soft ferromagnetic behaviour with narrow hysteresis loops. It was found that increasing the deposition time also improved the microhardness and magnetic properties of Co-Fe nanocoating, which is much needed for long-life high-coercivity magnetic strip card applications.

1. Introduction

Nanoparticles are ultrafine particles with a diameter less than 100 nm which are fundamental in nanocrystalline materials. These materials exhibit enhancing properties, that is, physical, chemical, and mechanical, resulting from a reduction of grain size and existence of interphase within the grain boundaries of the microstructure [1, 2]. Electrodeposition is a viable, low-cost process in synthesizing the nanomaterials. It can be used on metals, alloys, polymers, and composites [3]. It can also produce coatings on various substrates requiring higher deposition rates [4]. Electrodeposition is also suitable for any industrial application since it can produce deposits for restricted areas such as tiny parts in machines or any equipment. In electrodeposition, the properties of the nanocrystalline materials can be improved along with their microstructure being controlled by optimizing the operating parameters such as deposition time, pH, bath temperature, direct current density, and electrolytic composition. A diverse

range of applications has resulted in the interest for nanoparticles with a wide range of magnetic properties. The study of magnetic properties for softer magnetic materials has gained interest among the researchers due to their potential in the manufacturing of components for microelectromechanical system (MEMS) [5]. In magnetic data storage applications, ferromagnetic nanoparticles with a high coercivity, H_c , and saturation magnetization, M_s , is explored for high-density magnetic media such as magnetic recording write heads [6–8]. The magnetic properties such as M_s and H_c of soft magnetic materials are very important to be studied in order to evaluate the performance of those soft magnetic materials.

Previous findings have reported on the magnetic properties, M_s and H_c , of Co-Fe alloys in relation to their different alloy compositions in electrolytes [9]. It was found that the values of M_s and H_c increased linearly with additional contents of Fe. The increase in the M_s value was correlated to the crystal structure or phases of the films. The coexistence of both Co-Fe face-centred cubic (FCC) and Co-Fe

body-centred cubic (BCC) phases in the microstructure was possibly caused by higher M_s values as the Fe content was increased. Additionally, initial research works reported that, for nanocrystalline materials, there was a large reduction in M_s with decreasing grain size [10]. Reference [10] stated a 40% decrease in M_s for nanocrystalline Fe compared to its bulk polycrystalline Fe. It was then concluded that the reduction in M_s was attributed to the differences in the magnetic microstructure between nanocrystalline and conventional polycrystalline Fe.

Other previous paper work reviewed the size effects in nanocrystalline metals and alloys made by electroforming, a particular form of electrodeposition [11]. The main size effects in these nanocrystalline materials came from grain size reduction down to less than 5 nm and down towards the limit of the amorphous structure. Fully dense nanocrystalline metals and alloys have unique microstructures consisting of nanometre-sized crystals and large volume fractions of grain boundary and triple junction defects. It has been shown that several properties such as Young's modulus, thermal expansion, and saturation magnetization were not greatly affected by the presence of high concentrations of these defects. In contrast, properties that depend on the interactions of intercrystalline defects with other structural characteristics such as dislocations, precipitates, and electrons show significant grain size effects. These include hardness, wear resistance, electrical resistivity, and coercivity. In addition, the introduction of structural disorder by grain boundaries and triple junction had an insignificant effect on M_s compared with the chemical disorder introduced by additional alloying [12].

The study on the characterization and magnetic properties of electrodeposited Co-Fe alloys with a citrate stabilized sulphate bath was reported elsewhere in relation to the plating conditions and structure parameters [13]. The influence of ammonium citrate dosage, Fe content, and plating temperature was investigated in relation to magnetic properties. A lower value of H_c (10 Oe) was obtained with a low dosage of citrate bath (2–20 g/L) due to the low stress in Co-Fe film [14]. The value of H_c of the deposited film decreased as the Fe content reached the minimum requirement of approximately 40 atomic% Fe. However, the H_c value slowly rose as the Fe content increased from the minimum content. Similarly, the H_c value became greater with increments in the plating temperature. An increase in deposition temperature was most likely due to an increase in deposit grain size, which should have increased the H_c value. The H_c is directly proportional to the deposited grain size [15]. The composition of Co-Fe film with high Fe content and less Co content produced the best soft magnetic properties— H_c value of 17 Oe, which is still acceptable, and an M_s value of 2.04 T, which is quite good. The addition of ammonium citrate in the deposition bath was believed to have not sacrificed the magnetic properties of the Co-Fe films. The lowest H_c value of 10 Oe, which was obtained in a low dosage of ammonium citrate, corresponded to a mixture of FCC and BCC phases with BCC phase denominating. The optimal soft magnetic properties of lower H_c and higher M_s were produced when both phases, BCC and FCC were codeposited in the Co-Fe microstructure. This is

TABLE 1: Molar concentration of precursors in the electrolyte composition for the synthesis of Co-Fe nanocoating.

Precursor	Molar concentration, molarity (M)
CoSO ₄	0.075
FeSO ₄	0.03
H ₃ BO ₃	0.4
Sodium saccharine	0.01

due to the crystallization competition between the BCC and FCC phases which led to the reduction in grain size [15].

Thus, in this research work, the synthesis of Co-Fe nanocoatings using electrodeposition method on stainless steel substrate was reported. The physical and magnetic properties of as-synthesized Co-Fe deposits were investigated in relation to the different deposition times of 30, 60, and 90 minutes.

2. Experimental Work

The electrolyte used in the electrodeposition process was a mixture of CoSO₄, FeSO₄, and H₃BO₃ with an organic additive of saccharine [16]. Table 1 represents the molar concentration of the precursors in the bath composition. The Co-Fe coatings were deposited on the stainless steel substrate while a graphite electrode was used as the anode. A Co-Fe nanocrystalline was deposited with a flow of direct current of density 0.08 A/cm². The pH of the electrolyte was maintained at 3.0. The Co-Fe coatings were formed in 30-, 60- and 90-minute deposition times. All the operating parameters such as temperature, pH, direct current density, and deposition time during the electrodeposition process were controlled and maintained. Each experiment was carried out with a freshly prepared solution. The equipment used to test the characteristics of as-synthesized Co-Fe coatings were ULTIMA IV FD 3668N, X-ray diffractometer (XRD), and JEOL JSM-7600F, a Field Emission Scanning Electron Microscope (FESEM). Hardness of the coating sample was measured with a MITUTOYO MVK-H1, Vickers Microhardness Tester using a load of 200 gm. The Alternating Gradient Magnetometer, AGM (Model 2900) was used to determine the magnetic properties of Co-Fe coatings. Figure 1 illustrates the schematic diagram of the electrodeposition process for the synthesis of Co-Fe nanocoating.

3. Results and Discussion

3.1. Phase and Crystallographic Structure Characterization. XRD measurements of as-synthesized Co-Fe coatings were carried out from 30° to 100° 2θ angle. Figure 2 shows the XRD patterns of the electrodeposited Co-Fe coatings at different deposition times of 30, 60, and 90 minutes. The XRD spectrum for the Co-Fe phase reveals the characteristic peaks at 2θ angles of 45°, 65°, and 83°. The peaks correspond to (110), (200), and (211) planes. The Co-Fe phase is identified as the BCC crystal structure with JCPDS no. 10717173. Observing the XRD spectrum for pure cobalt during depositions of 30 and 60 minutes, the Co phase was observed at 2θ angles

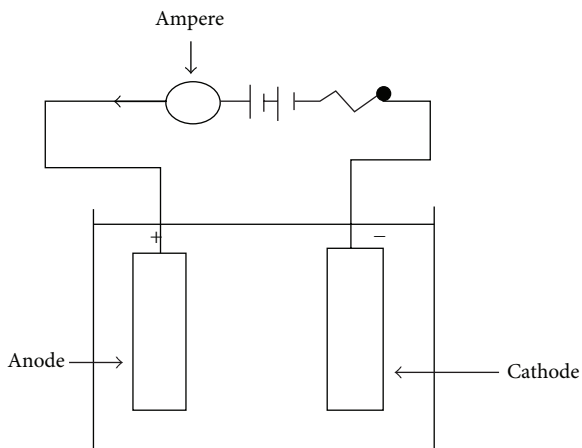


FIGURE 1: Schematic diagram of electrodeposition process.

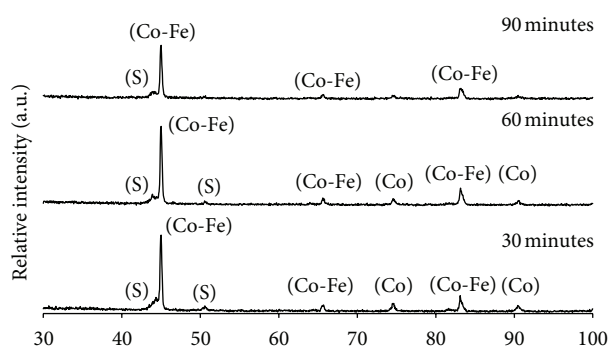


FIGURE 2: X-ray diffraction patterns for three Co-Fe nanocoatings obtained in 30-, 60-, and 90-minute depositions.

of 75° and 91° with (110) and (200) planes, respectively. Pure Co phases have the hexagonal close packed (HCP) crystal structure similar with JCPDS no. 50727.

Sulphur (S) peaks were observed in all Co-Fe XRD patterns prepared in three deposition times. The S peaks, which are indexed at 2θ angles of approximately 44° and 51° , have the respective corresponding planes of (2210) and (266). S phases have similar orthorhombic crystal structure as with JCPDS no. 80247. As for 90-minute depositions; the S phase reveals a characteristic peak at 2θ angle of 51° which disappeared and left only one S phase at 44° .

Saccharine when used as an organic additive in the electrodeposition process of Co-Fe nanocoating was the main source for the S element in the microstructure. The incorporation of the S element in the Co-Fe microstructure is believed to have occurred due to the two independent mechanisms. There are saccharine electroreduction and physical incorporation of saccharine molecules during the deposit growth. This incorporation of S elements in the Co-Fe microstructure was also reported in [17]. Referring to Figure 2, the peak of pure Co is fully dissolved in a 90-minute deposition which showed that the Co-Fe phase was completely formed.

3.2. Surface Morphology Characterization. Figure 3 shows the granular structure of Co-Fe coatings in three different deposition times: 30, 60, and 90 minutes. All Co-Fe coatings have dendritic and irregular microstructures. The grains resemble the pine tree-like shape which is known as dendrite, meaning branching. Secondary dendrite arms branch off the primary arm and tertiary arms off the secondary arms, and so forth. The formation of dendrite occurs because the grains are developed in defined planes due to the created crystal lattice [18]. The dendritic microstructure which contains Co-rich content is mostly found in the Co-Fe coating that was deposited for 30 minutes. This was due to the existence of pure Co phases compared to the other deposition times. This is in agreement with the XRD results. The oriented-attachment mechanism is assumed to have occurred in Co-Fe nanoparticle microstructures which caused the formation of dendritic microstructures [19]. In contrast, the majority of the microstructure area in the 90-minute deposition was overwhelmed with the existence of a greater number of irregular grains. These irregular grains are merely grains without a smooth surface because its growth was impeded by contact with another grain or boundary surface. The interface formed between grains is called the grain boundary. The atoms between the grains at the grain boundaries have no crystalline structure and are arranged in a disordered fashion [18]. In conclusion, the presence of irregular grains in the microstructure develops an interface between grain boundaries. Whereas, the grains with dendritic morphology have developed pine tree-like shapes in the microstructure, each with branches that have defined crystal planes.

The average grain sizes decreased from 70.2 nm to 57.9 nm with deposition times increasing. It is believed that there is insufficient time for the grains to distribute and therefore leave certain substrate areas empty in the microstructure of Co-Fe nanocoating for 30-minute depositions. The phenomenon has led to the creation of underdeveloped dendritic structures and bigger grain size due to the distribution of the Co-Fe atoms being mostly inside the grains compared to the grain boundaries. Agglomeration and grain growth tend to happen in 60-minute depositions as shown in the Figure 3(b). The atoms in the microstructure are fused, combining with each other and producing larger grains. Meanwhile, the irregular grains are smaller in FESEM micrographs of 90-minute electrodepositions compared to 30- and 60-minute depositions as shown in Figure 3(c).

In the 90-minute deposition, the Co-Fe atoms have ample time for rearranging themselves in the microstructure as compared to other's deposition times. For the rearrangement of atoms occurring in 90-minute depositions, a large amount of Co-Fe atoms have the opportunity to be located around the grain boundaries with a more complicated and disorderly manner. There are restrictions in their arrangement imposed by the adjacent crystal lattice of disoriented grains in the microstructure [20]. These Co-Fe atoms are arranged with a variety of interatomic spacing differing from boundary to boundary [2]. Furthermore, a greater number of grain boundaries with the highest proportion of atoms inside the boundaries have created an extremely high fractional volume

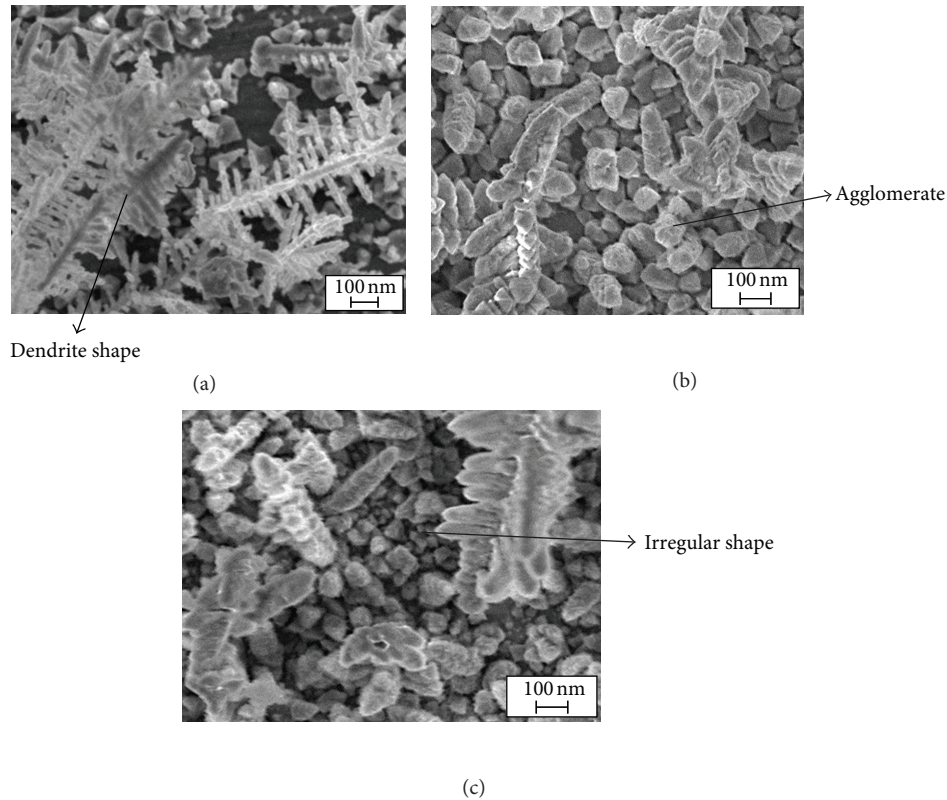


FIGURE 3: FESEM micrographs of Co-Fe nanocoatings deposited in (a) 30, (b) 60, and (c) 90 minutes.

of grain boundary phases in the Co-Fe microstructure. Therefore, a greater volume fraction of grain boundary phases has developed the fully compact and dense Co-Fe microstructure which has resulted in a reduction in grain size and enhanced properties from the bulk materials. In addition, the Co-Fe microstructure is also believed to be fully completed in this deposition time since there is no presence of pure Co phases in the microstructure as can be seen in the XRD result. As a conclusion, higher proportion of boundary atoms in grain boundaries compared to those inside the grains has created the fully dense and compact microstructure. These high volume fractions of grain boundaries lead to the reduction of grain size.

3.3. Microhardness Measurement. The microhardness measurements were taken from an average of 10 measurements using a 200 gm load. The microhardness values of as-synthesized Co-Fe coated samples in 30-, 60-, and 90-minute depositions were 287, 291, and 339 HVN, respectively, as shown in Figure 4. The highest microhardness was found at a deposition time of 90 minutes. This was with the smallest grain size (57.9 nm) and had an existence of structure compactness and grain boundaries in the coating microstructure. This is in parallel with the FESEM result. Moreover, the existence of these grain boundaries prevents the dislocation motion by changing the direction or stopping the movement of the dislocation. Consequently, the change in the dislocated direction movement results in a harder material. This result

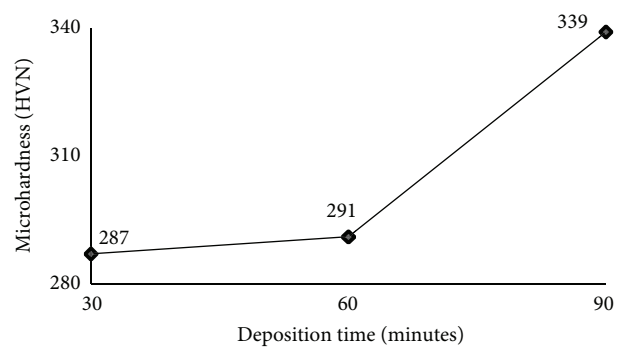


FIGURE 4: The average microhardness of Co-Fe coatings at different deposition times of 30, 60, and 90 minutes.

is consistent with [21]. It can be concluded that as the deposition time increases, the average microhardness of the Co-Fe coatings increases.

3.4. Magnetic Properties. Figure 5 shows the magnetic properties of as-synthesized Co-Fe coatings at different deposition times of 30, 60, and 90 minutes in M-H hysteresis loops. The M-H curve of Co-Fe coatings passes the origin of the graph. All the M-H curves illustrate that the electrodeposited Co-Fe coatings exhibit the soft ferromagnetic behaviour due to the presence of narrow and smaller well-defined hysteresis loop areas which can be seen in Figure 4. This similar finding

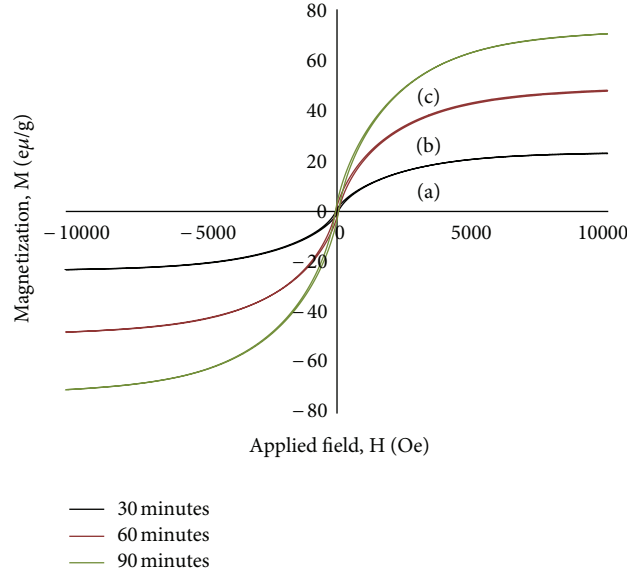


FIGURE 5: M-H hysteresis loops of Co-Fe nanocoatings prepared in deposition times of (a) 30, (b) 60, and (c) 90 minutes.

TABLE 2: The magnetic properties of electrodeposited Co-Fe coatings in three different deposition times.

Deposition time (minutes)	M_s ($e\mu/g$)	H_c (Oe)
30	22.99	42.56
60	47.87	52.67
90	70.45	56.43

was reported in [22]. The Co-Fe nanoparticles in 90-minute depositions show a broader hysteresis loop area compared to the other samples indicated by the higher M_s value.

The magnetic properties of electrodeposited Co-Fe coatings for different deposition times are tabulated in Table 2. The M_s of Co-Fe coating increases with longer deposition times from 22.99 to 70.45 $e\mu/g$. This increase in M_s value can be explained by the change in grain shape from dendritic to irregular for longer deposition times [5]. The highest proportion of the irregular grains in the 90-minute deposition of the Co-Fe nanocoating developed a compact and fully dense microstructure with smaller grain sizes. The reduced grain size and structure compactness have resulted from a high volume of disorderly arranged atoms in the grain boundaries as compared to the grains themselves. This phenomenon has led to the increase of M_s [23]. The formation of a compact dendritic morphology in the crystallized Co-Fe-based alloy was believed to have given an undesirable effect towards the soft magnetic properties [24].

The value of H_c was found to be greater with the grain size reducing as deposition times increased. The increase of H_c is usually influenced by larger grain sizes [23] but was not consistent with the results of this research. Additionally, based on research work taken from [25, 26], low H_c was found in the Co-Fe FCC + Co-Fe BCC region. However, in 30-minute depositions, low H_c value cannot be related to the creation of combined FCC + BCC phases since Co-Fe

phases exhibit pure BCC crystal structures. Therefore, further research should be conducted to investigate this phenomenon of H_c increment.

4. Conclusion

The Co-Fe phase in the Co-Fe coatings has a BCC crystal structure. Morphology studies reveal that the granular structure of Co-Fe coatings consist of a dendritic and irregular microstructure. The average grain size for all Co-Fe coatings is between 57.9 nm and 70.2 nm with the smallest grain size being noted in a deposition time of 90 minutes. The smallest grains produced the highest microhardness of 339 HVN. The mechanical properties of microhardness are not affected by the presence of phases in the Co-Fe microstructure. On the other hand, this mechanical property is closely correlated to the reduction in grain size and interactions of intercrystalline defects, that is, grain boundaries with other structural characteristics which include dislocations in the Co-Fe microstructure.

All the Co-Fe coatings show soft ferromagnetic behaviour with narrow hysteresis loops. The M_s and H_c are increased as the deposition time increases. M_s of electrodeposited ferromagnetic materials such as Co-Fe nanocoating are generally independent of electroplating conditions. It is only dependent on film compositions (Fe and Co content), phases and crystallographic structures (BCC phase), and surface morphologies (irregular and dendritic structures) in the microstructure. Usually, H_c values are directly proportional to the grain size and are affected by the presence of intercrystalline defects of grain boundaries and triple junctions. The best optimal magnetic properties which have reduced H_c and higher M_s are related to the coexistence of Co-Fe BCC and FCC phases in the microstructure. However, in this research, with the existence of only pure Co-Fe BCC phases, higher M_s and H_c values were found during depositions times of 90 minutes.

Effects on grain size reduction are directly proportional to the increase of M_s and H_c . It is suggested that the nanocrystalline Co-Fe coatings prepared at 90 minutes produce better H_c and hardness due to smaller grain size.

Acknowledgments

Financial supports from the Fundamental Research Grant Scheme (600-RMI/FRGS 5/3 (55/2012)) and the Universiti Teknologi Mara (UiTM) Excellent Fund (600-RMI/ST/DANA 5/3/Dst (373/2011)) and (600-RMI/ST/DANA 5/3/Dst (491/2011)) are gratefully acknowledged.

References

- [1] C. Suryanarayana and C. C. Koch, "Nanocrystalline materials—current research and future directions," *Hyperfine Interactions*, vol. 130, no. 1–4, pp. 5–44, 2000.
- [2] C. Suryanarayana, "Nanocrystalline materials," *International Materials Reviews*, vol. 40, no. 2, pp. 41–64, 1995.
- [3] I. Gurrappa and L. Binder, "Electrodeposition of nanostructured coatings and their characterization—a review," *Science and Technology of Advanced Materials*, vol. 9, no. 4, Article ID 043001, 11 pages, 2008.
- [4] U. S. Mohanty, "Electrodeposition: a versatile and inexpensive tool for the synthesis of nanoparticles, nanorods, nanowires, and nanoclusters of metals," *Journal of Applied Electrochemistry*, vol. 41, no. 3, pp. 257–270, 2011.
- [5] N. V. Myung, D. Y. Park, P. T. A. Sumodjo, and B. Y. Yoo, "Development of electroplated magnetic materials for MEMS," *Journal of Magnetism and Magnetic Materials*, vol. 265, no. 2, pp. 189–198, 2003.
- [6] P. Tartaj, M. P. Morales, S. Veintemillas-Verdaguer, T. González-Carreño, and C. J. Serna, "The preparation of magnetic nanoparticles for applications in biomedicine," *Journal of Physics D*, vol. 36, no. 13, pp. R182–R197, 2003.
- [7] H. Chiriac, A. E. Moga, and C. Gherasim, "Preparation and characterization of Co, Fe and Co-Fe magnetic nanoparticles," *Journal of Optoelectronics and Advanced Materials*, vol. 10, no. 12, pp. 3492–3496, 2008.
- [8] X. Liu, P. Evans, and G. Zangari, "Electrodeposited Co-Fe and Co-Fe-Ni alloy films for magnetic recording write heads," *IEEE Transactions on Magnetics*, vol. 36, no. 5, pp. 3479–3481, 2000.
- [9] S. H. Teh and I. I. Yaacob, "Synthesis and characterization of Co-Fe nanocrystalline magnetic films electrodeposited from electrolyte solution containing sodium saccharin," *IEEE Transactions on Magnetics*, vol. 47, no. 10, pp. 4398–4401, 2011.
- [10] H. Gleiter, "Nanocrystalline materials," *Progress in Materials Science*, vol. 33, no. 4, pp. 223–315, 1989.
- [11] U. Erb, "Size effects in electroformed nanomaterials," *Key Engineering Materials*, vol. 444, pp. 163–188, 2010.
- [12] B. Szpunar, U. Erb, K. T. Aust, G. Palumbo, and L. J. Lewis, "The influence of grain-boundary structural disorder on the magnetic properties of nanocrystalline nickel," in *Material Research Society Symposium Proceeding*, vol. 318, pp. 477–482, 1994.
- [13] Y. Zhang and D. G. Ivey, "Characterization of Co-Fe and Co-Fe-Ni soft magnetic films electrodeposited from citrate-stabilized sulfate baths," *Materials Science and Engineering B*, vol. 140, no. 1–2, pp. 15–22, 2007.
- [14] I. Tabakovic, V. Inturi, and S. Riemer, "Composition, structure, stress, and coercivity of electrodeposited soft magnetic CoNiFe films: thickness and substrate dependence," *Journal of the Electrochemical Society*, vol. 149, no. 1, pp. C18–C22, 2002.
- [15] G. Herzer, "Grain size dependence of coercivity and permeability in nanocrystalline ferromagnets," *IEEE Transactions on Magnetics*, vol. 26, no. 5, pp. 1397–1402, 1990.
- [16] G. Fortas, S. Sam, Z. Fekih, and N. Gabouze, "Electrodeposition of CoNiFe alloys on n-type silicon," *Materials Science Forum*, vol. 609, pp. 207–212, 2009.
- [17] J. George, J. Rantschler, S. E. Bae, D. Litvinov, and S. R. Brankovic, "Sulfur and saccharin incorporation into electrodeposited CoFe alloys: consequences for magnetic and corrosion properties," *Journal of the Electrochemical Society*, vol. 155, no. 9, pp. D589–D594, 2008.
- [18] Information on <http://www.ndt-ed.org>.
- [19] L. P. Zhu, H. M. Xiao, W. D. Zhang, Y. Yang, and S. Y. Fu, "Synthesis and characterization of novel three-dimensional metallic Co dendritic superstructures by a simple hydrothermal reduction route," *Crystal Growth and Design*, vol. 8, no. 4, pp. 1113–1118, 2008.
- [20] I. A. Ovid'ko, C. S. Pande, and R. A. Masumura, "Grain boundaries in nanomaterials," in *Nanomaterials Handbook*, Y. Gogotsi, Ed., CRC Press, 2006.
- [21] Y. Marita and I. I. Yaacob, "Synthesis and characterization of nickel-iron-silicon nitride nanocomposite," *Advanced Materials Research*, vol. 97–101, pp. 1360–1363, 2010.
- [22] C. K. S. Cheung, *Synthesis and microstructural characterization of electrodeposited nanocrystalline soft magnets [Ph.D. thesis]*, Queen's University, Kingston, Ontario, Canada, 2001.
- [23] T. Yokoshima, K. Imai, T. Hiraiwa, and T. Osaka, "Preparation of high-Bs Co-Fe soft magnetic thin films by electrodeposition," *IEEE Transactions on Magnetics*, vol. 40, no. 4, pp. 2332–2334, 2004.
- [24] H. F. Li and R. V. Ramanujan, "Synthesis of Fe-Co based nanomagnetic materials," *Transactions of the Indian Institute of Metals*, vol. 58, no. 6, pp. 965–970, 2005.
- [25] T. Osaka, T. Sawaguchi, F. Mizutani, T. Yokoshima, M. Takai, and Y. Okinaka, "Effects of saccharin and thiourea on sulfur inclusion and coercivity of electroplated soft magnetic CoNiFe film," *Journal of the Electrochemical Society*, vol. 146, no. 9, pp. 3295–3299, 1999.
- [26] T. Osaka, "Electrodeposition of highly functional thin films for magnetic recording devices of the next century," *Electrochimica Acta*, vol. 45, no. 20, pp. 3311–3321, 2000.

Research Article

The Effect of Reducing Time on the Magnetoresistance of Manganite $\text{La}_{0.67}\text{Sr}_{0.20}\text{Cu}_{0.10}\square_{0.03}\text{MnO}_3$ at a Temperature of 30°C

Hongwei Zhao,¹ Lichun Hu,² and Zhanxin Zhang¹

¹College of Science, Hebei United University, Tangshan 063009, China

²Department of Basic Teaching, Tangshan College, Tangshan 063000, China

Correspondence should be addressed to Hongwei Zhao, zhaowei2001@yahoo.com.cn

Received 18 July 2012; Revised 8 October 2012; Accepted 18 October 2012

Academic Editor: Gang Xiang

Copyright © 2012 Hongwei Zhao et al. This is an open access article distributed under the Creative Commons Attribution License, which permits unrestricted use, distribution, and reproduction in any medium, provided the original work is properly cited.

$\text{La}_{0.67}\text{Sr}_{0.20}\text{Cu}_{0.10}\square_{0.03}\text{MnO}_3$ (“ \square ” representing cation vacancy) polycrystalline manganite powder was synthesized by sol-gel method, which we used as parent materials. After reduced in hydrogen atmosphere for 30 and 60 minutes at a temperature of 400°C , the series bulk samples were obtained by sintering in argon atmosphere for 12 hours at 1100°C . The structure, electrical and magnetic properties, and colossal magnetoresistance of samples were researched in detail. Experiment results indicate that under an applied magnetic field of 1.8 T, the two bulk samples sintered in Ar atmosphere for 12 hours at 1100°C , with the powder reduced for 30 and 60 minutes in 400°C hydrogen atmosphere for $\text{La}_{0.67}\text{Sr}_{0.20}\text{Cu}_{0.10}\square_{0.03}\text{MnO}_3$ parent powders, respectively, have the stable MR ($11.0 \pm 0.3\%$) and ($10.0 \pm 0.5\%$) in temperature region from 270 K to 330 K. This is important for the potential application of this kind of magnetoresistance materials.

1. Introduction

Manganite $\text{R}_{1-x}\text{T}_x\text{MnO}_3$ with ABO_3 perovskite structure, where R and T are rare earth and alkaline earth ions, respectively, has been extensively studied due to its abundant physics related to colossal magnetoresistance (CMR) and its potential application in magnetic devices [1–4]. In general, the MR magnitude of a perovskite manganite reaches the maximum only at the Curie temperature (T_C), which is beyond the room temperature region generally. And the MR changes abruptly with the temperature approaching the Curie temperature. These properties severely limit the practical applications of these materials [5–8]. Many researchers have thus been concentrated on making new material system that provides low-field magnetoresistance (LFMR) around room temperature. On the other hand, recent efforts to broaden the CMR temperature range have been made by means of the Mn-site substitution or oxygen deficiency [9–12]. Brando et al. [11] studied the dependence of oxygen deficiency on electrical and magnetic properties of $\text{La}_{0.85}\text{Na}_{0.15}\text{MnO}_{3-\delta}$ ($\delta = 0; 0.04; 0.10$), they found that when the δ increased, the Curie temperature of the samples decreased. Liu et al. [12] studied the electrical

properties and magnetoresistance effect and found that for $\text{La}_{0.67}\text{Sr}_{0.33}\text{MnO}_3$, Sr-site substituted by Cu and leading to vacancy could both change the peak temperature (TMR) of MR to room temperature and improve the peak value of MR.

In this paper, we chose $\text{La}_{0.67}\text{Sr}_{0.20}\text{Cu}_{0.10}\square_{0.03}\text{MnO}_3$ as parent materials because its TMR is higher than room temperature, and its MR value is a little bigger. By means of reducing the powders in different temperature hydrogen atmosphere and changing the oxygen content of the parent materials, both the stabilization of MR and the peak value of MR are improved.

2. Experiment

$\text{La}_{0.67}\text{Sr}_{0.20}\text{Cu}_{0.10}\square_{0.03}\text{MnO}_3$ polycrystalline manganite powder was prepared by sol-gel method [12], which we used as parent powder materials. After reduced in hydrogen atmosphere for 30 and 60 minutes at a temperature of 400°C , the series bulk samples were obtained by sintering in argon atmosphere for 12 hours at 1100°C .

The phase identification of samples at room temperature has been carried out by the X-ray diffraction (XRD) with an

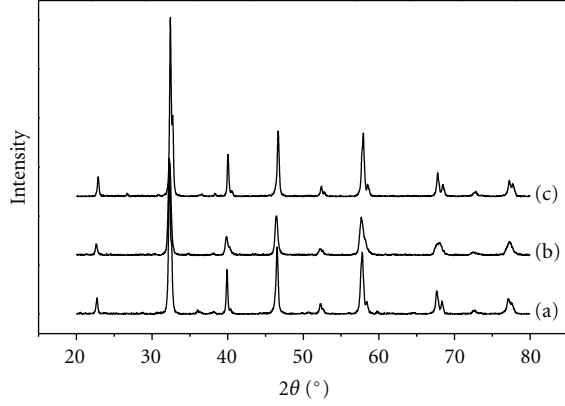


FIGURE 1: X-ray diffraction patterns for bulk samples B1 (a), B2 (b), and B3 (c).

TABLE 1: The lattice parameters and unit cell volume for bulk samples B1, B2, and B3.

Sample ID	Lattice parameters		Crystal cell volume $V/\text{Å}^3$
	$a/\text{Å}$	$c/\text{Å}$	
B1	5.5273	13.371	353.77
B2	5.5158	13.356	351.92
B3	5.5160	13.366	352.19

18 kW Rigaku Max-RB diffractometer with $\text{CuK}\alpha$ radiation in the 2θ range of 20° – 80° . The magnetization measurements were carried out with a Lake Shore vibrating sample magnetometer (VSM) in the temperature region of 120–370 K. All the Curie's temperature measurements were performed at an applied field 0.05 T. The morphology was obtained by S-570 scanning electron microscopy (SEM). The temperature and magnetic field dependences of the resistivity were measured (using Oxford Maglab Exa Measurement System) with the standard DC four-probe method, and the applied field was parallel to the direction of current.

3. Results and Discussion

3.1. X-Ray Characterization. The structural characterization of the powder samples grinding from the bulk samples was determined. Figure 1 shows the X-ray diffraction patterns for bulk samples B1–B3. (B1: parent materials; B2: reduced for 30 min; B3: reduced for 60 min). The results indicate that the materials are a single phase with $R\bar{3}c$ perovskite phase without any other secondary or impurity phase.

We use a Rietveld refinement software Fullprof Suite to calculate the lattice parameter and crystal cell volume. The results are given in Table 1. It can be seen from Table 1 that the lattice parameter and crystal cell volume of reduced samples B2 and B3 are slightly lower comparing to parent sample B1, thus causing the Mn–O bond length of the unit cell to be slightly lower.

3.2. Morphology of the Powder Sample. Figure 2 shows the scanning electron microscopy (SEM) morphology of powder

TABLE 2: The Curie temperature T_C (K) and special saturation magnetization σ (Am^2/kg) for samples B1 (a), B2 (b), and B3 (c).

Sample ID	T_C (K)	σ (Am^2/kg)
B1	337.6	9.5
B2	307.3	4.3
B3	305.2	3.2

samples B1, B2, and B3. From Figure 2, we can see that the $\text{La}_{0.67}\text{Sr}_{0.20}\text{Cu}_{0.10}\square_{0.03}\text{MnO}_3$ parent sample B1 prepared by sol-gel method possesses homogeneously globular shape grains, and the grain size is about 100 nm. After being reduced by hydrogen, the phenomenon of conglomeration in particles was improved.

3.3. Magnetization versus Temperature of Power Samples. Figure 3(a) shows curves of the special magnetization σ versus temperature T for the power samples, under an applied magnetic field of 0.05 T. Figure 3(a) shows that in the temperature region measured, the samples experienced a shift from ferromagnetic to paramagnetic; the changes have gone through a transition region, because samples still in the transition zone show varying degrees of ferromagnetism, so we define $d\sigma/dT$ which tends to zero corresponding to the temperature as the Curie temperature T_C .

Figure 3(b) shows curves of the $d\sigma/dT$ calculated from Figure 3(a) versus temperature, in which the Curie temperature (T_C) of the samples is determined by $d\sigma/dT$ tending to zero. Figure 3(b) indicates that reducing treatment can decrease Curie temperature T_C of the sample obviously, and the more reducing time, the more Curie temperature T_C decreases. Abdelmoula et al. [13] studied the dependence of oxygen deficiency on electrical and magnetic properties of $\text{La}_{0.7}\text{Sr}_{0.3}\text{MnO}_{3-\delta}$ ($0 \leq \delta \leq 0.15$), they found that when the δ increased, the Curie temperature of the samples decreased, which was the same as our conclusion. This phenomenon can be explained by the weakness of double exchange theory. Reducing treatment could result in the deficiency of oxygen. With oxygen deficiency increased, Mn^{4+} ion is reduced, Mn^{3+} ion increased, and R_n (the ratio of Mn^{4+} and Mn^{3+} ion) decreased quickly, causing T_C to lower temperature.

Figure 4 shows the magnetic hysteresis loop of the powder samples at room temperature (300 K).

As shown in Figure 4, at room temperature (300 K), our samples are in the transition region from ferromagnetic to paramagnetic; the Curie temperature is higher than room temperature; magnetization has not yet reached saturation under an applied magnetic field of 500 mT.

Table 2 shows the special saturation magnetization σ (Am^2/kg) under an applied magnetic field 500 mT. It can be seen from Table 2 that: Reducing treatment could reduce the special magnetization σ significantly, as the reducing time longer, σ decreases more.

3.4. Colossal Magnetoresistance of Samples. The temperature dependence of the resistivity measured in zero field and in an applied field (1.8 T) for the samples B1 (a), B2 (b), and

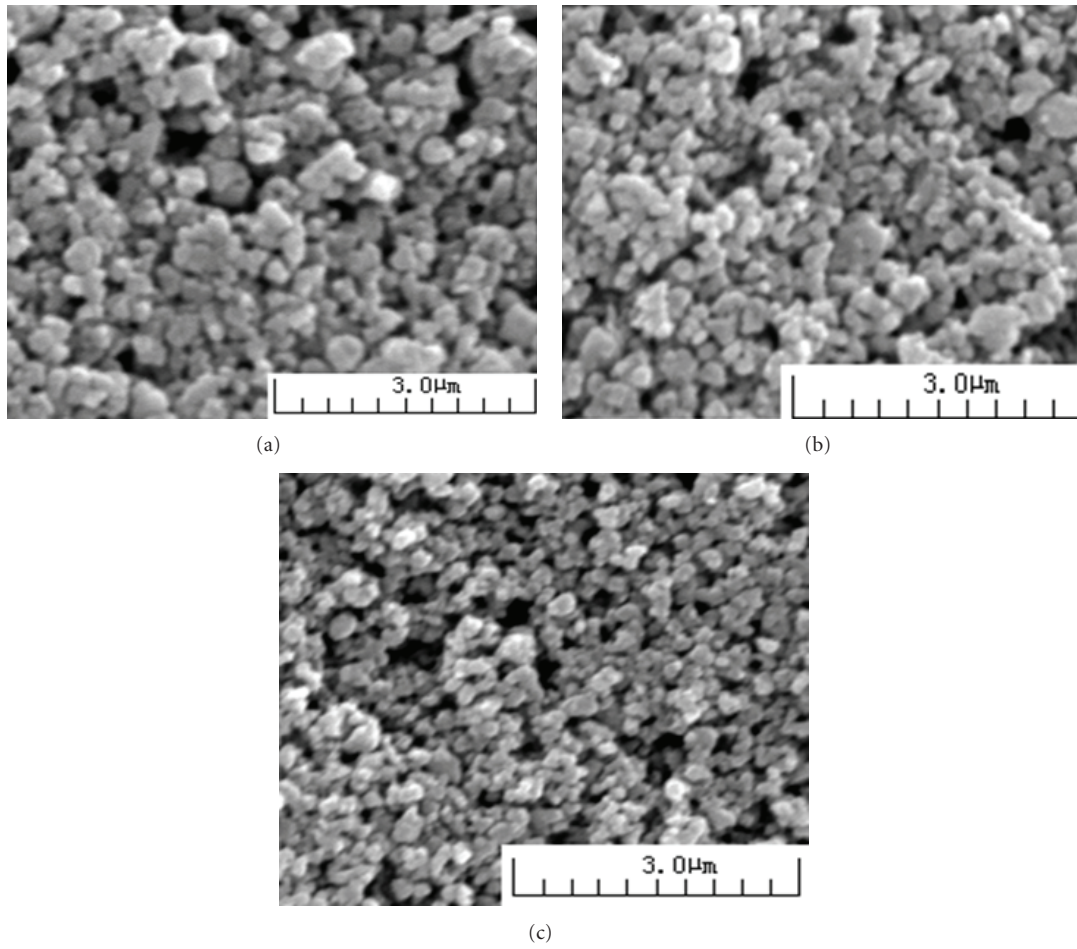


FIGURE 2: SEM morphology of powder samples B1, B2, and B3.

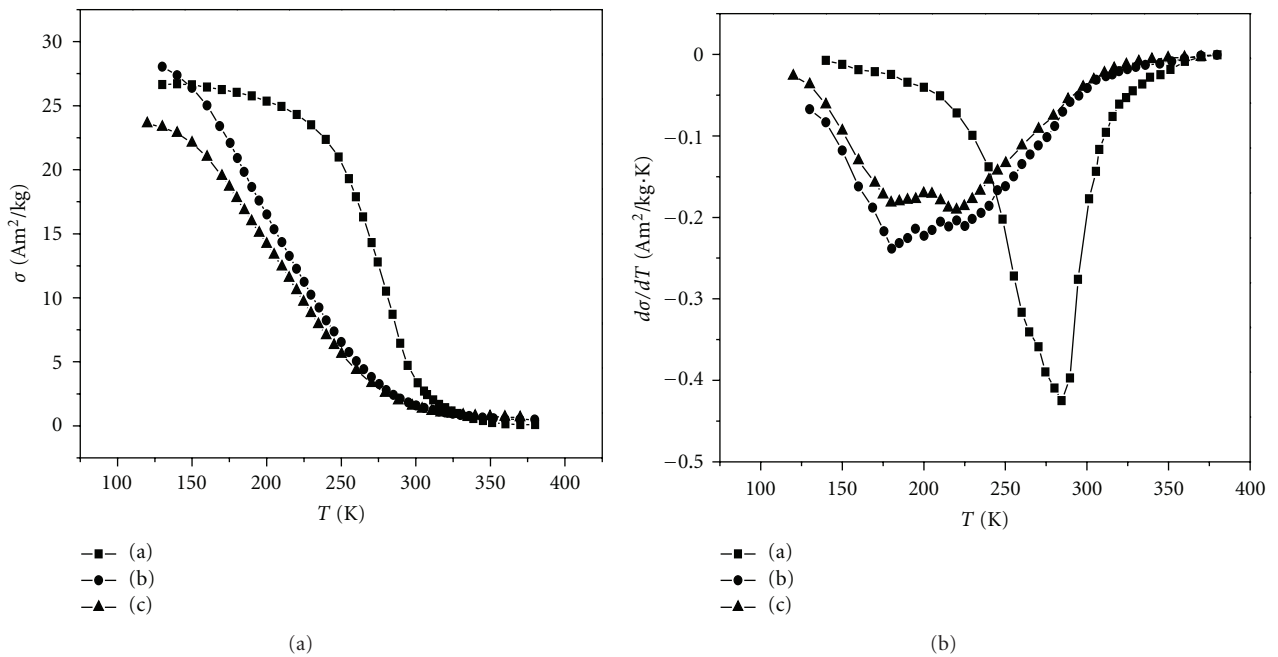


FIGURE 3: (a) Curves of special magnetization σ versus temperature T for samples B1 (a), B2 (b), and B3 (c). (b) Curves of $d\sigma/dT$ calculated from Figure 3(a) versus temperature T for samples B1 (a), B2 (b), and B3 (c).

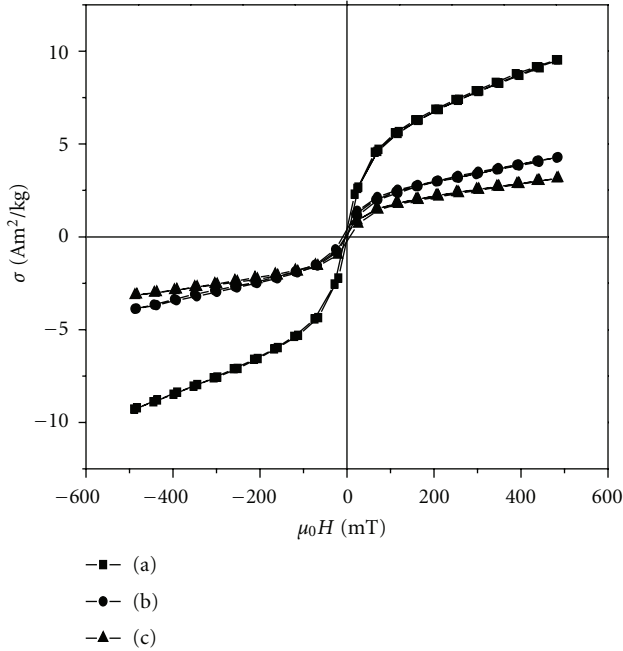


FIGURE 4: The magnetic hysteresis loop for samples B1 (a), B2 (b), and B3 (c) at room temperature (300 K).

B3 (c) is plotted in Figure 5. From Figure 5, we know that with the increase of temperature, the conductivity of the samples experienced a metal-semiconductor transition. The definition of metal-semiconductor transition temperature TMI for resistivity and temperature curve of resistivity maximum point corresponds to the temperature. For sample B1 (a), as in the temperature deviation TMI, its resistivity decreases rapidly, similarly to most of what is reported in the reference. But for samples B2 (b) and B3 (c), their resistivity changes a little near TMI.

Define the magnetoresistance by $MR(\%) = [(\rho_0 - \rho_H)/\rho_0] \times 100\%$, where ρ_0 and ρ_H stand for the resistivities at 0 and 1.8 T, different from most of the reports in the past; as the temperature decreases, the changes in samples B2 and B3 can be divided into three stages: in the high temperature area, MR increases as the temperature decreases; in near room temperature, MR is basically unchanged; in the low-temperature area, with decreasing temperature MR continues to increase.

For B2 and B3 samples at room temperature (300 K), their MR was 11.0% and 10.0%, not only higher than the sample B1 (9.5%), but also the temperature stability of MR is better; in the temperature range from 270 K to 330 K, their MR was maintained at 11.0% ($\pm 0.3\%$) and 10.0% ($\pm 0.5\%$) almost flat with temperature, which is important for the potential application of this kind of magnetoresistance materials.

4. Conclusions

By using reducing treatment, we can improve the MR of $\text{La}_{0.67}\text{Sr}_{0.20}\text{Cu}_{0.10}\square_{0.03}\text{MnO}_3$ polycrystalline manganite. The reduced samples B2 and B3 have the stable MR ($11.0 \pm 0.3\%$)

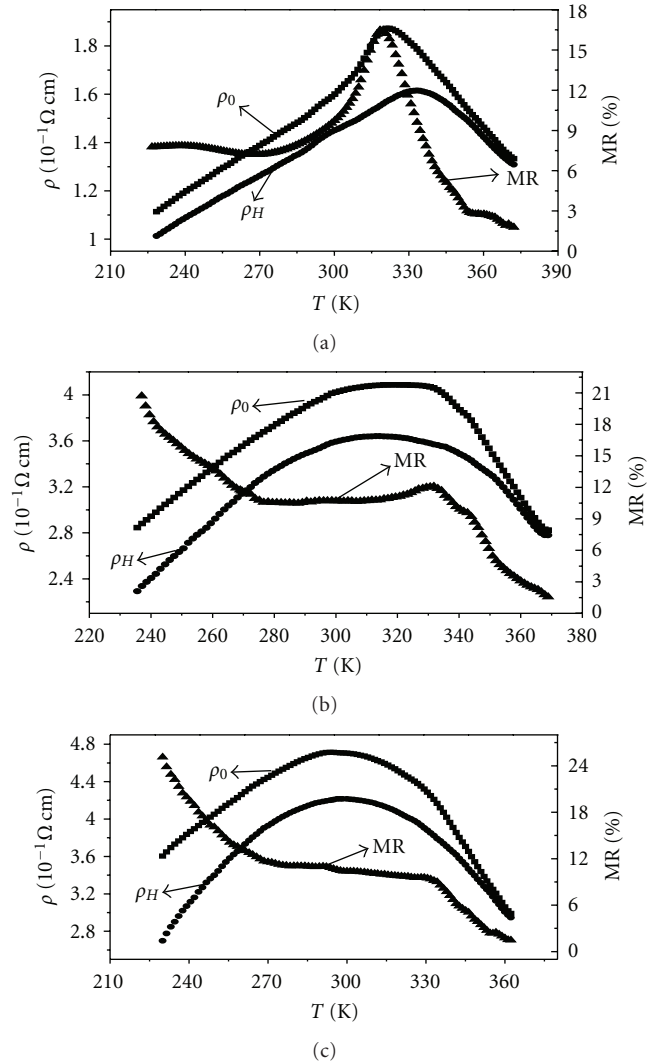


FIGURE 5: Temperature dependence of the resistivity measured in zero field and in an applied field (1.8 T) for samples B1 (a), B2 (b), and B3 (c). The corresponding magnetoresistances are also indicated.

and ($10.0 \pm 0.5\%$) in a temperature range between 270 K and 330 K. this is important for the potential application of this kind of magnetoresistance materials.

Acknowledgment

This work was supported by Science and Technology Research Program for Colleges and Universities in Hebei Province, China (Grant no. Z2012002) and supported by foundation science of Hebei united university (Grant no. Z201216).

References

- [1] Y. Tokura and Y. Tomioka, "Colossal magnetoresistive manganites," *Journal of Magnetism and Magnetic Materials*, vol. 200, no. 1, pp. 1–23, 1999.

- [2] J. Yang, Y. Q. Ma, B. C. Zhao et al., "Structural, magnetic and transport properties in the manganites $\text{La}_{0.7}\text{Sr}_{0.3-x}\text{Te}_x\text{MnO}_3$ ($0 \leq x \leq 0.15$)," *Solid State Communications*, vol. 134, no. 7, pp. 443–447, 2005.
- [3] C. H. Yan, Z. G. Xu, T. Zhu et al., "A large low field colossal magnetoresistance in the $\text{La}_{0.7}\text{Sr}_{0.7}\text{MnO}_3$ and CoFe_2O_4 combined system," *Journal of Applied Physics*, vol. 87, no. 9, pp. 5588–5590, 2000.
- [4] P. Chen, D. Y. Xing, Y. W. Du, J. M. Zhu, and D. Feng, "Giant room-temperature magnetoresistance in polycrystalline $\text{Zn}_{0.41}\text{Fe}_{2.59}\text{O}_4$ with $\alpha\text{-Fe}_2\text{O}_3$ grain boundaries," *Physical Review Letters*, vol. 87, no. 10, Article ID 107202, 3 pages, 2001.
- [5] A. J. Millis, P. B. Littlewood, and B. I. Shraiman, "Double exchange alone does not explain the resistivity of $\text{La}_{1-x}\text{Sr}_x\text{MnO}_3$," *Physical Review Letters*, vol. 74, no. 25, pp. 5144–5147, 1995.
- [6] A. J. Millis, B. I. Shraiman, and R. Mueller, "Dynamic Jahn-Teller effect and colossal magnetoresistance in $\text{La}_{1-x}\text{Sr}_x\text{MnO}_3$," *Physical Review Letters*, vol. 77, no. 1, pp. 175–178, 1996.
- [7] A. J. Millis, "Cooperative Jahn-Teller effect and electron-phonon coupling in $\text{La}_{1-x}\text{A}_x\text{MnO}_3$," *Physical Review B*, vol. 53, no. 13, pp. 8434–8441, 1996.
- [8] W. Feng and L. Ming, "Low-field magnetoresistance of perovskite manganite," *Progress in Physics*, vol. 23, no. 3, pp. 192–210, 2003.
- [9] J.-M. Liu, Q. Huang, J. Li et al., "Effect of oxygen nonstoichiometry on electrotransport and low-field magnetotransport property of polycrystalline $\text{La}_{0.5}\text{Sr}_{0.5}\text{MnO}_{3-\delta}$ thin films," *Physical Review B*, vol. 62, no. 13, pp. 8976–8982, 2000.
- [10] J. Li, J.-M. Liu, H. P. Li, H. C. Fang, and C. K. Ong, "Magnetoresistance in oxygen deficient $\text{La}_{0.75}\text{Sr}_{0.25}\text{MnO}_{3-\delta}$ thin films prepared by pulsed laser deposition," *Journal of Magnetism and Magnetic Materials*, vol. 202, no. 2, pp. 285–291, 1999.
- [11] M. Brando, R. Caciuffo, J. Hemberger, A. Loidl, L. Malavasi, and P. Ghigna, "Magnetic and electronic properties of $\text{La}_{0.85}\text{Na}_{0.15}\text{MnO}_{3-\delta}$," *Journal of Magnetism and Magnetic Materials*, vol. 272–276, no. 1, pp. 417–419, 2004.
- [12] X. M. Liu, G. D. Tang, X. Zhao et al., "Influences of Cu-doped and Sr vacancy on the room magnetoresistance of $\text{La}_{0.67}\text{Sr}_{0.33-x-y}\text{Cu}_x\text{MnO}_3$," *Journal of Magnetism and Magnetic Materials*, vol. 277, no. 1-2, pp. 118–122, 2004.
- [13] N. Abdelmoula, K. Guidara, A. Cheikh-Rouhou, E. Dhahri, and J. C. Joubert, "Effects of the oxygen nonstoichiometry on the physical properties of $\text{La}_{0.7}\text{Sr}_{0.7}\text{MnO}_{3-\delta}$ manganites ($0 \leq \delta \leq 0.15$)," *Journal of Solid State Chemistry*, vol. 151, no. 1, pp. 139–144, 2000.

Research Article

Spin Waves Excitations of Co/Pt Multilayers

W. Zhou

Key Laboratory of Materials Physics, Institute of Solid State Physics, Chinese Academy of Sciences, Hefei 230031, China

Correspondence should be addressed to W. Zhou, weizhou@theory.issp.ac.cn

Received 25 July 2012; Accepted 25 September 2012

Academic Editor: Weichang Hao

Copyright © 2012 W. Zhou. This is an open access article distributed under the Creative Commons Attribution License, which permits unrestricted use, distribution, and reproduction in any medium, provided the original work is properly cited.

The present work investigated interlayer couplings of $[\text{Co}(20 \text{ \AA})/\text{Pt}(30 \text{ \AA})]_5$, $[\text{Co}(4 \text{ \AA})/\text{Pt}(7 \text{ \AA})]_{30}$, and $[\text{Co}(4 \text{ \AA})/\text{Pt}(9 \text{ \AA})]_{30}$ multilayers with strong perpendicular magnetic anisotropy (PMA). Brillouin light scattering measurements were utilized to obtain spin waves of these samples with in-plane external magnetic fields. Interlayer couplings were found to be very sensitive to Pt thickness change from 7 Å to 9 Å, which implies that Pt atoms were more difficult to be polarized to provide interlayer coupling between Co layers than in the perpendicular external magnetic field situation. When Pt layer is 30 Å, the observed single spin wave can confirm the disappearance of interlayer coupling even when Co layer thickness is 20 Å.

1. Introduction

Since the first observation of spin waves in 1946 by Griffiths [1], with wide applications of laser in light scattering experiments and the invention of multipass Feby Péro interferometer by Sandercock in 1970 [2], Brillouin scattering became an important tool in the field of magnetism to detect different kinds of magnetic excitations in various systems, including bulk materials, thin films, and nanostructures. Magnetic thin film systems are of particular importance due to their rich magnetism physics and practical applications in magnetic recording industry; it includes systems of single magnetic films, double magnetic films, and multiple layered magnetic films composed by ferromagnetic (FM), antiferromagnetic (AFM), and nonmagnetic (NM) films of different thickness and layer arrangements, among which FM/NM multilayers gained a long-term interest in the last decade. Many theoretical and experimental works were devoted to this field in understanding its magnetic behaviors especially for the perpendicular magnetic anisotropy thin films [3–7] through different approaches like neutron scattering, ferromagnetic resonance, magneto-optical Kerr microscopy, and Brillouin scattering. Generally, external magnetic fields were applied perpendicular to the sample surface in PMA samples in various experimental methods mentioned above. However, in this work, we are going to apply magnetic fields inplane to three strong PMA samples $[\text{Co}(20 \text{ \AA})/\text{Pt}(30 \text{ \AA})]_5$,

$[\text{Co}(4 \text{ \AA})/\text{Pt}(7 \text{ \AA})]_{30}$, and $[\text{Co}(4 \text{ \AA})/\text{Pt}(9 \text{ \AA})]_{30}$ then use Brillouin scattering to detect spin waves, from which magnetic coupling behaviors can be deduced and compared with experiments with magnetic fields perpendicular to the sample surface. Due to the weak in-plane magnetic anisotropy, three strong PMA samples will have different spin waves when Co and Pt thickness changed thus providing another approach to understand magnetic coupling of this system.

2. Experimental Procedure

Ferromagnetic multilayers $[\text{Co}(t_1)/\text{Pt}(t_2)]_N$ with t_1 and t_2 as thickness of corresponding Co and Pt layers with N total periods were fabricated using a magnetron sputtering system of ultrahigh vacuum with working pressure of at least 10^{-9} torr. Three samples used in the present work are $[\text{Co}(20 \text{ \AA})/\text{Pt}(30 \text{ \AA})]_5$, $[\text{Co}(4 \text{ \AA})/\text{Pt}(7 \text{ \AA})]_{30}$, and $[\text{Co}(4 \text{ \AA})/\text{Pt}(9 \text{ \AA})]_{30}$. All of them were fabricated on the Si substrate with native oxide and 100 Å buffer layer of Pt, after Co and Pt layers of designed thickness were deposited; 30 Å Pt was deposited as the capping layer. All samples were found to have perpendicular magnetic anisotropy using a Lake Shore vibrating sample magnetometer (VSM) in [8], where more details of sample fabrication and calibration can be found.

Brillouin light scattering experiments were carried out using a tandem six-pass Feby Péro interferometer.

A single p-polarized 514.5 nm laser was used as the excitation source with an output power of 50 mW, focusing on a spot of approximately $50\ \mu\text{m}$ in diameter. A water cooling electromagnet was used to provide magnetic fields up to 10 KOe in the direction parallel to the sample surface. The standard backscattering geometry was utilized in the whole experimental process, where the incident laser has different angles of 30° , 45° , and 60° with respect to the normal direction of sample surface. Scattered light from spin waves was analyzed by the software Ghost to get Stoke and Antistoke spin waves at different external magnetic fields.

3. Results and Discussion

Figure 1 shows Brillouin spectra of spin waves of sample $[\text{Co}(20\ \text{\AA})/\text{Pt}(30\ \text{\AA})]_5$ with laser incident angle of 60° , where the external magnetic field is parallel to the sample surface up to 8.0 KOe; the experiment geometry is shown in the inset of Figure 2. Spin wave frequencies increase with external magnetic fields almost linearly from approximately 10 GHz at 1.0 KOe to 30 GHz at 8.0 KOe. In Figure 2, it shows a linear fit of 10 measured data points up to 10.4 KOe; the linear fitting function $y = 6.86 + 3.02 * x$ has very small stand errors of intercept and slope as 0.536 and 0.086; the adjusted coefficient of determination (adj. R -square) is also a small number as 0.993. Thus, we believe that the observed spin wave energies increase linearly with the external magnetic fields H rather than in the form of square root of H , which is a typical behavior of spin waves whose wave vector q is parallel rather than perpendicular to the magnetization M . Besides spin waves, there are two weak peaks around 4 GHz and 9 GHz at high magnetic fields of 7.0 KOe and 8.0 KOe, which show no changes with magnetic fields; they were confirmed as phonons from Brillouin scattering measurements without magnetic fields. Similar phonons were also observed for the other two samples $[\text{Co}(4\ \text{\AA})/\text{Pt}(7\ \text{\AA})]_{30}$ in Figure 4 and $[\text{Co}(4\ \text{\AA})/\text{Pt}(9\ \text{\AA})]_{30}$ in Figure 5.

The incident angle dependence of spin waves frequency was checked by changing laser incident angle θ to the normal of sample surface from 60° to 30° and 45° at different external magnetic fields. When the magnetic field was switched to the inverse direction, it was denoted as a negative field relative to the previous field in Figure 3. There are two observations from spectra in Figure 3. The first is that the spin waves at different incident angles θ have the same frequencies as those of 60° plotted in Figures 1 and 2 within experimental error, which demonstrates independence of spin wave frequency with respect to the incident angle θ . To confirm such a conclusion, we extended free spectra range to 100 GHz and found no other spin waves. Thus, the single observed spin wave of sample $[\text{Co}(20\ \text{\AA})/\text{Pt}(30\ \text{\AA})]_5$ shows no surface spin wave behavior, whose frequency is incident angle dependent in the form of cosine. The second observation is that the left side of spectra (Stoke side) is weaker than the right side (Antistoke side) for negative magnetic fields; the situation was totally inverted when magnetic fields are positive. The same phenomena can also be observed in $\theta = 60^\circ$ in Figure 1, where the magnetic fields are positive

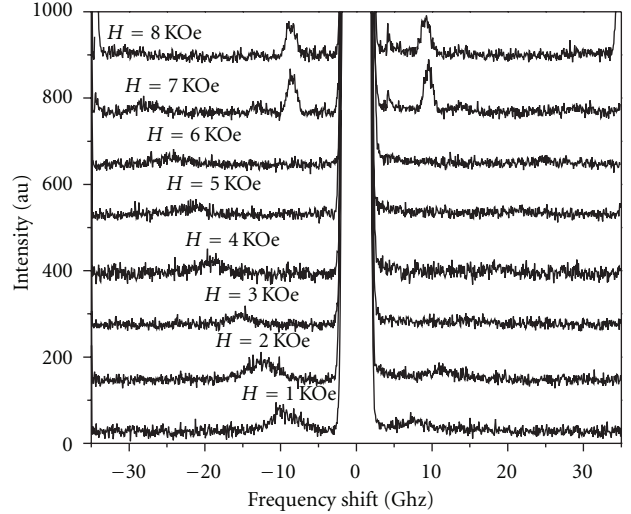


FIGURE 1: Spin wave Brillouin spectra of sputtered $[\text{Co}(20\ \text{\AA})/\text{Pt}(30\ \text{\AA})]_5$ sample with incident angle θ of 60° and magnetic fields parallel to the sample surface up to 8.0 KOe.

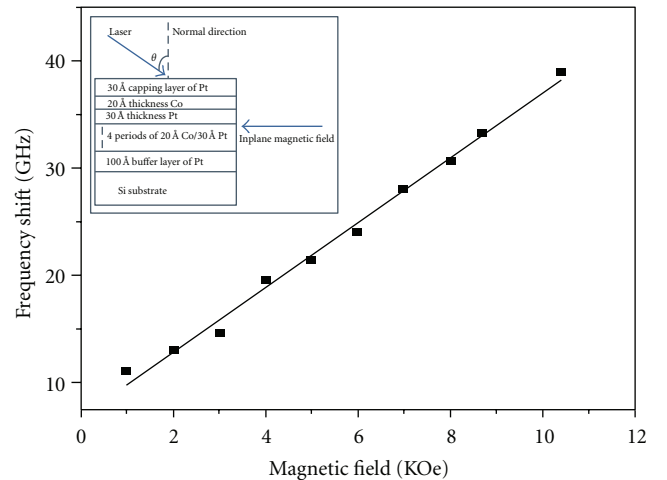


FIGURE 2: Magnetic field dependence of the spin wave frequencies of $[\text{Co}(20\ \text{\AA})/\text{Pt}(30\ \text{\AA})]_5$ sample with incident angle θ as 60° . The solid line is the linear fit of 10 measured data points. The inset shows the experiment geometry.

with Stoke side always stronger than Antistoke side. This is totally different from the normal acoustic excitations; their Stoke and Antistoke sides are of roughly the same intensity except for a temperature-dependent factor, which is a very small difference at room temperature compared with magnetic excitations intensity differences we observed. The explanation is due to the lack of time reversal symmetry for Stoke and Antistoke processes; spin wave intensity is proportional to the square of $GM \pm K$ as calculated in [9], where M is the magnetization component and K and G are imaginary and real tensor part of dielectric constant fluctuations. \pm are for Stoke and Antistoke intensities, which are the origin of the observed spin wave intensity asymmetry.

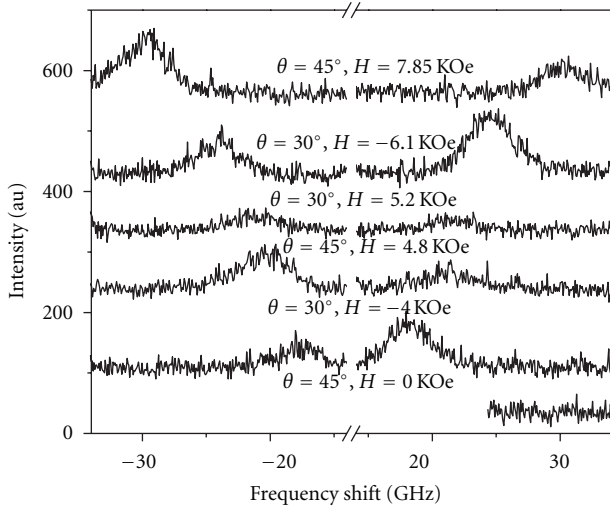


FIGURE 3: Spin wave Brillouin spectra of sputtered $[\text{Co}(20 \text{ \AA})/\text{Pt}(30 \text{ \AA})]_5$ sample with incident angle θ as 30° and 45° at different magnetic fields parallel to the sample surface. Negative and positive fields have opposite directions.

Brillouin spectra of the other two samples $[\text{Co}(4 \text{ \AA})/\text{Pt}(7 \text{ \AA})]_{30}$ and $[\text{Co}(4 \text{ \AA})/\text{Pt}(9 \text{ \AA})]_{30}$ were presented in Figures 4 and 5. They both have 120 \AA Pt layers, comparable with the 100 \AA Co layer of $[\text{Co}(20 \text{ \AA})/\text{Pt}(30 \text{ \AA})]_5$ sample. All three samples have strong perpendicular magnetic anisotropy with inplane magnetization much weaker from VSM measurements in [8]. In Figure 4, two acoustic phonons at low frequencies can be observed; the one with larger intensity is at 7.2 GHz and the weaker one at 11.2 GHz ; they have similar positions as phonons of sample $[\text{Co}(4 \text{ \AA})/\text{Pt}(9 \text{ \AA})]_{30}$, which are 6.6 GHz for the stronger phonon and 10.2 GHz for the weaker phonon separately. There are clearly two spin waves at 23.1 GHz and 15.2 GHz of sample $[\text{Co}(4 \text{ \AA})/\text{Pt}(7 \text{ \AA})]_{30}$ at magnetic fields of $\pm 6.5 \text{ KOe}$, whose Stoke and Antistoke relative intensities are different in the same manner as the spectra of $[\text{Co}(20 \text{ \AA})/\text{Pt}(30 \text{ \AA})]_5$ sample in Figures 1 and 3.

By comparing the spectra of $\pm 6.5 \text{ KOe}$ of $[\text{Co}(4 \text{ \AA})/\text{Pt}(7 \text{ \AA})]_{30}$ sample in Figure 4 and that of 8.7 KOe of $[\text{Co}(4 \text{ \AA})/\text{Pt}(9 \text{ \AA})]_{30}$ sample in Figure 5, one can find that spin waves of the former are stronger than those of the second sample. This can be attributed to their different Pt thickness, which is also their only difference. Because of the weak in-plane magnetic anisotropy, the external in-plane magnetic fields can only excite weak spin waves in thin 4 \AA Co layers compared with 20 \AA Co layers in the sample $[\text{Co}(20 \text{ \AA})/\text{Pt}(30 \text{ \AA})]_5$, where stronger spin waves can be obtained in Figure 3. We thus understand that signal-to-noise ratio of spin waves is determined by the thickness of Co layer thickness. Another interesting observation is that the spin waves species are different between sample $[\text{Co}(20 \text{ \AA})/\text{Pt}(30 \text{ \AA})]_5$ and two later layered samples of 30 layers. By changing free spectra range to more than 100 GHz , we found only one spin wave for the sample $[\text{Co}(20 \text{ \AA})/\text{Pt}(30 \text{ \AA})]_5$ and two spin waves for samples $[\text{Co}(4 \text{ \AA})/\text{Pt}(7 \text{ \AA})]_{30}$ and $[\text{Co}(4 \text{ \AA})/\text{Pt}(9 \text{ \AA})]_{30}$.

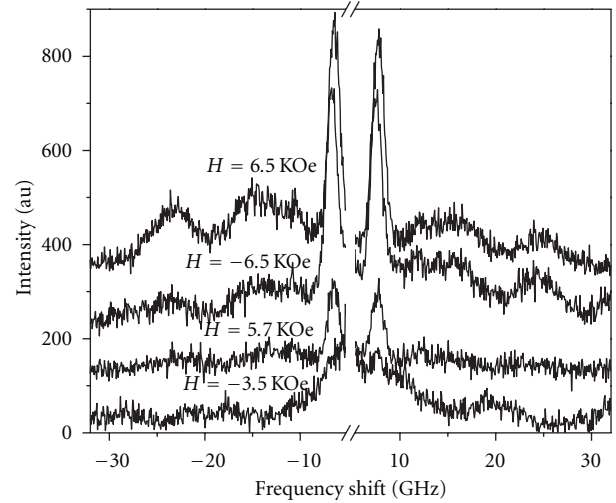


FIGURE 4: Spin wave Brillouin spectra of sputtered $[\text{Co}(4 \text{ \AA})/\text{Pt}(7 \text{ \AA})]_{30}$ sample with incident angle θ as 60° at different magnetic fields parallel to the sample surface. Negative and positive fields have opposite directions.

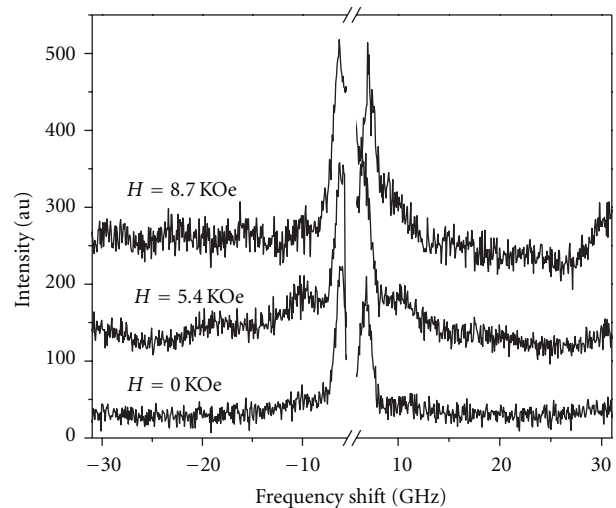


FIGURE 5: Spin wave Brillouin spectra of sputtered $[\text{Co}(4 \text{ \AA})/\text{Pt}(9 \text{ \AA})]_{30}$ sample with incident angle θ as 60° at different magnetic fields parallel to the sample surface.

Also, their spin wave frequency behaviors are different under external magnetic fields. Besides the linear increasing of spin wave frequency with magnetic fields of sample $[\text{Co}(20 \text{ \AA})/\text{Pt}(30 \text{ \AA})]_5$ in Figure 2, spin wave frequency of the other two samples shifts clearly in a different manner, although due to the limited signal-to-noise ratio, not all spin waves of the two samples $[\text{Co}(4 \text{ \AA})/\text{Pt}(7 \text{ \AA})]_{30}$ and $[\text{Co}(4 \text{ \AA})/\text{Pt}(9 \text{ \AA})]_{30}$ can be clearly resolved. This difference can be attributed to the different interlayer couplings of ferromagnetic Co layers. In [10, 11], magneto-optical Kerr microscopy was used to investigate interlayer couplings of same batch of $[\text{Co}(4 \text{ \AA})/\text{Pt}(t)]_N$ multilayers with strong perpendicular magnetic anisotropy. When the Pt thickness is less than 11 \AA , Co layers are strongly coupled.

Although in our study, magnetic fields are parallel to the sample surface, the induced magnetization should still be coupled, which can be used to explain the observed two spin waves and their intensity decreasing when Pt layers changed from 7 Å to 9 Å. So we conclude that the in-plane magnetization is much weaker to polarize Pt atoms to provide interlayer coupling of Co layers as in the perpendicular cases; thus, the spin waves are very weak and only observable at high magnetic fields, such as ± 6.5 KOe spectra in Figure 4. When Pt layers changed from 7 Å to 9 Å, magnetic field up to 8.7 KOe is still not enough to get clear spin wave signals as before. On the contrary, when Pt is of 30 Å thickness, Kerr imaging can confirm that the interlayer couplings are quite small, which can explain the observed one spin wave in [Co(20 Å)/Pt(30 Å)]₅ sample, with almost no couplings between Co layers. Also, 20 Å Co thickness layer can provide strong spin wave signals as in Figure 2.

4. Conclusions

In conclusion, interlayer coupling of three Co/Pt multilayers has been investigated by Brillouin scattering with in-plane magnetic fields. We find one spin wave of [Co(20 Å)/Pt(30 Å)]₅ sample; its frequency increases linearly with magnetic fields and independently of incident angles, which implies that Co interlayer coupling is negligibly small; two spin waves of [Co(4 Å)/Pt(7 Å)]₃₀ and [Co(4 Å)/Pt(9 Å)]₃₀ are also found, and their frequency behaviors are different from the first one, which demonstrates the existence of Co interlayer coupling and the decreasing of this coupling with increasing Pt thickness. Although we used in-plane magnetic fields to investigate perpendicular magnetic anisotropy samples, the behaviors of spin waves were found to be more sensitive to the Pt thickness change correspondingly, thus providing another approach to understand the multilayered magnetic thin film systems.

Acknowledgments

The author acknowledges Dr. F. Y. Yang, from The Ohio State University, for providing the multilayer samples, and Dr. R. Sooryakumar and X. P. Xie, from The Ohio State University, for helping in Brillouin scattering experiments and discussions. Support from the National Science Foundation of China (NSF no. 11204315) is gratefully acknowledged.

References

- [1] J. H. E. Griffiths, "Anomalous high-frequency resistance of ferromagnetic metals," *Nature*, vol. 158, pp. 670–671, 1946.
- [2] J. R. Sandercock, "Brillouin scattering study of SbSI using a double-passed, stabilised scanning interferometer," *Optics Communications*, vol. 2, pp. 73–76, 1970.
- [3] M. Buchmeier, H. Dassow, D. E. Bürgler, and C. M. Schneider, "Intensity of Brillouin light scattering from spin waves in magnetic multilayers with noncollinear spin configurations: theory and experiment," *Physical Review B*, vol. 75, Article ID 184436, 2007.
- [4] P. Manchanda, R. Skomski, P. K. Sahota, M. Franchin, H. Fangohr, and A. Kashyap, "Multiscale micromagnetism of Co-Pd multilayers," *Journal of Applied Physics*, vol. 111, Article ID 07C724, 2012.
- [5] P. J. Metaxas, J. P. Jamet, A. Mougin et al., "Creep and flow regimes of magnetic domain-wall motion in ultrathin Pt/Co/Pt films with perpendicular anisotropy," *Physical Review Letters*, vol. 99, no. 21, Article ID 217208, 2007.
- [6] H. Salhi, K. Chafai, O. Msieh et al., "Spin-wave excitations in evaporated Co/Pt multilayers," *Journal of Superconductivity and Novel Magnetism*, vol. 24, no. 5, pp. 1375–1379, 2011.
- [7] P. Landeros and D. L. Mills, "Spin waves in periodically perturbed films," *Physical Review B*, vol. 85, Article ID 054424, 2012.
- [8] J. W. Knepper and F. Y. Yang, "Oscillatory interlayer coupling in Co/Pt multilayers with perpendicular anisotropy," *Physical Review B*, vol. 71, Article ID 224403, 2005.
- [9] J. R. Sandercock, "Trends in Brillouin scattering: studies of opaque materials, supported films, and central modes," *Light Scattering in Solids III*, vol. 51, pp. 173–206, 1982.
- [10] M. Robinson, Y. Au, J. W. Knepper, F. Y. Yang, and R. Sooryakumar, "Magnetic imaging of layer-by-layer reversal in Co/Pt multilayers with perpendicular anisotropy," *Physical Review B*, vol. 73, Article ID 224422, 2006.
- [11] X. P. Xie, X. W. Zhao, J. W. Knepper, F. Y. Yang, and R. Sooryakumar, "Evolution of magnetic domain reversal with temperature in Co/Pt multilayers observed by magneto-optical Kerr imaging," *Physical Review B*, vol. 76, Article ID 184433, 2007.

Research Article

Magnetic Properties of Co-Fe-B Amorphous Films Thermomagnetically Treated with Different Field Directions

Zhe Liu, Weili Li, Weidong Fei, and Dan Xu

School of Materials Science and Engineering, Harbin Institute of Technology, Harbin 150001, China

Correspondence should be addressed to Weili Li, wlli@hit.edu.cn

Received 10 September 2012; Accepted 20 September 2012

Academic Editor: Weichang Hao

Copyright © 2012 Zhe Liu et al. This is an open access article distributed under the Creative Commons Attribution License, which permits unrestricted use, distribution, and reproduction in any medium, provided the original work is properly cited.

Co-Fe-B films were prepared by electroless plating. As-deposited films were thermomagnetically treated in the applied magnetic field of 500 Oe with different field directions at 300°C for 1 hour. The effects of magnetic field direction of thermomagnetic treatment on the structure and magnetic properties of Co-Fe-B thin films were investigated. It is found that two phases existed in annealed Co-Fe-B films: one is weak crystallized CoFe phase, the other being amorphous phase. The surface morphologies of the treated films are found to be affected by the direction of thermomagnetic treatment field. The results also show that the magnetic properties of thermomagnetically treated films are influenced greatly by the treatment field direction.

1. Introduction

Soft magnetic films have been widely used in magnetic heads, magnetic sensors, and planar inductors at high-frequency range. To play decisive roles in these devices, the magnetic materials must simultaneously possess higher saturation magnetization, lower coercivity, larger magnetic anisotropy, and higher resistivity. Amorphous Co-Fe-B thin films have been found to be good candidates for high-frequency applications, such as magnetic tunnel junction, HDD read-heads, and GHz magnetic film inductors [1–3]. Varieties of techniques have been used to prepare amorphous Co-Fe-B thin films, such as magnetron sputtering [4, 5], electroless deposition [6], and so forth. The electroless deposition method provides an alternative and promising fabrication process with advantages of low-cost, low-energy consumption and adaptation of complicated shapes.

Magnetic field annealing is an efficient way to induce different kinds of anisotropies in some crystalline magnetic materials [7–10], which closely correspond to magnetic performance. It has been reported that the magnetic field annealing can affect the microstructure, domain structure, and magnetic properties of amorphous materials [8, 11]. The previous researchers [12, 13] have indicated that the nanomagnetic phase or cluster can be formed during annealing treatment even when the annealing temperature is below

crystallization temperature. In this case, one can expect that the direction of magnetic field may affect the structure and properties of the amorphous films during thermomagnetic treatment. However, there are few reports on the influence of thermomagnetic treatment, especially under small magnetic field with different directions, on the magnetic properties of Co-Fe-B amorphous films.

In this paper, we prepared Co-Fe-B thin films which were annealed in small magnetic field (500 Oe) with respect to the film normal at different angles ($\alpha = 0 \sim 90^\circ$) subsequently. The mechanism of structural relaxation in Co-Fe-B amorphous films induced by thermomagnetic treatment was discussed.

2. Material and Methods

Co-Fe-B films were prepared by electroless plating on microscope glass slides (25 mm × 16 mm) with predeposited 5 nm thick Ni film as an active layer. The electroless plating solution utilized in this study was the mixture of cobalt sulfate heptahydrate (0.029 M), iron sulfate heptahydrate (0.009 M) as metal sources, sodium borohydride (0.13 M) as reducing agent and boron source, sodium tartrate (0.239 M) as complexing agent, ammonium sulfate (0.189 M), and sodium tetraborate (0.01 M) as additive. During the plating, the solution temperature was maintained at $30 \pm 1^\circ\text{C}$ using

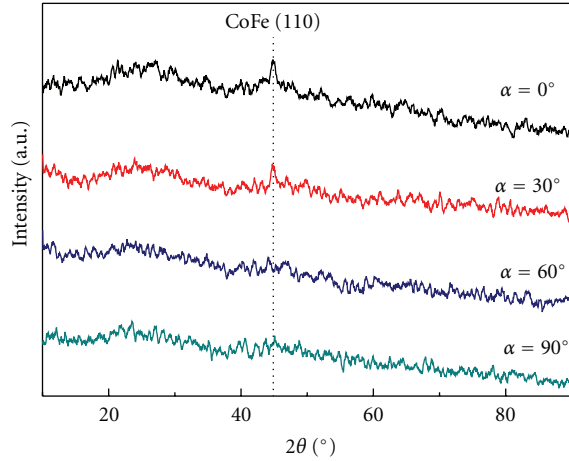


FIGURE 1: GIXRD spectra of the Co-Fe-B thin films thermomagnetically treated with different α angles.

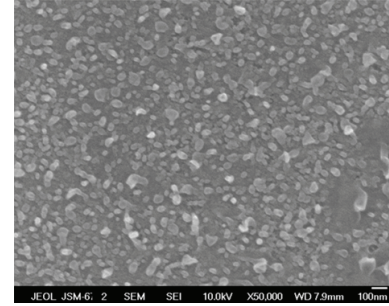
a constant temperature bath and the pH was maintained constant (12.7 ± 0.1) without agitation. After 30 min deposition, the sample was removed from the plating solution, then rinsed with distilled water several times and dried with blowing air. The as-deposited film was cut into four pieces ($12.5 \text{ mm} \times 8 \text{ mm}$) in preparation for the following treatment. Structures and magnetic properties of Co-Fe-B films of varied thickness and composition were studied. Therefore, we focus on the impact of thermomagnetic treatment at different angles on the magnetic properties of Co-Fe-B films with the optimize composition [6] and determined thickness (200 nm).

As-deposited films were then annealed in an applied magnetic field of 500 Oe, oriented differently with respect to the film normal direction at 300°C for 1 hour. In order to avoid oxidation during the heat treatment, the films were treated in pure argon gas. The longitudinal direction of all films was kept perpendicular to the field, while the film's normal direction varied from parallel to perpendicular to the field direction during the annealing process. We defined α ($0\sim 90^\circ$) as the annealing angle between the film normal direction and the magnetic field direction (corresponds to the films a–d).

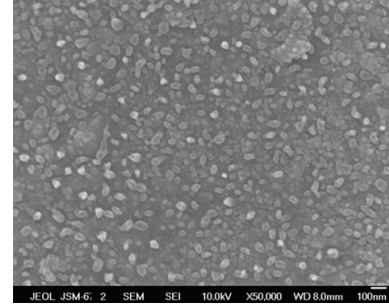
Grazing incidence X-ray diffraction (GIXRD) was carried out with the incident angle of 5° on a Philips X'Pert diffractometer with Cu $K\alpha$ radiation generated at 40 kV and 40 mA. Scanning electronic microscopy (SEM) was performed to determine the surface morphology and to estimate the film thickness from cross-sectional views. Vibrating sample magnetometer (VSM) was used to characterize the magnetic properties of the annealed Co-Fe-B films.

3. Results and Discussion

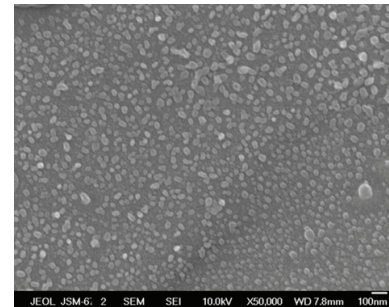
As shown in Figure 1, amorphous phase is the main component of all the films after being annealed at different magnetic field directions. When the film normal direction and the magnetic field direction approach to be parallel, that is, $\alpha \leq 30^\circ$, a weak peak can be found around 44.8° , which is



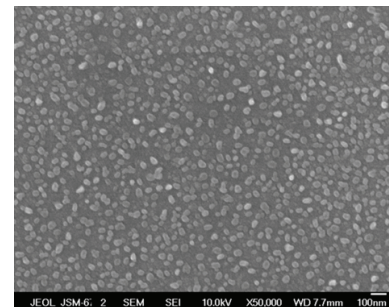
(a)



(b)



(c)



(d)

FIGURE 2: SEM photos of the Co-Fe-B thin films thermomagnetically treated with different α angles, (a) $\alpha = 0^\circ$, (b) $\alpha = 30^\circ$, (c) $\alpha = 60^\circ$, and (d) $\alpha = 90^\circ$.

corresponding to CoFe (110) diffraction. The crystallization phase generally has magnetic anisotropy, which is different from amorphous. It is suggested forming crystalline bcc CoFe phase was formed in amorphous matrix. With the change of magnetic field direction, when $\alpha \geq 60^\circ$, films as-annealed are fully amorphous.

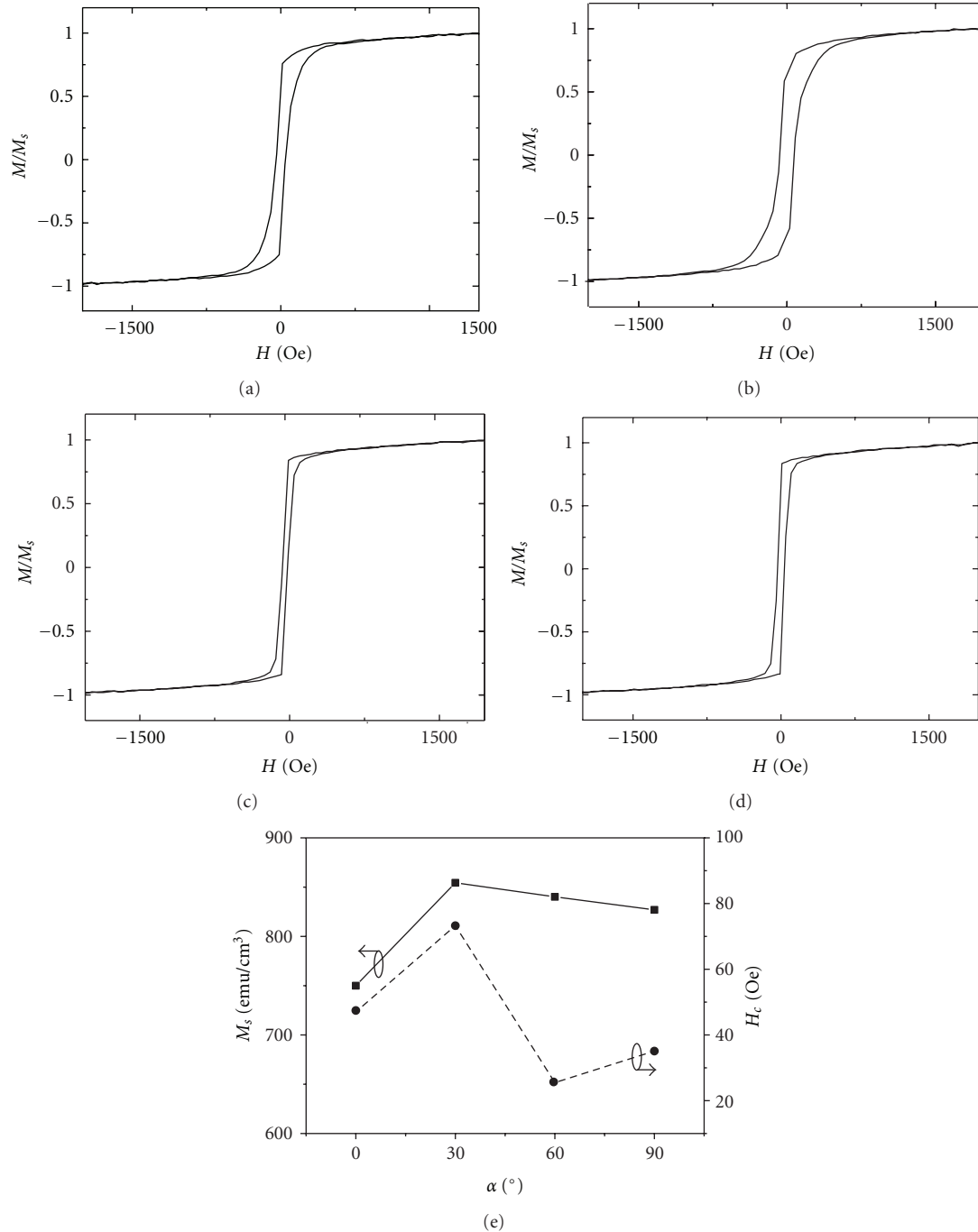


FIGURE 3: In-plane magnetic hysteresis curves of the Co-Fe-B thin films thermomagnetically treated with different α angles, (a) $\alpha = 0^\circ$, (b) $\alpha = 30^\circ$, (c) $\alpha = 60^\circ$, (d) $\alpha = 90^\circ$, and (e) the dependences of M_s and H_c on α angle.

Figure 2 shows the SEM photographs of the Co-Fe-B thin films after thermomagnetic treatment at different angles. It is clear that some tiny particles can be found in all films. The variety of the films' surface morphology after magnetic heat treatment results from local structure relaxation. Under the condition of magnetic field, the short-range order of the amorphous film is enhanced, and the free volume density of the film decreases, resulting in the fluctuation of the surface morphology of the films. For the amorphous films annealed

at different magnetic field direction, the conditions of short-range order and bond structure are different, leading to the differences on the surface morphology of the films treated at different magnetic field directions. Energy dispersion X-ray (EDX) analysis shows that the atomic ratio of Co and Fe is 2:1.

The in-plane magnetic hysteresis curves of the Co-Fe-B thin films thermomagnetically treated with different α angle are shown in Figure 3. When $\alpha \leq 30^\circ$, the films display

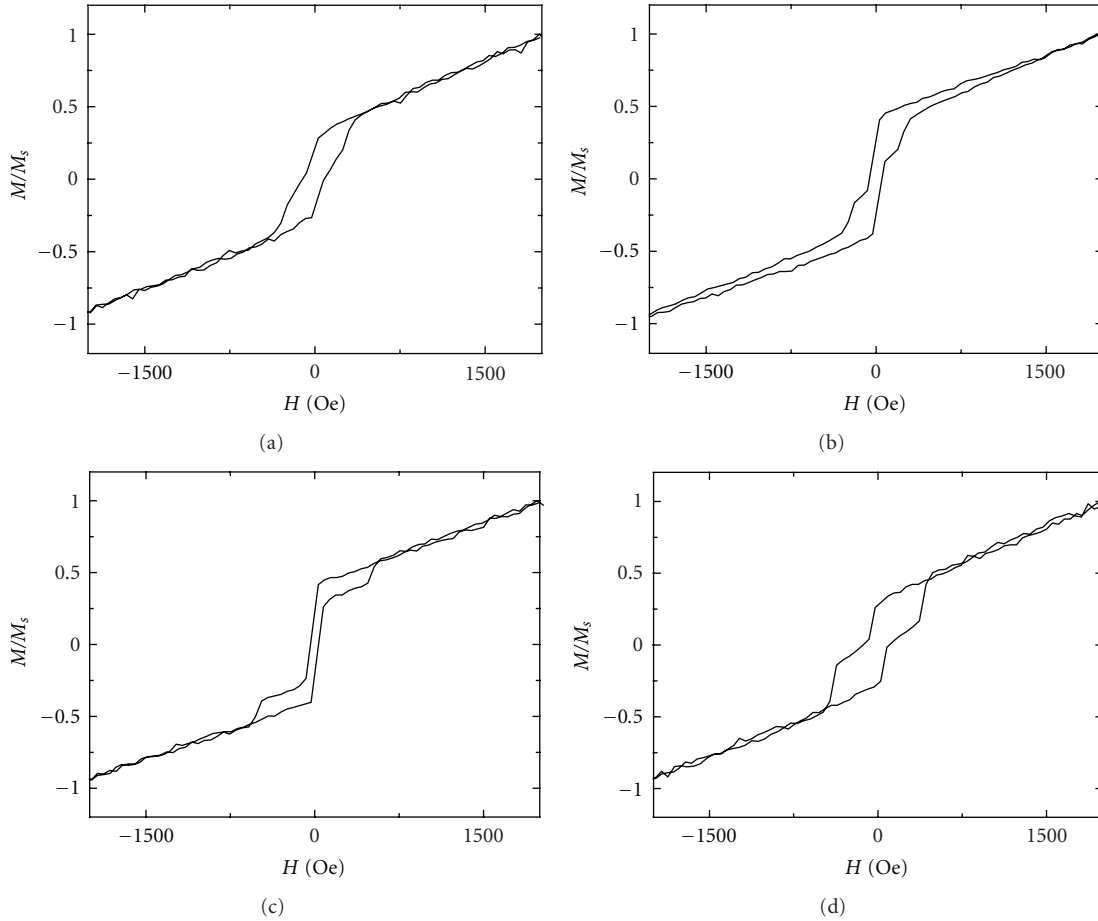


FIGURE 4: Out-of-plane magnetic hysteresis curves of the Co-Fe-B thin films thermomagnetically treated with different α angles, (a) $\alpha = 0^\circ$, (b) $\alpha = 30^\circ$, (c) $\alpha = 60^\circ$, and (d) $\alpha = 90^\circ$.

weakly wasp-waisted hysteresis loops. The shapes of loops are approximately square when $\alpha \geq 60^\circ$. Figure 3(e) shows the variation of saturation magnetization and the coercivity as a function of annealing angle measured along the in-plane direction. The maximum of the saturation magnetization and the coercivity reached 854 emu/cc and 73 Oe when $\alpha = 30^\circ$, respectively. As the annealing angle increased above 30° , they all descended. Especially, the film annealed at 60° exhibits lower coercivity and higher saturation magnetization.

As illustrated in Figure 4, the out-of-plane hysteresis loops of the Co-Fe-B thin films thermomagnetically treated with different α angles are very different from those of in-plane ones. They also exhibit wasp-waisted shape within the small range of applied magnetic field (± 500 Oe). With the annealing angle increases from 0° to 90° , the wasp-waisted shape becomes more and more obvious.

Thermal annealing of amorphous materials at the temperature well below the crystallization temperature will lead to the change of structure towards a more relaxed state [14]. In the process of structural relaxation, applied magnetic field can affect the anisotropy of the relaxed regions with high magnetization [15]. The easy direction of Fe-Co rich region tends to be parallel to the applied magnetic field to reduce

the energy. However, the effective magnetic field in the film is affected by the demagnetization effect in the case of thin film state [16].

In the case of thin films, when α angle is small (i.e., $\alpha \leq 30^\circ$) for the thermomagnetic treatment, the in-plane applied magnetic field is small, and out-of-plane magnetic field is small as well because of the demagnetization effect. This leads to weak anisotropy in the relaxed regions. However, the effect of in-plane demagnetization field can be neglected when the applied magnetic field is in-plane during thermomagnetic treatment. The in-plane magnetic field applied in the thermomagnetic treatment increases with α angle increasing. The optimum soft magnetic properties obtained in the film thermomagnetically treated with the incline angle of 60° is the result of the competition between the demagnetization effect and the driving force of annealing magnetic field.

On the basis of the above analysis, it can be concluded that the large magnetic anisotropy induced by thermomagnetic treatment is mainly in-plane when α angle is larger. However, the out-of-plane magnetic anisotropy may be weak at small α angle due to the demagnetization effect. When the hysteresis loops were measured in the in-plane direction, the loops are normal ones with square-like shape. Because large

anisotropy is mainly parallel to the measurement direction. The weak wasp-waisted shape in-plane hysteresis loop at low value of α angle may be caused by the weak anisotropy in the out-of-plane direction [17]. When the hysteresis loops are measured in the out-of-plane direction, the loops for the film thermomagnetically treated with high α angle exhibits more obvious wasp-waisted shape, because of the large magnetic anisotropy in the in-plane direction. The anisotropy constant of Co-Fe-B with an extremely high Curie temperature (about 1300 K [18]) is big. Therefore, it is hard to form a perpendicular magnetic anisotropy and to get the out-of-plane magnetization saturated (Figures 4(a)–4(d)). The shape of hysteresis loop merely varied under small magnetic field.

4. Conclusions

Co-Fe-B thin films were prepared by electroless deposition successfully. The deposits were annealed in an applied magnetic field of 500 Oe being oriented differently with respect to the direction of film normal at 300°C for 1 hour. It is found weak crystallized CoFe phase exist in annealed films. The surface morphologies of annealed films depended strongly on annealing angle.

It is found that magnetic field annealing is an efficient way to obtain different anisotropy in amorphous Co-Fe-B films. In the occasion of small magnetic field annealing, it is found that the optimum soft magnetic properties were not obtained when annealing field was completely parallel to the film plane, but with a little incline ($\alpha = 60^\circ$).

References

- [1] T. Yokoshima, S. Nakamura, D. Kaneko, T. Osaka, S. Takefusa, and A. Tanaka, "Micropattern formation for magnetic recording head using electroless CoFeB deposition," *Journal of the Electrochemical Society*, vol. 149, no. 8, pp. C375–C382, 2002.
- [2] D. D. Djayaprawira, K. Tsunekawa, M. Nagai, H. Maehara, S. Yamagata, N. Watanabe et al., "230% room-temperature magnetoresistance in CoFeB/MgO/CoFeB magnetic tunnel junctions," *Applied Physics Letters*, vol. 86, Article ID 092502, 3 pages, 2005.
- [3] M. Munakata, S. I. Aoqui, and M. Yagi, "B-concentration dependence on anisotropy field of CoFeB thin film for gigahertz frequency use," *IEEE Transactions on Magnetics*, vol. 41, no. 10, pp. 3262–3264, 2005.
- [4] R. D. Gomez, J. S. Ma, A. Arkilic, S. H. Chung, and C. Krafft, "Vortex-antivortex creation and annihilation on CoFeB cross-tie patterns," *Journal of Applied Physics*, vol. 109, no. 7, Article ID 07D310, 2011.
- [5] S. A. Manuilov, A. M. Grishin, and M. Munakata, "Ferromagnetic resonance, magnetic susceptibility, and transformation of domain structure in CoFeB film with growth induced anisotropy," *Journal of Applied Physics*, vol. 109, no. 8, Article ID 083926, 2011.
- [6] C. H. Liu, H. H. He, X. Shen, Y. F. He, and H. H. Li, "Soft magnetic peculiarities of the electroless magnetic loss CoFeB films," *Materials Science and Engineering B*, vol. 137, no. 1–3, pp. 103–107, 2007.
- [7] S. Chikazumi and T. Oomura, "On the origin of magnetic anisotropy induced by magnetic annealing," *Journal of the Physical Society of Japan*, vol. 10, no. 10, pp. 842–849, 1955.
- [8] B. S. Berry and W. C. Pritchett, "Magnetic annealing and directional ordering of an amorphous ferromagnetic alloy," *Physical Review Letters*, vol. 34, no. 16, pp. 1022–1025, 1975.
- [9] Y. Yoshizawa and K. Yamauchi, "Effects of magnetic field annealing on magnetic properties in ultrafine crystalline Fe-Cu-Nb-Si-B alloys," *IEEE Transactions on Magnetics*, vol. 25, no. 5, pp. 3324–3326, 1989.
- [10] N. Masahashi, M. Matsuo, and K. Watanabe, "Development of preferred orientation in annealing of Fe-3.25% Si in a high magnetic field," *Journal of Materials Research*, vol. 13, no. 2, pp. 457–461, 1998.
- [11] Y. Yoshizawa, S. Oguma, and K. Yamauchi, "New Fe-based soft magnetic alloys composed of ultrafine grain structure," *Journal of Applied Physics*, vol. 64, no. 10, pp. 6044–6046, 1988.
- [12] S. L. Wang and L. L. Hong, "Effect of the heat treatment on the structure and the properties of the electroless Co-Fe-B alloy," *Journal of Alloys and Compounds*, vol. 429, no. 1–2, pp. 99–103, 2007.
- [13] Y. H. Wang, W. C. Chen, S. Y. Yang et al., "Interfacial and annealing effects on magnetic properties of CoFeB thin films," *Journal of Applied Physics*, vol. 99, no. 8, Article ID 08M307, 2006.
- [14] H. S. Chen, "Glassy metals," *Reports on Progress in Physics*, vol. 43, no. 4, article 001, pp. 353–432, 1980.
- [15] H. Kronmüller, "Magnetic aftereffects, induced anisotropies, and the role of two-level systems in amorphous alloys," *Journal of Magnetism and Magnetic Materials*, vol. 41, pp. 366–375, 1984.
- [16] O. De Abril, M. D. C. Sánchez, and C. Aroca, "The effect of the in-plane demagnetizing field on films with weak perpendicular magnetic anisotropy," *Journal of Applied Physics*, vol. 100, no. 6, Article ID 063904, 2006.
- [17] Q. Gao, G. Hong, J. Ni, W. Wang, J. Tang, and J. He, "Uniaxial anisotropy and novel magnetic behaviors of CoFe₂O₄ nanoparticles prepared in a magnetic field," *Journal of Applied Physics*, vol. 105, no. 7, Article ID 07A516, 2009.
- [18] L. Heyne, M. Klaui, D. Backes, P. Mohrke, T. A. Moore, J. G. Kimling et al., "Direct imaging of current-induced domain wall motion in CoFeB structures," *Journal of Applied Physics*, vol. 103, article 07D928, 2008.

Research Article

Zinc Vacancy-Induced Room-Temperature Ferromagnetism in Undoped ZnO Thin Films

Hongtao Ren,¹ Gang Xiang,¹ Gangxu Gu,¹ Xi Zhang,¹ Wenjun Wang,² Peng Zhang,³ Baoyi Wang,³ and Xingzhong Cao³

¹Department of Physics and Key Laboratory for Radiation Physics and Technology of Ministry of Education, Sichuan University, Chengdu 610064, China

²Institute of Physics and Center for Condensed Matter Physics, Chinese Academy of Sciences, Beijing 100080, China

³Key Laboratory of Nuclear Analytical Techniques, Institute of High Energy Physics, Chinese Academy of Sciences, Beijing 100049, China

Correspondence should be addressed to Gang Xiang, gxiang@scu.edu.cn and Xi Zhang, xizhang@scu.edu.cn

Received 29 June 2012; Accepted 19 July 2012

Academic Editor: Weichang Hao

Copyright © 2012 Hongtao Ren et al. This is an open access article distributed under the Creative Commons Attribution License, which permits unrestricted use, distribution, and reproduction in any medium, provided the original work is properly cited.

Undoped ZnO thin films are prepared by polymer-assisted deposition (PAD) and treated by postannealing at different temperatures in oxygen or forming gases (95% Ar + 5% H₂). All the samples exhibit ferromagnetism at room temperature (RT). SQUID and positron annihilation measurements show that post-annealing treatments greatly enhance the magnetizations in undoped ZnO samples, and there is a positive correlation between the magnetization and zinc vacancies in the ZnO thin films. XPS measurements indicate that annealing also induces oxygen vacancies that have no direct relationship with ferromagnetism. Further analysis of the results suggests that the ferromagnetism in undoped ZnO is induced by Zn vacancies.

1. Introduction

The dilute magnetic semiconductors (DMSs) have attracted increasing attention due to the potential applications in spintronic devices in recent years [1, 2]. Since the room-temperature (RT) ferromagnetism in Co-doped ZnO has been predicted by Dietl et al. with the Zener model of ferromagnetism [3], extensive theoretical and experimental studies have been performed on ZnO [4–12]. Various mechanisms, such as intrinsic defects [4–6] (zinc vacancy (V_{Zn}), oxygen vacancy (V_O), etc.), extrinsic defects [7–10] (TM and non-TM dopants), and the correlation of intrinsic and extrinsic defects [11, 12] have been declared to induce the room-temperature (RT) ferromagnetism in ZnO. However, magnetic properties of ZnO still remain a heavily controversial issue: the theoretical and experimental results were often found contradictory to each other; the origin of ferromagnetism and the influence of the complex interactions between different defects on magnetic properties of ZnO are still not well understood. Among them, the

ferromagnetism induced by intrinsic defects, such as Zn vacancies and oxygen vacancies, and the correlation between the magnetic properties and intrinsic defects are of particular interest, since intrinsic-defects-induced mechanism may suggest new pathways for preparing ZnO-based spintronic devices and the physics of the simple system without dopants may be more straightforward.

In this paper, we systematically investigated the correlation between the magnetic properties and the intrinsic defects in undoped ZnO. Undoped ZnO thin films were first grown on (0001) sapphire (Al₂O₃) substrates by polymer-assisted deposition (PAD) [13, 14] and then treated by postannealing at different temperatures in different atmospheres. We then measured the structures and the magnetic properties of the ZnO thin films.

The crystalline structure of the films was characterized by using X-ray diffractometer (XRD) with Cu K α radiation. The morphology of the samples was observed by a field emission scanning electronic microscopy (SEM). Magnetic measurements were performed using superconducting

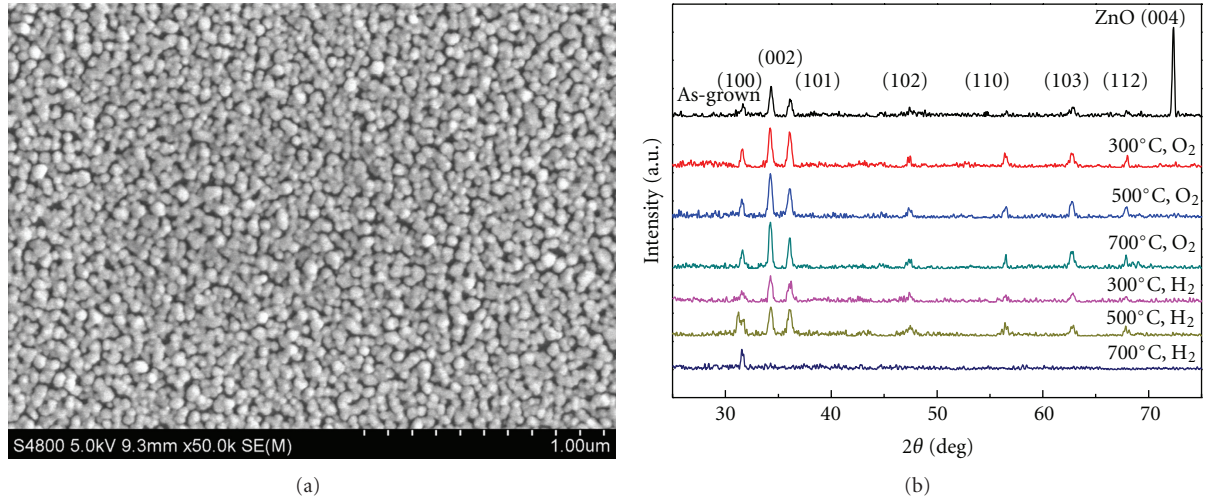


FIGURE 1: (a) SEM of nanocrystalline ZnO thin films (b) XRD spectra of ZnO thin films: as-grown, annealed at different temperatures in O_2 or H_2 atmosphere.

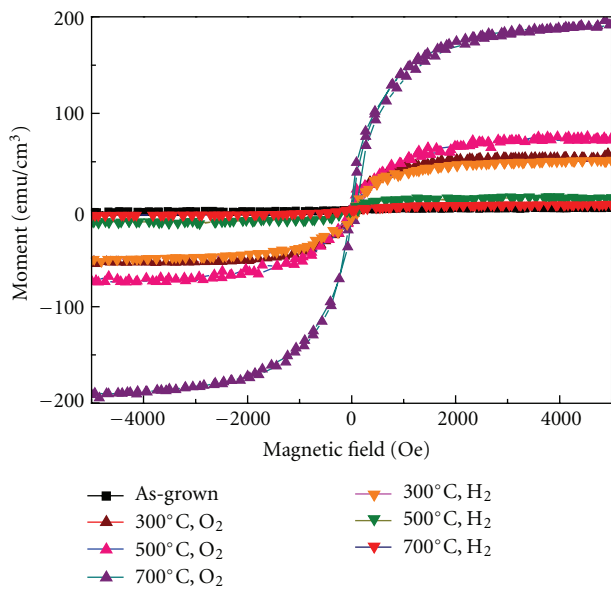


FIGURE 2: (a) M versus H of undoped ZnO thin films before and after annealing at different temperatures in H_2 gas. (b) M versus H of undoped ZnO thin films before and after annealing at different temperatures in O_2 gas.

quantum interference device (SQUID) magnetometer with the magnetic field applied parallel to the film surface at 300 K. The chemical state of oxygen was measured by X-ray photoelectron spectroscopy (XPS). Cation vacancies were detected by positron annihilation spectroscopy (PAS).

2. Experimental

ZnO thin films were prepared by PAD of Zinc nitrate hexahydrate (purity $\geq 99.0\%$) and ethylene imine polymer (purity = 99%). To prepare Zn-polymer solution, 2.5 g zinc

nitrate hexahydrate was dissolved in 40 ml deionized water, and then 2 g ethylene imine polymer was added into the mixed solution. After stirring, the solution was purified by Amicon Ultra Centrifugal Filters with a 10,000 molar weight-off membrane. The solution was spin coated on (0001) R-cut sapphire substrates at the rates of ~ 600 rpm for 18 s and ~ 2600 rpm for 30 s. The resultant coatings were gradually heated from room temperature to 500°C and stayed at that temperature for a period of about 1 h to burn out the polymer under an oxygen atmosphere. These as-grown films, which served as the precursors, were put into a horizontal quartz tube furnace for 3 minutes of heating at 900°C . The heating and cooling rates were 75°C/s for all the cases. After deposition, the samples were treated by post-annealing in oxygen gas or forming gas of 5% H_2 and 95% Ar gases (we use H_2 to denote the forming gas for simplicity later) at 300, 500 and 700°C for 30 minutes.

3. Results and Discussions

We first measured the structure and morphology of the ZnO samples. Figure 1(a) shows that the prepared as-grown samples are nanocrystalline ZnO thin films. The average crystallite size of the samples is about 50 nm and the film thickness is about 100 nm. No crack or obvious protuberance can be observed within the visual field. As shown in Figure 2(b), XRD results indicate that all the thin films are polycrystalline wurtzite-type ZnO and no second peaks can be observed. After post-annealing, the (004) main peak in as-grown sample disappears, indicating formation of more defects in ZnO samples. The diffraction peaks of samples annealed in O_2 at different temperatures are strong and similar to each other, while those of samples annealed in H_2 at 700°C get much weaker, indicating the deteriorated quality of the sample. This is probably because H_2 is a reducing gas and taking more amounts of oxygen atoms away from the sample at higher temperatures.

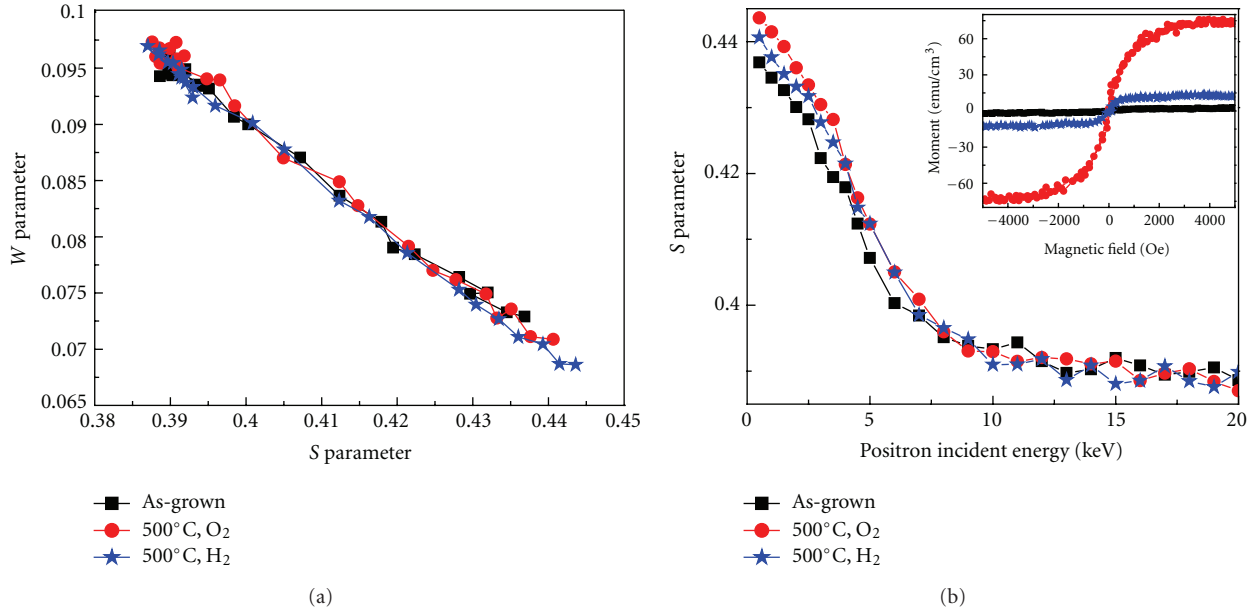


FIGURE 3: (a) Doppler-broadening parameter “S” as a function of incident positron energy for the ZnO samples: as-grown, annealed at 500°C in O₂ and annealed at 500°C in H₂ atmosphere. (b) The spectra of W parameter versus S parameter.

The magnetization of the undoped ZnO thin films was measured by SQUID at room temperature, as shown in Figure 2. All the samples exhibit a clear hysteresis loop, indicating that these films are ferromagnetic at RT. The as-grown undoped sample shows weak ferromagnetism ($M \sim 2.5 \text{ emu/cm}^3$). There are reports indicating that surface defects of the oxide thin film could cause ferromagnetism [15, 16]. After post-annealing treatment at different temperatures in O₂ or H₂ gas, ferromagnetic ordering of all the samples was improved. As shown in Figure 2, in the case of annealing in O₂ gas, the measured magnetization increases as annealing temperature increases, while in the case of annealing in H₂ gas, the magnetization decreases as annealing temperature increases. However, the annealing effect at the same temperature in O₂ atmosphere is always stronger than that in H₂ in terms of enhancement of ferromagnetism in undoped ZnO thin films. Since annealing in oxygen atmosphere tends to prevent the formation of oxygen vacancies but promote the formation of Zn vacancies while annealing in hydrogen the opposite, the results above suggest that the enhancement of ferromagnetism of undoped ZnO thin films is related to the Zn vacancies in the sample.

In order to confirm the Zinc vacancies concentration, we carried out the positron annihilation analysis (PAS) measurements for a series of samples: as-grown, annealed at 500°C in O₂ gas and annealed at 500°C in H₂ gas. As shown in Figure 3(a), the linear S-W spectra suggest that there is only one type of cation vacancies, that is, zinc vacancies in the samples. The relationship between the S values and positrons energy for the films is shown in Figure 3(b). The increase in the S values in the annealed samples indicates that annealing introduces more Zn vacancies. In addition, the S value in the sample annealed in O₂ is bigger than that

annealed in H₂ at the same temperature. Since the magnetization of annealed samples increases and the magnetization of the samples annealed in O₂ is bigger than that annealed in H₂ at the same temperature, as shown in the insert of Figure 3(b), we see clearly positive correlation between the Zn vacancies and the magnetization of the undoped ZnO samples. In fact, theoretical studies show that the ferromagnetism can be induced by Zn vacancies instead of oxygen vacancies, in ZnO samples, and the magnetic moment mainly arises from the unpaired 2p electrons at O sites surrounding the Zn vacancies [17]. Therefore the ferromagnetic ordering can be enhanced by introducing more Zn vacancies.

On the other hand, we also investigate the variation of oxygen vacancies in the samples using XPS analysis. XPS O 1s scans of typical ZnO thin films are shown in Figures 4(a)–4(c). Two Gaussians were fitted to separate oxygen species. Then the profile can be fit by two symmetrical peaks, which are normally assigned as low-binding-energy component (LBEC) and high-binding-energy component (HBEC). Since the HBEC peak develops with increasing loss of oxygen, the development of the HBEC peak obviously leads to the asymmetry of the main peak. Changes in the ratios of HBEC/LBEC peak may result from the variations in the concentration of oxygen vacancies.

The variations of oxygen vacancies and the magnetization in the samples are shown in Figures 4(d)–4(f). As shown in Figure 4(e), when annealing in H₂, the magnetization decreases while oxygen concentration increases as annealing temperature increases. The negative correlation between the magnetization and the oxygen vacancies indicates that oxygen cannot be the origin of the ferromagnetism in these samples. In the case of annealing in hydrogen atmosphere, the oxygen vacancies are preferred, which results in higher

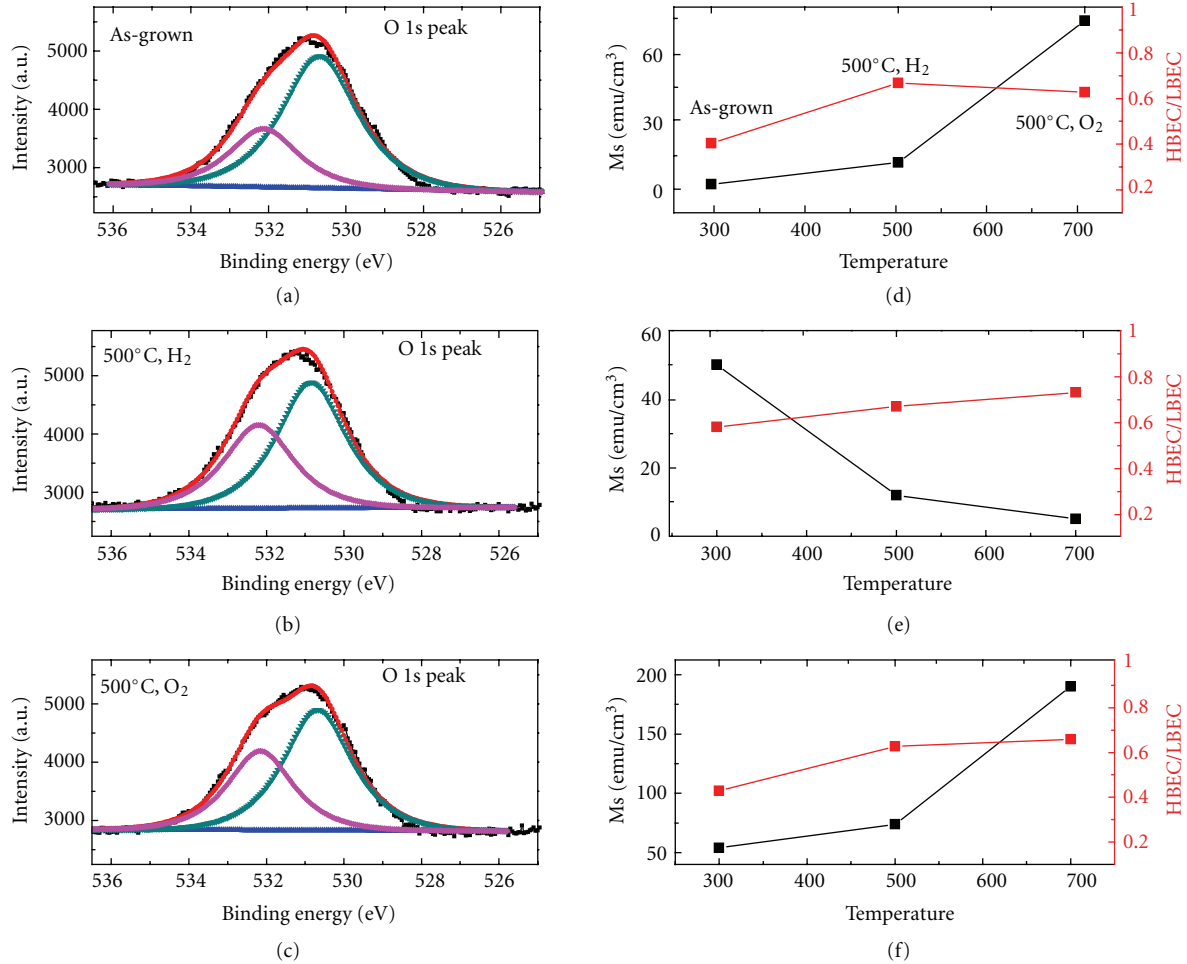


FIGURE 4: (a–c) Normalized XPS O 1s scans of ZnO samples: as-grown, annealed at 500°C in H₂ atmosphere, and annealed at 500°C in O₂ atmosphere; (d) The ratio of HBEC/LBEC peak and magnetization of as-grown, annealed (500°C + H₂), and annealed (500°C + O₂) ZnO samples; (e–f) Corresponding ratios of HBEC/LBEC peak and magnetizations of samples annealed at different temperatures in H₂ and O₂ atmosphere, respectively.

oxygen concentration than the case of annealing in oxygen atmosphere, as shown in Figure 4(d). Since the oxygen vacancies have no positive contribution to the ferromagnetism and the reducing H₂ gas may result in deterioration of sample quality at high temperature, the magnetization decreases as the annealing temperature increases. As shown in Figure 4(f), when annealing in O₂, both the magnetization and the oxygen vacancies increase as the annealing temperature increases, but the increasing rate of magnetization is higher than that of oxygen vacancies. This can be understood as follows: annealing in oxygen atmosphere promotes the formation of Zn vacancies, so Zn vacancies increase more rapidly than oxygen vacancies; since the ferromagnetism is induced by Zn vacancies, the magnetization also increase more rapidly than that of oxygen vacancies.

4. Conclusions

In summary, we have grown undoped ZnO thin films by polymer-assisted deposition. All the ZnO thin films show

RT ferromagnetism. The enhancement of magnetization is observed after the samples are annealed at different temperatures in O₂ or H₂ gas. The clearly positive correlation between the magnetization and Zn vacancies indicates that Zinc vacancies are the origin of the ferromagnetism. Our results may be useful for the design and fabrication of spintronic devices based on ZnO DMS without dopants.

Acknowledgments

This work was supported by the Natural Science Foundation of China (NSFC) through Grant nos. 11004141 and 11174212 and by the Program for New Century Excellent Talents in University (NCET) through Grant no. 11-0351.

References

- [1] I. Žutić, J. Fabian, and S. D. Sarma, “Spintronics: fundamentals and applications,” *Reviews of Modern Physics*, vol. 76, no. 2, pp. 323–410, 2004.

- [2] S. A. Wolf, D. D. Awschalom, R. A. Buhrman et al., “Spintronics: a spin-based electronics vision for the future,” *Science*, vol. 294, no. 5546, pp. 1488–1495, 2001.
- [3] T. Dietl, T. Dietl, H. Ohno, F. Matsukura, J. Cibert, and D. Ferrand, “Zener model description of ferromagnetism in zinc-blende magnetic semiconductors,” *Science*, vol. 287, no. 5455, pp. 1019–1022, 2000.
- [4] M. Khalid, M. Ziese, A. Setzer et al., “Defect-induced magnetic order in pure ZnO films,” *Physical Review B*, vol. 80, no. 3, Article ID 035331, 2009.
- [5] G. Xing, D. Wang, J. Yi et al., “Correlated d^0 ferromagnetism and photoluminescence in undoped ZnO nanowires,” *Applied Physics Letters*, vol. 96, Article ID 112511, 3 pages, 2010.
- [6] P. Zhan, W. Wang, C. Liu et al., “Oxygen vacancy-induced ferromagnetism in un-doped ZnO thin films,” *Journal of Applied Physics*, vol. 111, no. 3, Article ID 033501, 5 pages, 2012.
- [7] K. Ueda, H. Tabata, and T. Kawai, “Magnetic and electric properties of transition-metal-doped ZnO films,” *Applied Physics Letters*, vol. 79, no. 7, pp. 988–990, 2001.
- [8] J. M. D. Coey, M. Venkatesan, and C. B. Fitzgerald, “Donor impurity band exchange in dilute ferromagnetic oxides,” *Nature Materials*, vol. 4, no. 2, pp. 173–179, 2005.
- [9] P. Sati, C. Deparis, C. Morhain, S. Schäfer, and A. Stepanov, “Antiferromagnetic interactions in single crystalline $\text{Zn}_{1-x}\text{Co}_x\text{O}$ thin films,” *Physical Review Letters*, vol. 98, no. 13, Article ID 137204, 4 pages, 2007.
- [10] G. Gu, G. Xiang, and J. Luo, “Magnetism in transition-metal-doped ZnO: a first-principles study,” *Journal of Applied Physics*, vol. 112, no. 2, Article ID 023913, 5 pages, 2012.
- [11] J. B. Yi, C. C. Lim, G. Z. Xing et al., “Ferromagnetism in dilute magnetic semiconductors through defect engineering: Li-Doped ZnO,” *Physical Review Letters*, vol. 104, no. 13, Article ID 137201, 4 pages, 2010.
- [12] J.-J. Li, W.-C. Hao, H.-Z. Xu, and T.-M. Wang, “Variation of structural and magnetic properties with Co-doping in $\text{Zn}_{1-x}\text{Co}_x\text{O}$ nanocrystals,” *Journal of Applied Physics*, vol. 105, no. 5, Article ID 053907, 2009.
- [13] Q. X. Jia, T. M. McCleskey, A. K. Burrell et al., “Polymer-assisted deposition of metal-oxide films,” *Nature Materials*, vol. 3, no. 8, pp. 529–532, 2004.
- [14] A. K. Burrell, T. Mark McCleskey, and Q. X. Jia, “Polymer assisted deposition,” *Chemical Communications*, no. 11, pp. 1271–1277, 2008.
- [15] N. Sanchez, S. Gallego, and M. C. Muñoz, “Magnetic states at the oxygen surfaces of ZnO and Co-doped ZnO,” *Physical Review Letters*, vol. 101, no. 6, Article ID 067206, 2008.
- [16] S. M. M. Yee, D. A. Crandles, and L. V. Goncharova, “Ferromagnetism on the unpolished surfaces of single crystal metal oxide substrates,” *Journal of Applied Physics*, vol. 110, no. 3, Article ID 033906, 6 pages, 2011.
- [17] Q. Wang, Q. Sun, G. Chen, Y. Kawazoe, and P. Jena, “Vacancy-induced magnetism in ZnO thin films and nanowires,” *Physical Review B*, vol. 77, no. 20, Article ID 205411, 7 pages, 2008.

Research Article

2D Simulation of Nd₂Fe₁₄B/ α -Fe Nanocomposite Magnets with Random Grain Distributions Generated by a Monte Carlo Procedure

Nguyen Xuan Truong, Nguyen Trung Hieu, Vu Hong Ky, and Nguyen Van Vuong

Institute of Materials Science, Vietnam Academy of Science and Technology, 18 Hoang Quoc Viet, Cau Giay, Ha Noi 10000, Vietnam

Correspondence should be addressed to Nguyen Van Vuong, vuongnv@ims.vast.ac.vn

Received 17 May 2012; Accepted 1 July 2012

Academic Editor: Yi Du

Copyright © 2012 Nguyen Xuan Truong et al. This is an open access article distributed under the Creative Commons Attribution License, which permits unrestricted use, distribution, and reproduction in any medium, provided the original work is properly cited.

The magnetic properties of Nd₂Fe₁₄B/ α -Fe nanocomposite magnets consisting of two nanostructured hard and soft magnetic grains assemblies were simulated for 2D case with random grain distributions generated by a Monte Carlo procedure. The effect of the soft phase volume fraction on the remanence B_r , coercivity H_c , squareness γ , and maximum energy product $(BH)_{\max}$ has been simulated for the case of Nd₂Fe₁₄B/ α -Fe nanocomposite magnets. The simulation results showed that, for the best case, the $(BH)_{\max}$ can be gained up only a several tens of percentage of the origin hard magnetic phase, but not about hundred as theoretically predicted value. The main reason of this discrepancy is due to the fact that the microstructure of real nanocomposite magnets with their random feature is deviated from the modeled microstructure required for implementing the exchange coupling interaction between hard and soft magnetic grains. The hard magnetic shell/soft magnetic core nanostructure and the magnetic field assisted melt-spinning technique seem to be prospective for future high-performance nanocomposite magnets.

1. Introduction

The preparation of nanocomposite magnets containing simultaneously both soft and hard magnetic phases is an advanced technology that can enhance maximum energy product $(BH)_{\max}$ twice and thus keeps further the tendency of the permanent magnet development which was going on over last 30 years.

In principle, for the case of nanocomposite magnets, by choosing the soft magnetic phase which has the saturation magnetization, J_s^s , higher than that of the matrix of the hard magnetic phase, J_s^h , the higher total saturation magnetization, J_s , can be achieved. Besides, for this nanocomposite magnet, the related magnetic moment reversal mechanism, which can provide the total magnetic remanence value, B_r , larger than that of the pure hard magnetic phase, B_r^h , should be taken in to account. Thus, the suitable nanostructured microstructure of the nanocomposite magnet consisting of the soft and hard magnetic phases can be obtained by controlling the magnet microstructure with regards to the

related moment reversal mechanism. In this ideal case, the coercivity H_c of the nanocomposite magnet can be remained while the maximum energy product $(BH)_{\max}$ can be enhanced up to the upper limit of $(B_r)^2/4\mu_0$.

The theory for one dimension case [1] has explained this enhancement by accounting the hardening process of fine soft magnetic particles that occurred under the exchange coupling of hard magnetic grains. This theory requires the soft magnetic grain size to be less than the critical value $\delta_{cm} = \pi(A_m/2K_h)^{1/2}$, where A_m is the soft magnetic phase exchange energy, and K_h is the hard magnetic phase anisotropy energy with $A_m = 10^{-11}$ J/m and $K_h = 2.10^6$ J/m³, respectively, for α -Fe and Nd₂Fe₁₄B.

Numerous theoretical works [2–5] have shown the ability of obtaining a large value of $(BH)_{\max}$ for modeled regular nanostructured configurations. However, up to date, the experimental studies reported that the $(BH)_{\max}$ value is still less than 200 kJ/m³ [6–20].

This paper presents 2D simulation of Nd₂Fe₁₄B/ α -Fe nanocomposite magnets by using Monte Carlo method. The

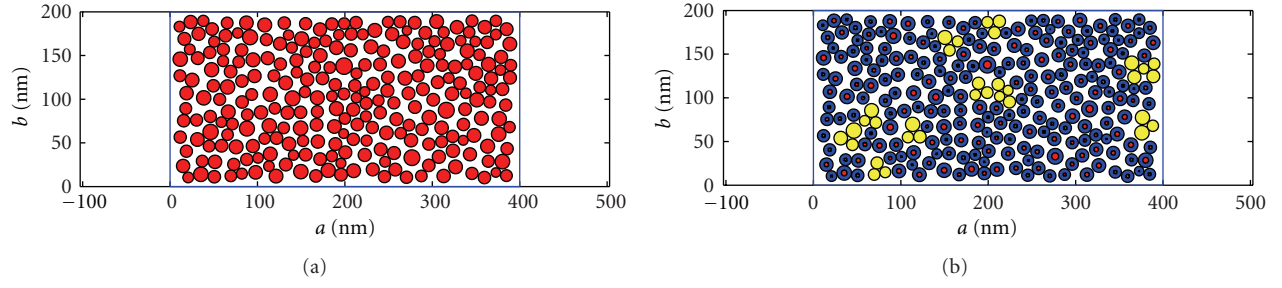


FIGURE 1: (a) The soft magnetic grains (red) are randomly distributed in the hard magnetic phase matrix (white). (b) Some sets of closed three and more soft magnetic grains (yellow) will be replaced by the one new grain with the area conservation rule. The blue parts are the parts of the soft magnetic particles hardened under the exchange coupling interactions.

TABLE 1: Magnetic parameters of hard grains, soft grains, and soft grains which are hardened under the exchange coupling interactions.

Type of grains	Saturation magnetization J_s (T)	Remanent magnetization J_r (T)	Coercivity iH_c (kA/m)	Coercivity bH_c (kA/m)	Squareness γ	Energy product $(BH)_{\max}$ (kJ/m ³)
Parts of hard magnetic grains	1.61	1.3	960	880	0.92	300
Parts of soft magnetic grains	2.15	1.978	0.0	0.0	—	0.0
Parts of soft magnetic grains which are hardened under the exchange coupling interaction	1.61	1.3	960	880	0.92	300

simulation results allow to find out the answer how difficult to prepare the high quality nanocomposite magnets. The paper also suggests the way to get high quality hard/soft magnetic two-phase nanostructure by using an external magnetic field to assist the formation of this structure.

2. 2D Simulation Algorithm

Considering the case of which the soft magnetic α -Fe grains are randomly dispersed into a two-dimensional (2D) magnet with sizes a , b of the $\text{Nd}_2\text{Fe}_{14}\text{B}$ hard magnetic phase as presented in Figure 1. The number of the soft magnetic grains is suggested to be large enough to apply Gaussian function to their grain size distribution.

The simulation algorithm is as follows.

- (i) Using the special random number generator with Gaussian statistics [21] to “spray” the assembly of the soft magnetic α -Fe grains (with the mentioned Gaussian distribution function) and the hard magnetic $\text{Nd}_2\text{Fe}_{14}\text{B}$ matrix to build up $\text{Nd}_2\text{Fe}_{14}\text{B}/\alpha$ -Fe nanocomposite microstructure.
- (ii) Inspecting all the soft magnetic grains. If three or more grains are placed closely with one another on the given distance ε , then they will be replaced by bigger grains with the effective diameter defined by the area conservation.
- (iii) The Monte Carlo probability bin of the hardening process of the soft magnetic grains is chosen on the basics of the Kneller-Hawig criterion [1]. It was

suggested that the exchange coupling interaction of the hard phase is expanded into the soft phase keeping continuously on the distance of order of the hard magnetic phase domain wall width δ_{cm} .

- (iv) In the common case, there are three kinds of grains: the origin hard magnetic grains, the original soft magnetic grains, and the hardened soft grains. Correspondingly, we have three types of the magnetization loops: the origin hard phase loop $J^h(H)$, the origin soft phase loop $J^s(H)$, and the loop $J^{hs}(H)$ of the parts of soft grains which are hardened under the exchange coupling with the hard grains. The loop $J^h(H)$ of $\text{Nd}_2\text{Fe}_{14}\text{B}$ is chosen with properties consequently observed in practice: $J_s^h = 1.61$ T, $J_r^h = 1.3$ T, $iH_c^h = 960$ kA/m, $bH_c^h = 880$ kA/m, squareness $\gamma = 0.92$, and $(BH)_{\max} = 300$ kJ/m³. The loop of hardened grains $J^{hs}(H)$ is suggested to have the intrinsic coercivity iH_c^h and the squareness γ like those of the hard magnetic phase. The remanence of the soft phase $J_r^s = \gamma J_s^s$ with $J_s^s = 2.15$ T is selected for the case of α -Fe. For clarity, the main magnetic properties of these three parts of grains are listed in the Table 1.

The total loop of the 2D nanocomposite magnet is then calculated by averaging all the loops with weighted factors of the volume fractions of three kinds mentioned above.

We present below the simulating results with $a = 80\delta_{\text{cm}}$, $b = 40\delta_{\text{cm}}$ and ε was taken to be equal $0.3\delta_{\text{cm}}$ with $\delta_{\text{cm}} = 5$ nm.

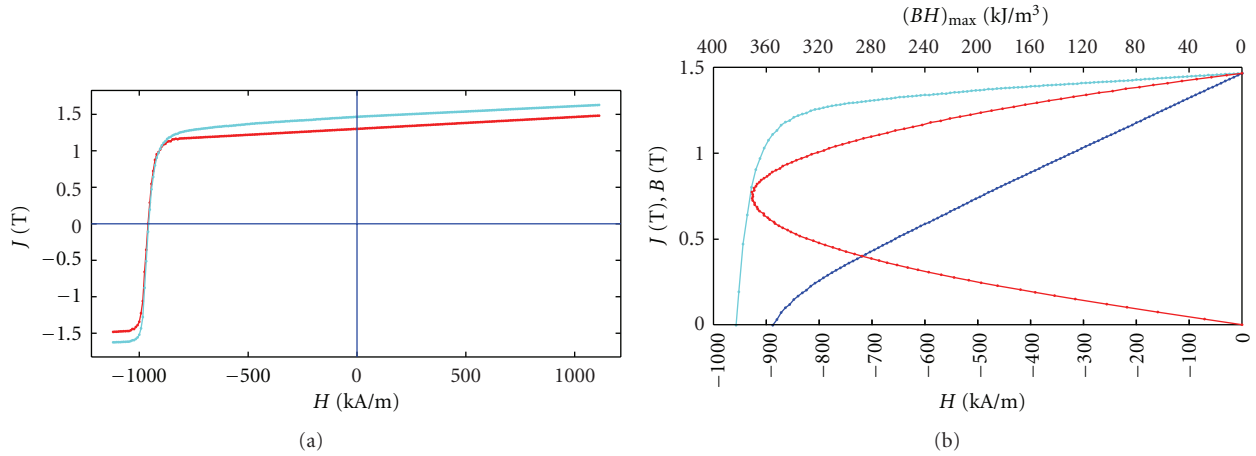


FIGURE 2: (a) The magnetization loops J^h of the magnet (sky-blue) and J^h of the origin hard phase $\text{Nd}_2\text{Fe}_{14}\text{B}$ (red); (b) the demagnetization curves $J(H)$ (sky-blue), $B(H)$ (blue), and $(BH)_{\max}$ curve (red) of the $\text{Nd}_2\text{Fe}_{14}\text{B}/\alpha\text{-Fe}$ magnet.

3. Results and Discussion

3.1. Exchange Coupling Nature. Simulation data proved the significant enhancement in magnetic properties of nanocomposite magnets in the case that a large total volume fraction of the magnets is occupied by the fine soft magnetic grains. The typical example is shown in Figures 2(a) and 2(b). In this case, the soft phase volume fraction is 33%, 700 $\alpha\text{-Fe}$ grains with the averaged particle size of 6.75 nm, and the half-width, σ , of the Gaussian distribution is 0.5.

The magnetization loop presented in Figure 2(a) shows the conventional single phase behavior, which corresponds to the fully hardening of all soft grains. The demagnetization curve together with the $(BH)_{\max}$ versus the external magnetic field curve is shown in Figure 2(b). This magnet has the remanence $J_r = 1.46$ T and $(BH)_{\max} = 370$ kJ/m³ that was enhanced by 12 and 23%, respectively, in comparison with ones of pure $\text{Nd}_2\text{Fe}_{14}\text{B}$ hard phase.

3.2. Effects of the Soft Magnetic Phase Volume Fraction on Magnetic Properties of the Nanocomposite Magnet. The dependence of magnetic properties on the soft magnetic phase volume fraction ξ is crucial for nanocomposite magnets. It is worthy to note that ξ is the function of two variables, the number and sizes of grains. For the same value of ξ , the number of grains and grain sizes can be different thus lead to the different option of implementing the Kneller-Hawig criterion, and thus lead to the dispersion of the magnetic properties of different samples prepared by different routes but with the same soft phase volume fraction. This behavior was observed in our simulation results.

The ξ -dependent magnetic properties are presented on Figure 3, and it shows clearly their complicated feature which can be summarized as follows.

- (1) A large dispersion of $(BH)_{\max}$ is observed for $\xi > 20\%$. This phenomenon might be caused mainly by the dispersion of J_r (up to 10% of its maximum

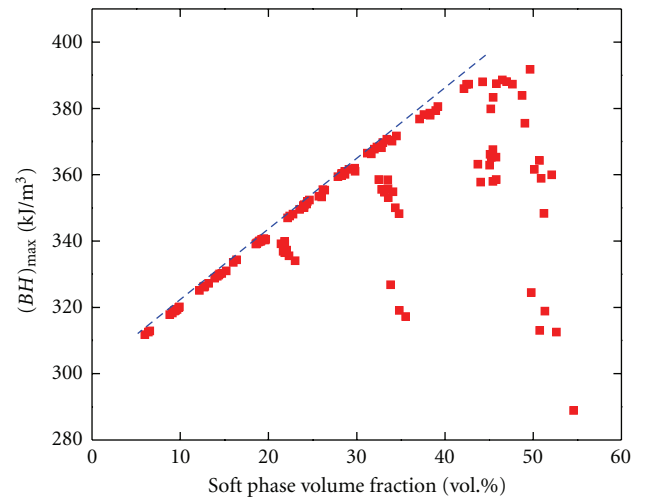


FIGURE 3: The simulated dependence of $(BH)_{\max}$ on the soft phase volume fraction ξ .

value), the dispersion of bH_c (7%), and the dispersion of iH_c (small, within 1% only).

- (2) The optimal value of ξ for the given simulated magnet is about 50%. For $\xi > 50\%$, all of the magnetic performances became worse.
- (3) For $\xi < 50\%$, the dashed curve presented in Figure 3 corresponds to the upper limit of the enhancements of the magnetic properties. So, for the given magnet, $(BH)_{\max}$ can be gained up only 30% at $\xi = 50\%$.

3.3. The Dependence of Magnetic Properties on the Grain Size. Based on the Kneller-Hawig theory, it is clear that the quality of nanocomposite magnets depends mainly on the two parameters of the soft magnetic phase: volume fraction and grain size. The volume fraction must be large enough to increase the remanence, and the grain sizes must be small enough for strengthening the hardening process.

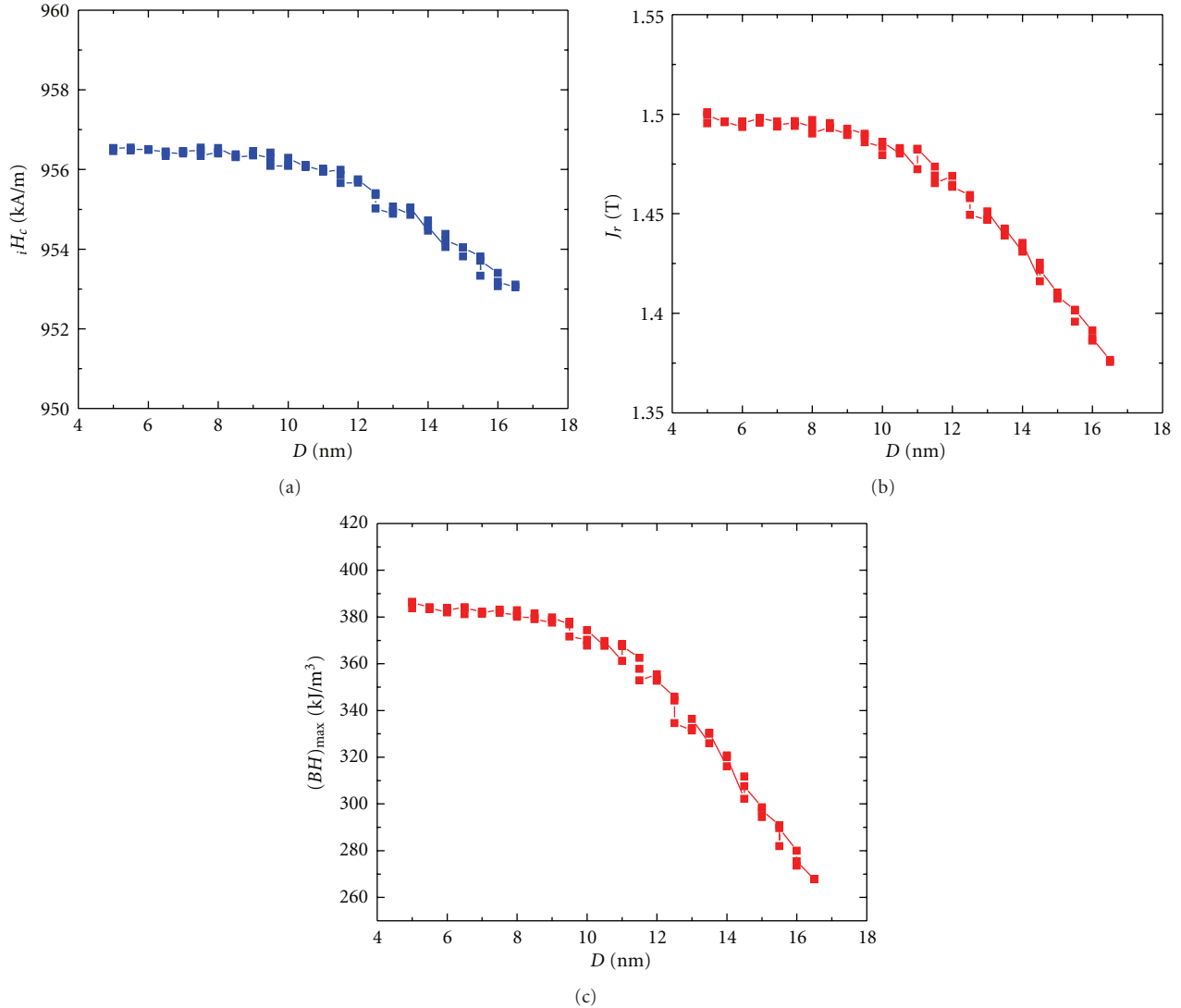


FIGURE 4: The effect of the soft phase grain size on (a) coercivity iH_c , (b) remanence J_r , and (c) $(BH)_{\max}$.

Figure 4 shows the dependence of the magnetic properties on the grain size D . The value of 40% of ξ was kept constant during the simulation, the other input data are the same as those mentioned in Section 3.1. It is interesting to note that, for the given configuration of the magnet, the intrinsic coercivity iH_c is nearly independent on the soft magnetic grain size. In contrast, the remanence J_r and the maximum energy product $(BH)_{\max}$ reach maximum values for $D < 2\delta_{\text{cm}}$ ($=10$ nm in this case) and linear dependent on the grain size in the range $D > 2\delta_{\text{cm}}$ (from 10 to 16 nm) with the slopes of -0.026 T/nm and -18.6 kJ/m³/nm, respectively.

4. The Hard Magnetic Shell/Soft Magnetic Core Nanostructure

The large dispersion observed in Figure 3 belongs to the random behavior of the distribution of soft magnetic grains

in the hard magnetic phase matrix which can form a large soft phase cluster. This effect is described in the second step of the given algorithm. In practice, the effect of increasing in randomness on soft magnetic grain size is closely related to interdiffusion of Fe/Co in the ball-milled Nd-Fe-B/ α -Fe or Sm-Co/ α -Fe systems. In melt-spun ribbons, this effect is raised up due to the splitting of the CCT (Continuous Cooling Transformation) curves of the soft and hard magnetic phases. In hot compacted nanocomposite magnets, this effect also relates to the soft phase interdiffusion process.

The effect of soft phase cluster formation disturbs the Kneller-Hawig criterion and diminishes the exchange coupling, making the nanocomposite magnet become a mixture of hard and soft phases with poor magnetic properties. To avoid this effect, one can use the nanocomposite structure of hard shell/soft core. In this configuration, the soft phase is confined inside the hard shell and the soft cluster cannot be formed. Moreover, under the protection of hard shell, instead

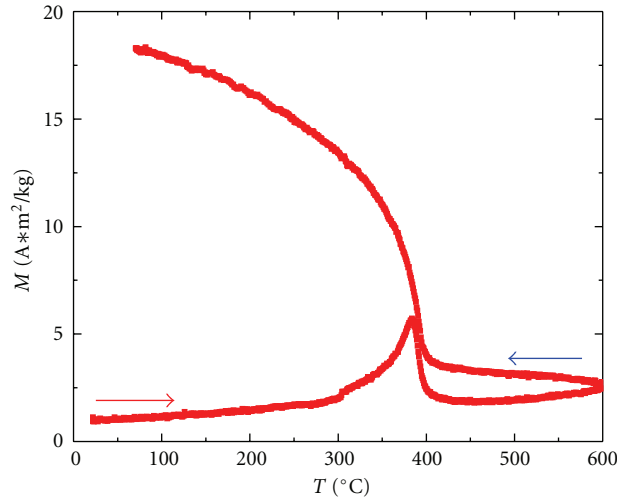


FIGURE 5: The $M(T)$ curve of the nanocomposite ribbon sample with the hard shell/soft core nanostructure. The sample was demagnetized thermally. The measuring magnetic field was 40 kA/m. The temperature was cycled between the room temperature and 600°C.

of being subjected to the external magnetic field, the soft core magnetization follows the magnetization of hard shell which allows keeping the coercivity of magnets at high values.

A technology which provides the hard magnetic shell/soft magnetic core is the magnetic field assisted melt-spinning technique [22]. For Nd-Fe-B/ α -Fe system, during the field assisted melt-spinning process, the α -Fe seeds are formed initially on the wheel surface, the hard magnetic Nd-Fe-B grains are then grown on the seed along the (001) direction and perpendicular to the ribbon free surface. As mentioned in [22], the magnetic field increases the energy inside the volume of seeds and thus decreases the critical size of seeds and, consequently, the average grain size.

In our experimental work, the hard magnetic shell/soft magnetic core nanostructure is realized by melt-spinning the alloy $\text{Nd}_{16}\text{Fe}_{76}\text{B}_8 + 40 \text{ wt.}\% \text{ Fe}_{65}\text{Co}_{35}$ with an external magnetic field, $H_{\text{ex}} = 0.32 \text{ T}$. The dependence of the magnetization on temperature was measured in the magnetic field of 40 kA/m from T_{room} to 600°C and vice versa and is presented in Figure 5. During the heating stage, the hard magnetic shell protects the soft magnetic core from the external magnetic field and the magnetization of sample is increased gradually, reaching the maximum value at the Curie temperature of the Co-containing hard magnetic phase. After reaching 400°C, the hard magnetic shell is degraded totally and as a result, only the bare soft magnetic core is left but the magnetization is kept at the value around $2 \text{ A}\cdot\text{m}^2/\text{kg}$, then increased continuously and reached the saturation when T is reaching the T_c of the soft magnetic phase. By cooling from 600°C, the magnetization that existed inside the bare soft magnetic phase is increased normally until 395°C where the hard magnetic shell restores its own hard magnetic properties.

This hard magnetic shell/soft magnetic core realizes a good exchange coupling interaction that keeps the remanence about of 0.99 T, $iH_c \sim 675 \text{ kA/m}$, and $(BH)_{\text{max}} \sim 140 \text{ kJ/m}^3$ for the ribbon melt-spun at the speed of 30 m/s. The loops of prepared ribbons melt-spun at

different wheel speeds are presented in Figure 6(a). The hysteresis curve of optimal sample at $v = 30 \text{ m/s}$ is smooth, indicating the existence of an exchange coupling between the hard and soft magnetic phases. This obtained $(BH)_{\text{max}}$ value of 140 kJ/m^3 of our work is an encouraging result and approached to that reported by other research groups [6–20] while using a rather simple preparation method.

The simple calculation in the framework of the model of spherical soft core covered entirely by the hard shell showed that the upper limit of the volume fraction of the soft phase is about 60%. The thickness of the hard magnetic shell in this case reaches about 2 nm, the size of the superparamagnetic state for $\text{Nd}_2\text{Fe}_{14}\text{B}$. This value, 60%, is greater than the limit 50% mentioned above for the case of random distribution of hard and soft grains. Thus, it is quite reasonable to expect that the optimized magnetic field assisted melt spinning method is promising to prepare high performance nanocomposite magnets.

5. Conclusion

The magnetic properties of nanocomposite magnets have been simulated with random grain distributions generated by a Monte Carlo procedure. The simulation results for the case of $\text{Nd}_2\text{Fe}_{14}\text{B}/\alpha\text{-Fe}$ showed the ability of enhancing the magnetic performance of magnet. However, the enhancement is not crucial as predicted theoretically. For the tested magnet configuration, the maximum energy product $(BH)_{\text{max}}$ can be enhanced only by about 30% of the value of the origin $\text{Nd}_2\text{Fe}_{14}\text{B}$ hard magnetic phase. The upper limit of $\alpha\text{-Fe}$ phase volume fraction is found to be about 50%, and beyond this value the $(BH)_{\text{max}}$ decreases abruptly. At the fixed values of the $\alpha\text{-Fe}$, the magnetic properties exhibit a large dispersion depending on the soft magnetic cluster formation. For further increase of $(BH)_{\text{max}}$ of nanocomposite magnets, it is suggested to use the hard shell/soft core nanostructure. This nanocomposite configuration with large

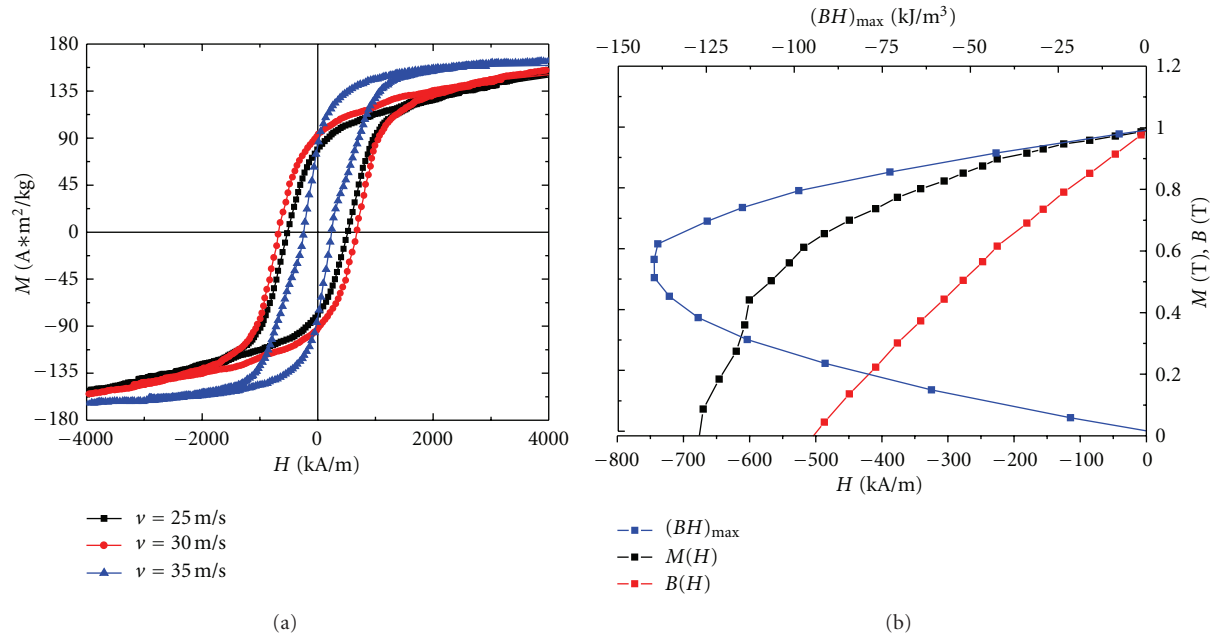


FIGURE 6: (a) The loops of the nanocomposite ribbons melt-spun at different wheel speeds, $v = 20, 25, 30$ m/s. (b) The $M(H)$ and $B(H)$ and $(BH)_{max}$ of the high performance ribbon melt-spun at the optimal wheel speed 30 m/s.

soft phase volume fraction is suggested to be prepared by means of the magnetic field assisted melt-spinning technique.

Acknowledgment

This research is supported by Vietnam's National Foundation for Science and Technology Development (NAFOSTED), code: 103.02-2010.05.

References

- [1] E. F. Kneller and R. Hawig, "The exchange-spring magnet: a new material principle for permanent magnets," *IEEE Transactions on Magnetics*, vol. 27, no. 4, pp. 3588–3600, 1991.
- [2] R. Skomski and J. M. D. Coey, "Giant energy product in nanostructured two-phase magnets," *Physical Review B*, vol. 48, no. 21, pp. 15812–15816, 1993.
- [3] T. Schrefl and J. Fidler, "Modelling of exchange-spring permanent magnets," *Journal of Magnetism and Magnetic Materials*, vol. 177–181, no. 2, pp. 970–975, 1998.
- [4] H. Fukunaga and H. Nakamura, "Computer simulation of magnetic properties of anisotropic nanocomposite magnets," *IEEE Transactions on Magnetics*, vol. 36, no. 5, pp. 3285–3287, 2000.
- [5] J. Fidler, T. Schrefl, W. Scholz, D. Suess, R. Dittrich, and M. Kirschner, "Micromagnetic modelling and magnetization processes," *Journal of Magnetism and Magnetic Materials*, vol. 272–276, pp. 641–646, 2004.
- [6] Z. Chen, Y. Zhang, G. C. Hadjipanayis, Q. Chen, and B. Ma, "Effect of wheel speed and subsequent annealing on the microstructure and magnetic properties of nanocomposite $Nd_2Fe_{14}B/\alpha-Fe$ magnets," *Journal of Magnetism and Magnetic Materials*, vol. 206, no. 1, pp. 8–16, 1999.
- [7] G. Mendoza-Suárez, J. I. Escalante-García, J. López-Cuevas, G. Vargas-Gutiérrez, H. Mancha-Molinar, and J. Mendez-Nonell, "Effect of roll speed on the magnetic properties of nanocomposite $PrFeB$ magnets prepared by melt-spinning," *Journal of Magnetism and Magnetic Materials*, vol. 206, no. 1, pp. 37–44, 1999.
- [8] A. Melsheimer, M. Seeger, and H. Kronmüller, "Influence of Co substitution in exchange coupled $NdFeB$ nanocrystalline permanent magnets," *Journal of Magnetism and Magnetic Materials*, vol. 202, no. 2, pp. 458–464, 1999.
- [9] C. J. Yang and E. B. Park, "Enhancement of magnetic properties of $Fe_3B/Nd_2Fe_{14}B$ magnet by the addition of Co," *IEEE Transactions on Magnetics*, vol. 35, no. 5, pp. 3328–3330, 1999.
- [10] W.-Y. Zhang, S.-Y. Zhang, A.-R. Yan, H.-W. Zhang, and B.-G. Shen, "Effect of the substitution of Pr for Nd on microstructure and magnetic properties of nanocomposite $Nd_2Fe_{14}B/\alpha-Fe$ magnets," *Journal of Magnetism and Magnetic Materials*, vol. 225, no. 3, pp. 389–393, 2001.
- [11] A. Arai, H. Kato, and K. Akioka, "High-energy isotropic resin bonded magnets produced from $(Nd,Dy)-(Fe,Co)-B$ nanocomposite alloys," *IEEE Transactions on Magnetics*, vol. 37, no. 4, pp. 2555–2557, 2001.
- [12] L. Shandong, D. Yaodong, B. X. Gu, T. Zongjun, and D. Youwei, "Effect of amorphous grain boundaries on the magnetic properties of B-rich nanocomposite permanent magnets," *Journal of Alloys and Compounds*, vol. 339, no. 1–2, pp. 202–206, 2002.
- [13] M. Daniil, Y. Zhang, H. Okumura, G. C. Hadjipanayis, and D. J. Sellmyer, "Effect of grain growth inhibitors on the hysteresis properties of $Nd_{10}Fe_{82}C_6B_2$ melt-spun alloys," *IEEE Transactions on Magnetics*, vol. 38, no. 5, pp. 2973–2975, 2002.

- [14] Y. Sen, S. Xiaoping, and D. Youwei, "Exchange coupled $\text{Nd}_2\text{Fe}_{14}\text{B}/\alpha\text{-Fe}$ nanocomposite magnets with fine $\alpha\text{-Fe}$ grains," *Microelectronic Engineering*, vol. 66, no. 1–4, pp. 121–127, 2003.
- [15] D. N. Brown, Z. Chen, P. Guschl, and P. Campbell, "Developments with melt spun RE-Fe-B powder for bonded magnets," *Journal of Magnetism and Magnetic Materials*, vol. 303, no. 2, pp. e371–e374, 2006.
- [16] W. Chen, X. Zhao, J. J. Hu et al., "Refinement of the microstructure and enhancement of the magnetic properties in $\alpha\text{-Fe}/(\text{Nd,Dy})_2\text{Fe}_{14}\text{B}$ nanocomposite using the two-step annealing technique," *Journal of Magnetism and Magnetic Materials*, vol. 306, no. 1, pp. 51–54, 2006.
- [17] Z. Q. Jin, H. Okumura, Y. Zhang, H. L. Wang, J. S. Muoz, and G. C. Hadjipanayis, "Microstructure refinement and significant improvements of magnetic properties in $\text{Pr}_2\text{Fe}_{14}\text{B}/\alpha\text{-Fe}$ nanocomposites," *Journal of Magnetism and Magnetic Materials*, vol. 248, no. 2, pp. 216–222, 2002.
- [18] D. Sultana, M. Marinescu, Y. Zhang, and G. C. Hadjipanayis, "Isotropic nanocomposite Pr-Fe-Co-B ribbons with $(\text{BH})_{\text{max}} > 20$ MGOe," *Physica B*, vol. 384, no. 1-2, pp. 306–309, 2006.
- [19] Z. W. Liu and H. A. Davies, "The practical limits for enhancing magnetic property combinations for bulk nanocrystalline NdFeB alloys through Pr, Co and Dy substitutions," *Journal of Magnetism and Magnetic Materials*, vol. 313, no. 2, pp. 337–341, 2007.
- [20] X.-R. Zeng, H. C. Sheng, J. Z. Zou, and S. H. Xie, "New crystallographic textures of $\text{Nd}_2\text{Fe}_{14}\text{B}/\alpha\text{-Fe}$ nanocomposite materials prepared by controlled melt spinning," *Materials Science Forum*, vol. 654-656, pp. 1170–1173, 2010.
- [21] N. V. Vuong, N. V. Khanh, and D. M. Thuy, "Simulation of the energy product $(\text{BH})_{\text{max}}$ of Nd-Fe-B anisotropic bonded magnets," *Physica B*, vol. 327, no. 2–4, pp. 349–351, 2003.
- [22] N. V. Vuong, C. Rong, Y. Ding, and J. Ping Liu, "Effect of magnetic fields on melt-spun $\text{Nd}_2\text{Fe}_{14}\text{B}$ -based ribbons," *Journal of Applied Physics*, vol. 111, no. 7, pp. 07A731-1–07A731-3, 2012.

Research Article

Synthesis, Characterization, and Microwave-Absorbing Properties of Polypyrrole/MnFe₂O₄ Nanocomposite

Seyed Hossein Hosseini¹ and Ahmad Asadnia²

¹Department of Chemistry, Faculty of Science, Islamic Azad University, Islamshahr Branch, Tehran, Iran

²Young Researchers Club, Islamic Azad University, Central Tehran Branch, Tehran, Iran

Correspondence should be addressed to Seyed Hossein Hosseini, shhosseini@iaiu.ac.ir

Received 24 January 2012; Revised 17 March 2012; Accepted 31 March 2012

Academic Editor: Yi Du

Copyright © 2012 S. H. Hosseini and A. Asadnia. This is an open access article distributed under the Creative Commons Attribution License, which permits unrestricted use, distribution, and reproduction in any medium, provided the original work is properly cited.

Conductive polypyrrole (PPy)-manganese ferrite (MnFe₂O₄) nanocomposites with core-shell structure were synthesized by in situ polymerization in the presence of dodecyl benzene sulfonic acid (DBSA) as the surfactant and dopant and iron chloride (FeCl₃) as the oxidant. The structure and magnetic properties of manganese ferrite nanoparticles were measured by using powder X-ray diffraction (XRD) and vibrating sample magnetometer (VSM), respectively. Its morphology, microstructure, and DC conductivity of the nanocomposite were characterized by scanning electron microscopy (SEM), Fourier transform infrared spectroscopy (FTIR), and four-wire technique, respectively. The microwave-absorbing properties of the nanocomposite powders dispersing in resin acrylic coating with the coating thickness of 1.5 mm were investigated by using vector network analyzers in the frequency range of 8–12 GHz. A minimum reflection loss of –12 dB was observed at 11.3 GHz.

1. Introduction

Recently, conducting polymer composites with both electrical and ferromagnetic properties have received tremendous attention, and study on this kind of composites has become one of the most active and promising research area. What makes conducting polymer composites so attractive is their potential applications in batteries, electrochemical display devices, molecular electronics, electromagnetics shields, microwave-absorbing materials, and so forth. Polypyrrole (PPy) is one of the most promising conducting polymers due to unique properties and excellent environmental stability [1]. Conducting polymers have emerged as a new class of materials in the last three decades. Because of their high conductivity, intriguing electrical properties, and ease of production, potential applications such as microwave absorbers were seriously considered soon after the discovery of these materials [2]. It is well known that conducting polymers can effectively shield electromagnetic waves generated from an electric source, whereas electromagnetic waves from a magnetic source can be effectively shielded only by magnetic materials. Thus, the incorporation of

magnetic constituents and conducting polymeric materials into multifunctional composites opens new possibilities for the achievement of good shielding effectiveness for various electromagnetic sources [3]. The development of microwave-absorbing materials continues to attract much attention. Among the candidates for such application, ferrites present an interesting material. The use of ferrite-based absorbers requires better performance at higher frequencies such as X-band [4].

Spinel-type ferrites have been used as conventional microwave absorption materials. However, spinel-type ferrites show Snoek's limit, and the magnetic loss decreases drastically at several gigahertz [5]. Electromagnetic wave absorbing materials used in gigahertz (GHz) range have attracted much attention with the development of GHz microwave communication, radar detection, and other industrial applications in recent years. These absorbing materials can be manufactured by a number of magnetic and dielectric materials in powder form, loaded in various kinds of polymeric binders. Various electromagnetic wave absorbing materials can be designed by using the dispersion characteristic of the complex permittivity and permeability.

Ferrite is one of materials as electromagnetic-wave-absorber, and a number of investigations have been reported for studying the effect of composition on electromagnetic wave absorption properties [6]. In the past decades, the spinel ferrites have been utilized as the most frequent absorbing materials in various forms. Manganese ferrite (MnFe_2O_4) is a common spinel ferrite material and has been widely used in microwave and magnetic recording applications. Recently, it has been shown that magnetic nanocomposites are useful as microwave-absorbing materials due to their advantages in respect to light weight, low cost, design flexibility, and microwave properties over pure ferrites [7]. The previous work, PANi-manganese ferrite nanocomposite with the magnetic behavior, is successfully synthesized by in situ polymerization of aniline in the presence of MnFe_2O_4 nanoparticles [8]. A minimum reflection loss of -15.3 dB was observed at 10.4 GHz. In this work, minimum reflection loss of -12 dB was observed at 11.3 GHz.

2. Experimental

2.1. Materials and Instrumentals. Chemicals including metal salts, hexamethylenetetramine (HMTA), potassium persulfate (KPS), and ethylene glycol (EG) are analytical grade (Merck) and were used without further purification. Water was deionized, doubly distilled, and deoxygenated prior to use. Styrene and methacrylic acid (analytical grade, Merck) were distilled to remove the inhibitor. Pyrrole monomer (analytical grade, Merck) was distilled twice under reduced pressure. DBSA and acrylic resin were of industrial grade. The other reagent, including iron chloride (FeCl_3), was of analytical grade (Merck).

The morphology of coated particles and nanocomposite was observed by scanning electron microscopy (SEM) with a JSM-6301F (Japan) instrument operated at an accelerating voltage of 10 kV. X-ray powder diffraction (XRD) patterns of the nanoparticles assemblies were collected on a Philips-PW 1800 with Cu-K radiation under $\text{CuK}\alpha$ radiation ($\lambda = 1.5406 \text{ \AA}$). Fourier transform infrared spectroscopy (FTIR) spectra were recorded on a PerkinElmer spectrum FTIR using KBr pellets. The M-H hysteresis loops were measured by vibrating sample magnetometer (VSM) (RIKEN DENSHI Co. Ltd., Japan). Microwave-absorbing properties were measured by vector network analyzers (Agilent Technologies Inc. 8722) in the 8–12 GHz range at room temperature.

2.2. Preparation of Nanoparticles (see [9])

2.2.1. PS Colloid. Negatively charged PS spheres with average diameter 230 nm, which were used as core particles, were prepared by a free-emulsion polymerization method [10]. In a typical experiment, 10 mL styrene, 2 mL methacrylic acid, and 0.054 g KPS were added to the flask with 100 mL deionized water. To eliminate oxygen effects, the solution was purged with nitrogen before the process was initiated. The mixture was heated to 72°C and stirred with a magnetic stirrer. The polymerization was continued for 24 h, and in the whole procedure the nitrogen was purged. Concentration

of PS spheres in solution is 80 mg/mL, which was calculated by drying 5 mL colloid solution and weighing the remained solids.

2.3. Coated Particles. The coating procedure consisted of controlled hydrolysis of aqueous solutions of ferrous chloride and other divalent metal salts in the presence of polystyrene latexes. In a typical preparation process, 2 mL PS colloid solution was diluted with 250 mL deoxygenated distilled water and then mixed with the metal salts solution, which contained 10 mmol FeCl_2 and 5 mmol MnCl_2 . After dispersed under ultrasonic for several minutes, the mixture was incorporated with 4 g HMTA and 0.5 g potassium nitrate and heated to 85°C under gentle stirring. After 3 h, the system was cooled to room temperature. The solution was poured into excess distilled water, then magnetic particles were deposited using magnetic field. The precipitate was washed with distilled water for several times and then dried in oven at 80°C for 24 h. In addition, to modify the surface chemical properties of the composites magnetic spheres, 5 mL ethylene glycol (EG) was added into the reaction solution before the incorporation of HMTA.

2.4. Synthesis of MnFe_2O_4 -PPy Nanocomposite with Core-Shell Structure. MnFe_2O_4 -PPy core-shell nanocomposites were prepared by in situ polymerization in the presence of DBSA as the surfactant and dopant and FeCl_3 as the oxidant. The DBSA was dissolved in distilled water with vigorous stirring for about 20 min, then MnFe_2O_4 nanoparticles (0.73 g) were added to the DBSA solution under stirring for approximately 1 h. Then 5 mL of pyrrole monomer was added to the suspension and stirred for 30 min. MnFe_2O_4 nanoparticles were dispersed well in the mixture of pyrrole/DBSA under ultrasonication for 2 h. 23.5 g FeCl_3 in 60 mL deionized water was slowly added dropwise to the mixture with a constant stirring. The polymerization with stirring under an ice-water bath was allowed to proceed for 4 h. The nanocomposite was obtained by filtering and washing the suspension with deionized water and ethanol, respectively. The obtained black powder with the content of 15 wt% MnFe_2O_4 was dried under vacuum for 24 h.

3. Results and Discussion

3.1. X-Ray Diffraction. Figure 1 shows the XRD pattern of manganese ferrites. It can be clearly noted from Figure 1 that the ferrite shell are phase-pure spinel structure in all cases according to the standard XRD patterns of the spinel ferrite Fe_3O_4 ($2\theta = 30.1, 35.5, 43.7, 53.2, 57.0, 62.4, 74.0, 78.0$) Mn ferrite ($2\theta = 33.0, 71.0, 86.5$), and NaCl ($2\theta = 75.4$). The average crystallite size was calculated using software Originpro75 through the diffraction speaks from Scherrer's formula as shown below:

$$D = 0.89 \frac{\lambda}{\beta} \cos \theta, \quad (1)$$

where D is the crystal size, λ is the X-ray wavelength, β is the broadening of the diffraction peak, and θ is the diffraction

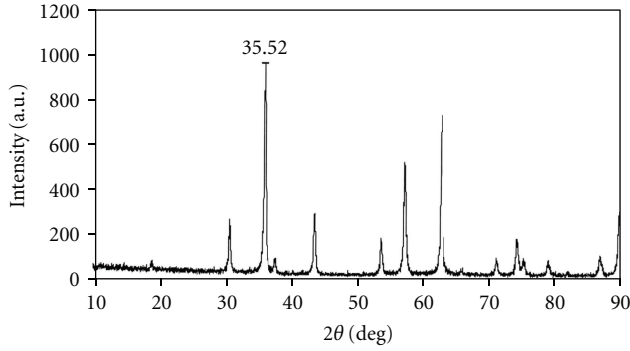


FIGURE 1: X-ray diffraction for MnFe_2O_4 .

angle. Calculated by the Scherrer formulation, the mean crystallite size of the ferrite particles is 24.27 nm.

3.2. Magnetic Properties. Figures 2(a) and 2(b) show the magnetization (M) versus the applied magnetic field (H) for MnFe_2O_4 and $\text{MnFe}_2\text{O}_4/\text{PPy}$ nanocomposite (15 wt%) respectively. The magnetic properties of the ferrite-coated PS latex were analyzed by room temperature VSM with an applied field $-10 \text{ kOe} \leq H \leq 10 \text{ kOe}$. It can be inferred from the hysteresis loops that all the composite magnetic spheres are magnetically soft at room temperature. The value of saturation magnetization (M_s) is about 66.7 emu/g, the remnant magnetization (M_r), and coercivity field are 17.81 emu/g and 110 Oe, respectively. Figure 2(b) shows clear saturation $-10 \leq H \leq 10 \text{ kOe}$ with saturation magnetization (M_s) about 10 emu/g and the remnant magnetization (M_r) about 3.4 emu/g, for nanocomposite which is lower than pure manganese ferrite nanoparticles, so the magnetization curve of the sample shows weak ferromagnetic behavior, with slender hysteresis. Magnetic properties of nanocomposites containing magnetite or ferrite particles have been believed to be highly dependent on the sample shape, crystallinity, and the value of magnetic particles, so that they can be adjusted to obtain optimum property. Magnetic properties of nanocomposite and ferrite particles showed soft magnetization behavior.

3.3. Morphology Investigation. Figures 3(a), 3(b), and 3(c) show the SEM images for the MnFe_2O_4 and $\text{MnFe}_2\text{O}_4/\text{PPy}$ nanocomposite, respectively. As shown in Figure 3(a), the spongy-shaped MnFe_2O_4 was seen with a small quantity of amorphous phase. The length of spongy-shaped MnFe_2O_4 average diameter is about 80–90 nm. In Figures 3(b) and 3(c), it is found that the $\text{MnFe}_2\text{O}_4/\text{PPy}$ nanocomposite (15 wt%) still retains the morphology of PPy shape. It is much unknown how to form spongy-shaped composite in the polymerization process. The SEM image clearly shows that the MnFe_2O_4 was distributed rather homogeneously and ultrasonication is effective for dispersing nanoferrite in the polymer matrix.

The length of $\text{MnFe}_2\text{O}_4/\text{PPy}$ nanocomposite average diameter is about 60–130 nm.

3.4. FTIR Spectra. Figures 4(a) and 4(b) show FTIR spectra of MnFe_2O_4 and $\text{PPy-MnFe}_2\text{O}_4$ nanocomposite, respectively. In ferrites, the metal ions are usually situated in two different sublattices, designated as tetrahedral and octahedral sites according to the geometrical configuration of the oxygen nearest neighbors [9]. It was observed from Figure 4(a) that the peak at 570.22 cm^{-1} is intrinsic vibrations of manganese ferrite. The characteristic peaks of styrene occur at 1638, 1458.04, 1008.65–1382.16, 811.30 and 865.50 cm^{-1} . The peak at 1638 is attributed to the styrene ring. The peak at 1458 cm^{-1} is attributed to the characteristic C=C stretching ring. The peaks at 811.30, and 865.50 cm^{-1} are related to the C–H outer bending vibrations.

As shown in Figure 4(b), the characteristic peaks of PPy-manganese ferrite nanocomposite occur at 2920, 1555, 1461, 1313, 1188, 1038, 1006, 959, 908, 670, and 576 cm^{-1} . The peaks at 1555 and 1461 cm^{-1} are attributed to the characteristic C=C and C–N stretching of polypyrrole ring; the peaks at 1313 and 1188 cm^{-1} correspond to N–H bending and asymmetric C–N stretching modes of the PPy ring, respectively. The peak around 1038 cm^{-1} is associated with vibrational modes of N=Q=N (Q refers to the quinonic type rings), indicating that PPy is formed in our sample. The peaks at 2920 and 1038 cm^{-1} attributed to C–H aliphatic stretching vibration and the symmetric and antisymmetric stretching vibration of SO_3 group of dopant (DBSA), respectively. The peaks at $1006\text{--}908 \text{ cm}^{-1}$ are attributed to the *p*-disubstituted aromatic ring C–H out-of-plane bending. However, the characteristic peaks of MnFe_2O_4 for F–O and Mn–O stretching vibrations can be observed at wave numbers 670 and 576 cm^{-1} .

3.5. Microwave-Absorbing Properties. According to transmission line theory, the reflection loss (RL) of electromagnetic radiation, under normal wave incidence at the surface of a single-layer material backed by a perfect conductor can be given by

$$\text{RL} = 20 \log \left| \frac{Z_{in} - Z_0}{Z_{in} + Z_0} \right|, \quad (2)$$

where Z_0 is the characteristic impedance of free space:

$$Z_0 = \sqrt{\frac{\mu_0}{\epsilon_0}}. \quad (3)$$

Z_{in} is the input impedance at free space and materials interface:

$$Z_{in} = \sqrt{\frac{\mu_r}{\epsilon_r} \tanh \left[j \frac{2\pi f t}{c} \sqrt{\mu_r \epsilon_r} \right]}, \quad (4)$$

where μ_r and ϵ_r are the complex permeability and permittivity of the composite medium, respectively, which can be calculated from the complex scatter parameters, c is the light velocity, f is the frequency of the incidence electromagnetic wave, and t is the thickness of composites. The impedance-matching condition is given by $Z_{in} = Z_0$ to represent the perfect absorbing properties [9]. There are two

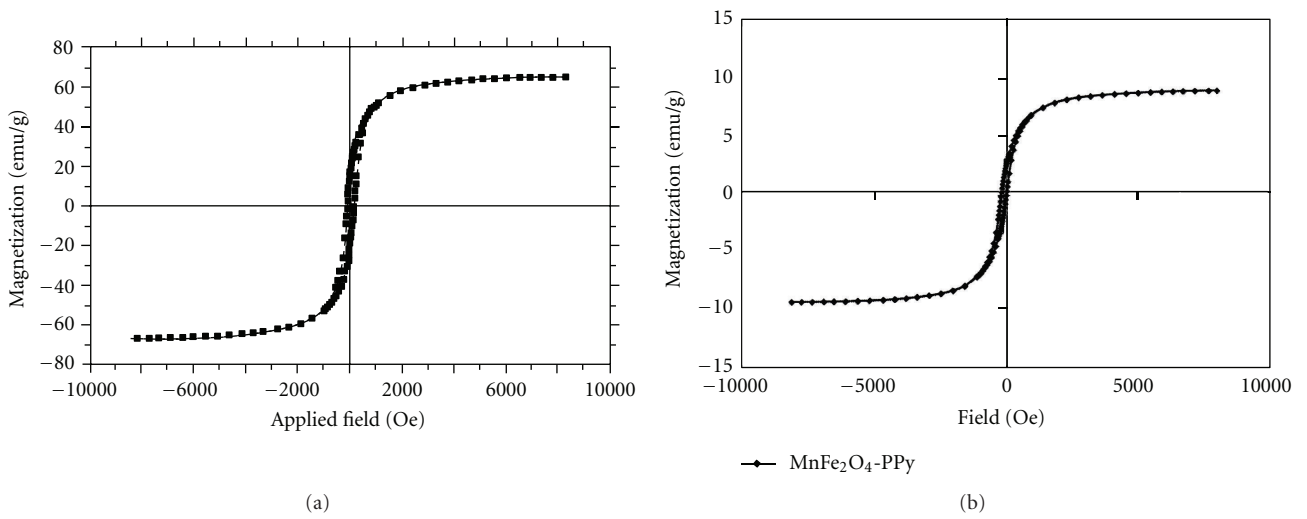


FIGURE 2: Magnetic hysteresis loop of (a) MnFe₂O₄ nanoparticle and (b) MnFe₂O₄/PPy nanocomposite.

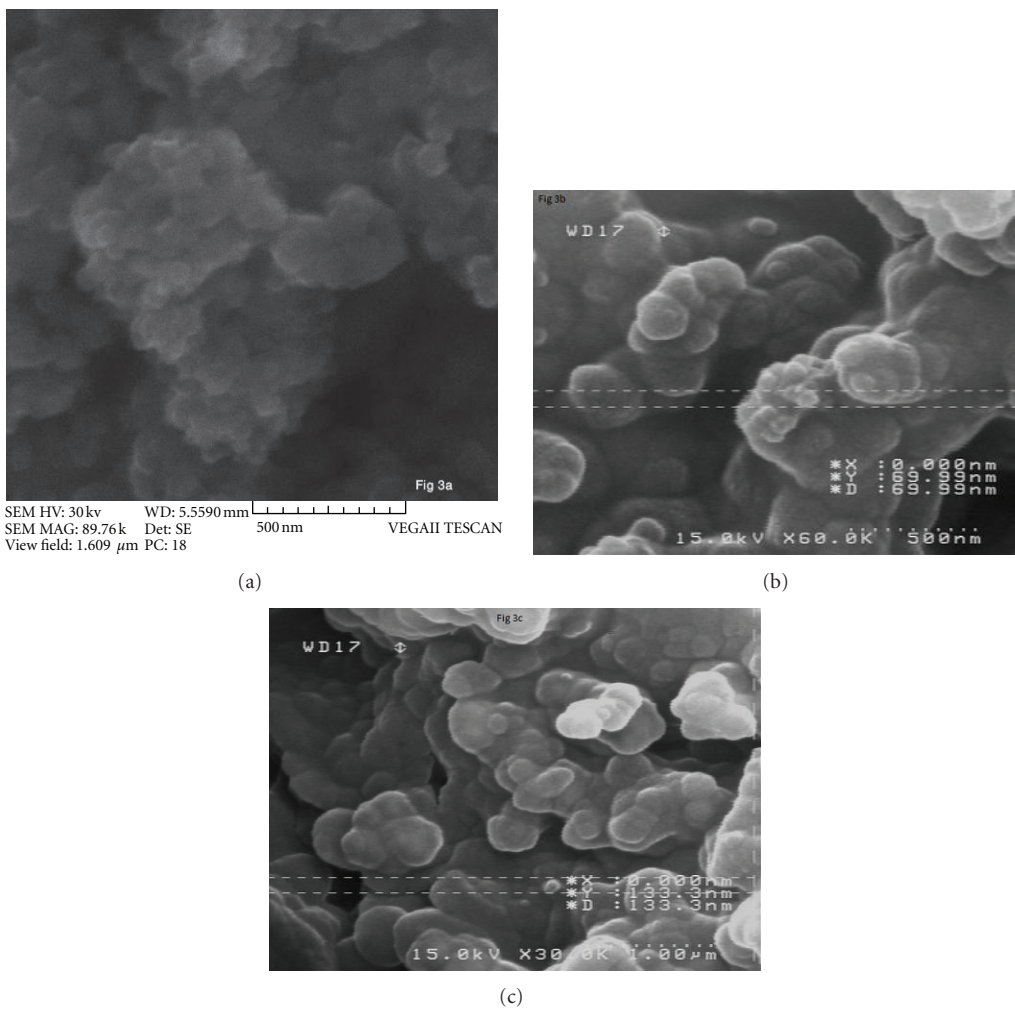


FIGURE 3: SEM microphotographs of (a) MnFe₂O₄ nanoparticle and ((b), (c)) MnFe₂O₄/PPy nanocomposite.

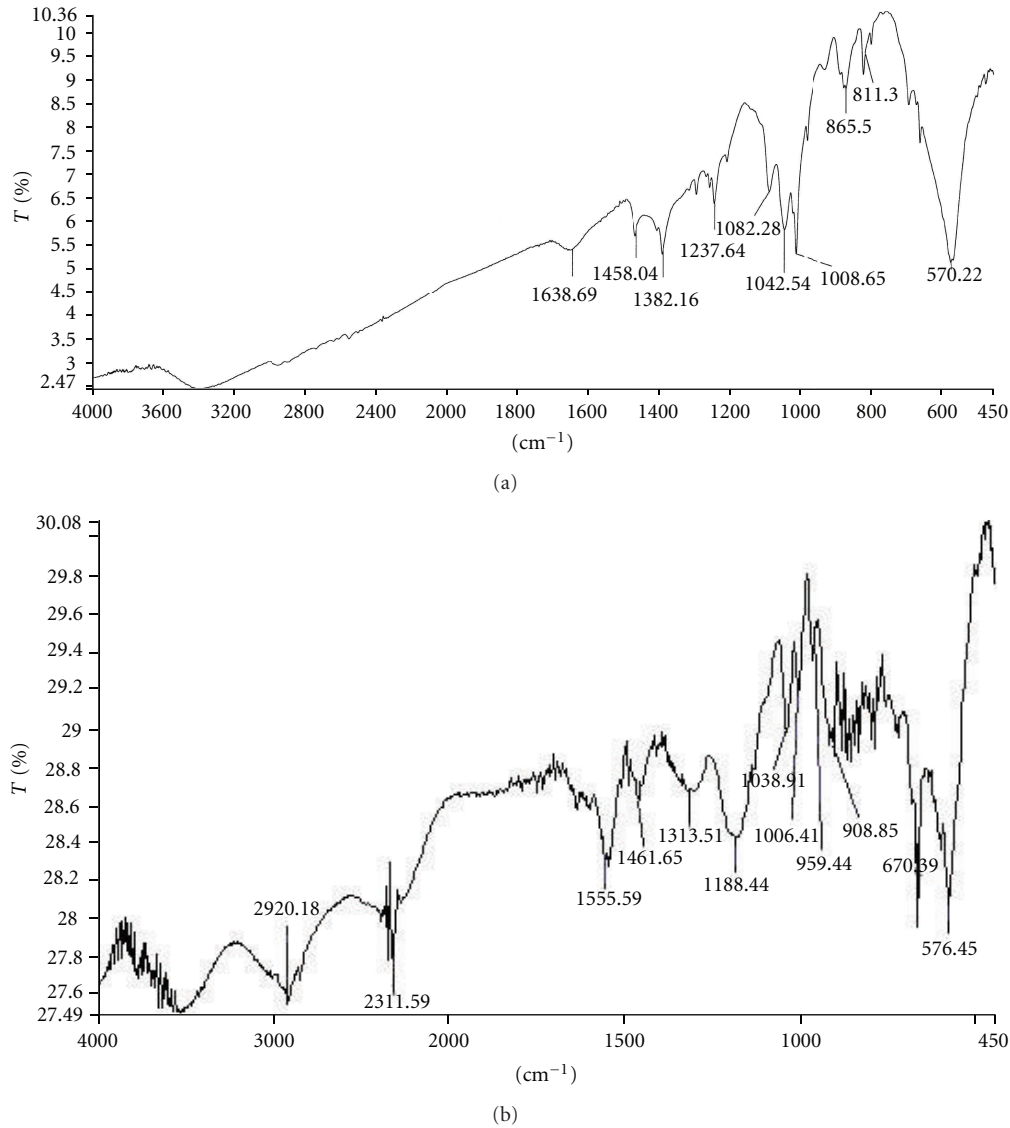


FIGURE 4: FTIR spectra: (a) MnFe_2O_4 nanoparticle and (b) $\text{MnFe}_2\text{O}_4/\text{PPy}$ nanocomposite.

different concepts to satisfy the zero-reflection condition. The first concept is the “matched characteristic impedance.” The intrinsic impedance characteristic of material is made equal to the impedance characteristic of the free space. The second is the “matched-wave-impedance” concept. The wave impedance at the surface of the metal-backed material layer is made equal to the intrinsic impedance of the free space. In this work, the second concept was applied. The condition of maximal absorption is satisfied at a particular point where thickness and frequency match each other. Ferrites are the only materials that present two matching frequencies and thicknesses. The first matching at low frequency is associated with the mechanisms of magnetic resonance and shows a dependence on the chemical composition. The second matching at high frequency is associated with the thickness of absorber material. To satisfy the zero-reflection condition where maximum absorption would occur, Z_{in} should be 1

to prevent reflection. This can be ideally achieved when the material presents $|\mu_r| = |\epsilon_r|$. In this case, the performance of electromagnetic wave-absorbing material increases linearly with the increase in thickness. In practical terms, however, this is rarely achieved because the values of complex permeability and complex permittivity are very different in the frequency range of interest. When $|\mu_r| \neq |\epsilon_r|$, we should consider two other cases. For materials with intrinsic impedances greater than unity, $|\mu_r| > |\epsilon_r|$, the minimum reflection loss occurs at around a half-wavelength thickness of the material, and for materials with intrinsic impedances lower than unity, $|\mu_r| < |\epsilon_r|$, the minimum reflection loss occurs at around a quarter-wavelength thickness of the material. Within the microwave region, ferrites usually present electromagnetic characteristics of $|\mu_r| < |\epsilon_r|$, giving rise to the term “quarter-wavelength absorbers.” Minimum loss occurs when the thickness is about an odd multiple

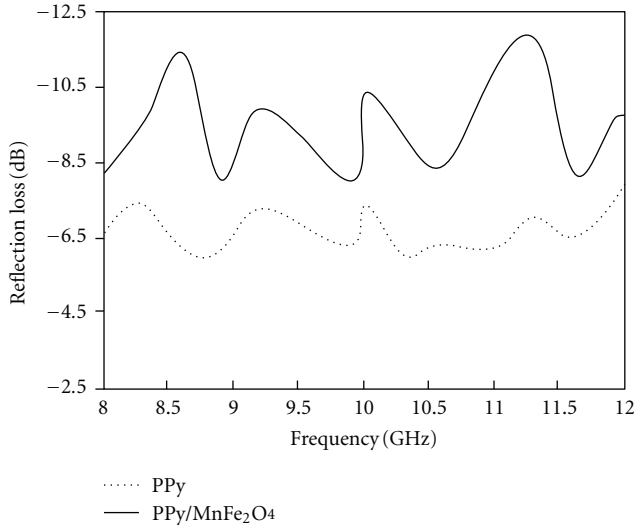


FIGURE 5: Frequency dependence of RL for the $\text{MnFe}_2\text{O}_4/\text{PPy}$ nanocomposite.

of one quarter of the wavelength of the incident frequency, measured inside the absorbing material, and the material has the proper loss factor for this particular thickness. The thickness, d , can be written as (5), where c is the speed of light and f is the frequency of interest [11]:

$$d = \frac{c}{4f\sqrt{|\mu_r||\epsilon_r|}}. \quad (5)$$

Nanocomposite powders dispersed in acrylic resins, then the mixture was pasted on metal plate with the area of $100\text{ mm} \times 100\text{ mm}$ as the test plate. The microwave-absorbing properties of the nanocomposite with the coating thickness of 1.5 mm, were investigated by using vector network analyzers in the frequency range of 8–12 GHz. Figure 5 shows the variation of reflection loss versus frequency determined from PPy-manganese ferrite nanocomposite. For MnFe_2O_4 composites with the coating thickness of 1.5 mm, the reflection loss values less than -12 dB were obtained in the frequency of 8–12 GHz and its value of minimum reflection loss is -12 dB at the frequency of 11.3 GHz.

4. Conclusion

The obtained magnetic nanoparticles are of a diameter of 24.27 nm. PPy-manganese ferrite nanocomposite with the magnetic behavior is successfully synthesized by in situ polymerization of pyrrole in the presence of MnFe_2O_4 nanoparticles. The results of spectroanalysis indicate that there is an interaction between PPy chains and ferrite particles. A minimum reflection loss of -12 dB was observed at 11.3 GHz with at thickness of 1.5 mm of nanocomposite.

References

- [1] C. Zhang, Q. Li, and Y. Ye, "Preparation and characterization of polypyrrole/nano- $\text{SrFe}_{12}\text{O}_{19}$ composites by in situ polymerization method," *Synthetic Metals*, vol. 159, no. 11, pp. 1008–1013, 2009.
- [2] V. T. Truong, S. Z. Riddell, and R. F. Muscat, "Polypyrrole based microwave absorbers," *Journal of Materials Science*, vol. 33, no. 20, pp. 4971–4976, 1998.
- [3] B. Birsöz, A. Baykal, H. Sözeri, and M. S. Toprak, "Synthesis and characterization of polypyrrole- $\text{BaFe}_{12}\text{O}_{19}$ nanocomposite," *Journal of Alloys and Compounds*, vol. 493, no. 1-2, pp. 481–485, 2010.
- [4] T. Giannakopoulou, L. Kompotiatis, A. Kontogeorgakos, and G. Kordas, "Microwave behavior of ferrites prepared via sol-gel method," *Journal of Magnetism and Magnetic Materials*, vol. 246, no. 3, pp. 360–365, 2002.
- [5] S. Sugimoto, K. Haga, T. Kagotani, and K. Inomata, "Microwave absorption properties of Ba M-type ferrite prepared by a modified coprecipitation method," *Journal of Magnetism and Magnetic Materials*, vol. 290-291, pp. 1188–1191, 2005.
- [6] F. Tabatabaie, M. H. Fathi, A. Saatchi, and A. Ghasemi, "Microwave absorption properties of Mn- and Ti-doped strontium hexaferrite," *Journal of Alloys and Compounds*, vol. 470, no. 1-2, pp. 332–335, 2009.
- [7] H. M. Xiao, X. M. Liu, and S. Y. Fu, "Synthesis, magnetic and microwave absorbing properties of core-shell structured $\text{MnFe}_2\text{O}_4/\text{TiO}_2$ nanocomposites," *Composites Science and Technology*, vol. 66, no. 13, pp. 2003–2008, 2006.
- [8] S. H. Hosseini, S. H. Mohseni, A. Asadnia, and H. Kerdari, "Synthesis and microwave absorbing properties of polyaniline/ MnFe_2O_4 nanocomposite," *Journal of Alloys and Compounds*, vol. 509, no. 14, pp. 4682–4687, 2011.
- [9] Y. Zhang, Z. Huang, F. Tang, and J. Ren, "Ferrite hollow spheres with tunable magnetic properties," *Thin Solid Films*, vol. 515, no. 4, pp. 2555–2561, 2006.
- [10] G. Mu, N. Chen, X. Pan, H. Shen, and M. Gu, "Preparation and microwave absorption properties of barium ferrite nanorods," *Materials Letters*, vol. 62, no. 6-7, pp. 840–842, 2008.
- [11] A. R. Bueno, M. L. Gregori, and M. C. S. Nóbrega, "Microwave-absorbing properties of $\text{Ni}_{0.50-x}\text{Zn}_{0.50-x}\text{Me}_{2x}\text{Fe}_2\text{O}_4$ (Me 1/4 Cu, Mn, Mg) ferrite wax composite in X-band frequencies," *Journal of Magnetism and Magnetic Materials*, vol. 320, no. 6, pp. 864–870, 2008.

Research Article

Temperature-Driven Spin Reorientation Transition in CoPt/AlN Multilayer Films

Wupeng Cai,¹ Shinji Muraishi,² Ji Shi,² Yoshio Nakamura,² Wei Liu,¹ and Ronghai Yu³

¹Department of Materials Science and Engineering, Tsinghua University, Beijing 100084, China

²Department of Metallurgy and Ceramics Science, Tokyo Institute of Technology, 2-12-1, Oh-okayama, Meguro-ku, Tokyo 152-8552, Japan

³School of Materials Science and Engineering, Beihang University, Beijing 100191, China

Correspondence should be addressed to Ji Shi, shi.j.aa@m.titech.ac.jp

Received 10 May 2012; Accepted 23 May 2012

Academic Editor: Weichang Hao

Copyright © 2012 Wupeng Cai et al. This is an open access article distributed under the Creative Commons Attribution License, which permits unrestricted use, distribution, and reproduction in any medium, provided the original work is properly cited.

Spin reorientation transition phenomena from out-of-plane to in-plane direction with increasing temperature are observed for the 500°C annealed CoPt/AlN multilayer films with different CoPt layer thicknesses. CoPt-AlN interface and volume anisotropy contributions, favoring out-of-plane and in-plane magnetization, respectively, are separately determined at various temperatures. Interface anisotropy exhibits much stronger temperature dependence than volume contribution, hence the temperature-driven spin reorientation transition occurs. Interface anisotropy in this work consists of Néel interface anisotropy and magnetoelastic effect. Magnetoelastic effect degrades rapidly and changes its sign from positive to negative above 200°C, because of the involvement of stress state in CoPt films with temperature. By contrast, Néel interface anisotropy decays slowly, estimated from a Néel mean field model. Thus, the strong temperature dependence of CoPt-AlN interface anisotropy is dominated by the change of magnetoelastic effect.

1. Introduction

Spin reorientation transition (SRT) is one of the most interesting phenomena occurring in thin ferromagnetic films. During this process, the orientation of the magnetization changes spontaneously and often reversibly from one direction to another. This process can be induced by varying related parameters such as measuring temperature and film thickness. Tremendous efforts have been made to investigate SRT in various systems such as Fe/Ag(100) [1–4], Fe/Cu(100) [1, 3, 5–7], Gd/W(110) [8–10], and Co/Au(111) [11–14]. Generally, with increasing temperature and film thickness, SRT from perpendicular to the in-plane magnetic direction has been observed. However, Ni/Cu(001) thin films exhibit the reversed SRT, namely, from in-plane to perpendicular orientation [15–17]. That is due to the different signs of the surface anisotropy between Ni and Fe, Co, Gd, which favors in-plane magnetization for Ni and out-of-plane magnetization for Fe, Co, Gd.

SRT phenomena are generally caused by the competition between several anisotropy contributions favoring different directions of magnetization. For example, different temperature dependences of these anisotropy contributions may make a temperature-driven SRT occur. For a thin ferromagnetic film, the surface or interface anisotropy (K_S) becomes comparable with the other effects like shape and magnetocrystalline anisotropies. Hence, it is important to study the temperature dependence of K_S to understand the SRT process. Farle et al. found an almost linear decrease of K_S with increasing temperature for Gd/W(110), Ni/W(110), and Ni/Cu(001) thin films [10, 18–20]. Similar linear temperature dependence of K_S has been observed for Ni/Re(0001) [21] and Fe/Cu(001) [7]. On the other hand, Pechan found a much more abrupt decrease of K_S for Ni/Mo multilayers, which is inexplicable in terms of a simple Néel mean field model [22]. The author then supposed such strong temperature dependence of K_S was due to the involvement of Ni-Mo interface strain, which generates a magnetoelastic

term in K_S . But quantitative study of the magnetoelastic effect has not been conducted.

For the metal/metal films, the interlayer mixing or interfacial reaction at elevated temperatures will destroy the interface and make an irreversible change to the magnetic properties. In our previous work, to avoid such structural changes, AlN instead of metal was used to form CoPt/AlN multilayer films [23–25]. Flat and continuous CoPt-AlN interface has been observed even after high-temperature postdeposition annealing at temperatures as high as 500°C [23, 24]. CoPt layers remain FCC structure when the annealing temperature is below 600°C [25]. High crystallinity, strong (111) texture in CoPt layers and (002) texture in AlN layers were exhibited. Moreover, a large perpendicular magnetic anisotropy was obtained mainly due to the tensile stress in the CoPt layers [23]. In the present work, we have investigated the temperature dependence of CoPt-AlN interface anisotropy up to 350°C and its relationship with the temperature-driven SRT in CoPt/AlN multilayer films. The temperature dependence of the stress-induced magnetoelastic term in interface anisotropy has also been quantitatively studied.

2. Experiment

CoPt/AlN multilayer films with the configuration as [AlN (10 nm)/CoPt (x nm)]₅/AlN (10 nm) ($x = 2, 4, 6, 8$) were prepared at ambient temperature by direct current (dc) magnetron sputtering on fused-quartz substrates. Two pairs of facing targets, one pair composed of Co and Pt targets and the other pair composed of two Al targets, were equipped at two sides in the sputtering chamber. Sample depositions were conducted in an Ar and N₂ gas mixture. CoPt/AlN multilayer films were formed by switching the substrate holder alternatively to the two targets sides. The atomic ratio in the CoPt layer is Co₄₄Pt₅₆. As-deposited films were then annealed in a vacuum furnace (below 1×10^{-4} Pa) at 500°C for 3 hours.

Out-of-plane (along the film normal, \perp) and in-plane (in the film plane, \parallel) magnetization-temperature (M - T) curves were measured by a vibrating sample magnetometer (VSM) with heating rate as 5°C/min. Before the measurement of M - T curves, the sample was magnetized in an external field of 1 T, and then the external field was removed. However, a small constant external field about 60 Oe, which is the residual magnetization of the cores inside the electromagnets, still exists. In-plane and out-of-plane hysteresis loops at various temperatures up to 350°C were measured with the same VSM.

3. Results and Discussion

Figure 1 shows the evolutions of in-plane and out-of-plane remnant magnetizations with temperature for CoPt/AlN multilayer films with different CoPt layer thicknesses. SRT from out-of-plane to in-plane direction, indicated by an abrupt decrease of out-of-plane magnetization (M_{\perp}) followed by rapid increase of in-plane magnetization (M_{\parallel}), can be observed for the films with CoPt layer thickness larger than 2 nm. Moreover, SRT occurs at lower temperatures

when the CoPt layer thickness increases. For the film with CoPt layer thickness $d = 2$ nm, M_{\perp} starts decreasing rapidly at a relative high temperature of 303°C, while M_{\parallel} remains a low value (about one tenth of M_{\perp}) in the whole temperature range without obvious increase. When $d = 4$ nm, M_{\perp} exhibits an abrupt degradation from a much lower temperature of 110°C. On the other hand, M_{\parallel} starts a sharp increase around 250°C and reaches a considerable magnitude. For the thicker films with d as 6 and 8 nm, it seems that the rapid depression of M_{\perp} occurs from a temperature below room temperature. The starting temperature of the rapid increase of M_{\parallel} is about 100°C when $d = 6$ nm, while it should be lower than the room temperature when $d = 8$ nm. The final decay of M_{\parallel} in the in-plane M - T curve is due to the ferromagnetic-paramagnetic transition.

As mentioned in Section 1, the temperature-driven SRT is generally caused by the change of magnetic anisotropy with temperature. Hence, we measured the in-plane and out-of-plane hysteresis loops for each film at various temperatures up to 350°C in order to measure the effective anisotropy energy. Typical results for the CoPt/AlN multilayer film with $d = 4$ nm are shown in Figures 2(a)–2(c), which show a smooth transition from perpendicular to in-plane magnetic anisotropy. At 250°C, the film almost exhibits a magnetic isotropic behavior (Figure 2(b)). Figure 2(d) shows the change of saturation magnetization (M_S), obtained from the hysteresis loops, with temperature. The degradation of M_S exhibits a growing rate with increasing temperature.

The total magnetic anisotropy energy per volume K_{eff} (erg/cm³) is calculated by measuring the area enclosed between in-plane and out-of-plane hysteresis loops. When the magnetic anisotropy is extremely high, the saturation of magnetization along the hard axis cannot be reached under the maximum applied field of 1 T. In such cases, the hard axis hysteresis loop is extrapolated to M_S . Figure 3 summarizes the calculated K_{eff} of CoPt/AlN multilayer films with $d = 2, 4, 6$ and 8 nm at different temperatures. At room temperature, a high perpendicular magnetic anisotropy (PMA) energy of 7.2×10^6 erg/cm³ is obtained when $d = 2$ nm. With increasing d , PMA weakens and turns to a weak in-plane magnetic anisotropy (IMA) when $d = 8$ nm. With increasing temperature, PMA rapidly degrades. Due to the strong PMA of 2 nm thick CoPt thin film, out-of-plane easy axis is maintained up to 350°C. On the other hand, when $d = 4$ and 6 nm, the transition from PMA to IMA occurred at 250°C and 100°C, respectively. When $d = 8$ nm, only IMA is observed. Maximum K_{eff} with a value of -8.2×10^5 erg/cm³ has been obtained at 300°C. The degradation of IMA at high temperatures may arise from the enhancing thermal fluctuations. Magnetic anisotropy could be expected to vanish at the Curie temperature.

Magnetic anisotropy decides the magnetization state at each temperature, illustrated in Figure 1(b). When K_{eff} is extremely high, for example, $d = 2$ nm below 303°C and $d = 4$ nm below 110°C, a single perpendicular domain can be maintained. Hence, M_{\perp} only gradually decreases with increasing temperature. When K_{eff} decreases to a critical value, for example, $d = 2$ nm at 303°C and $d = 4$ nm at 110°C, the reversed magnetization starts to form.

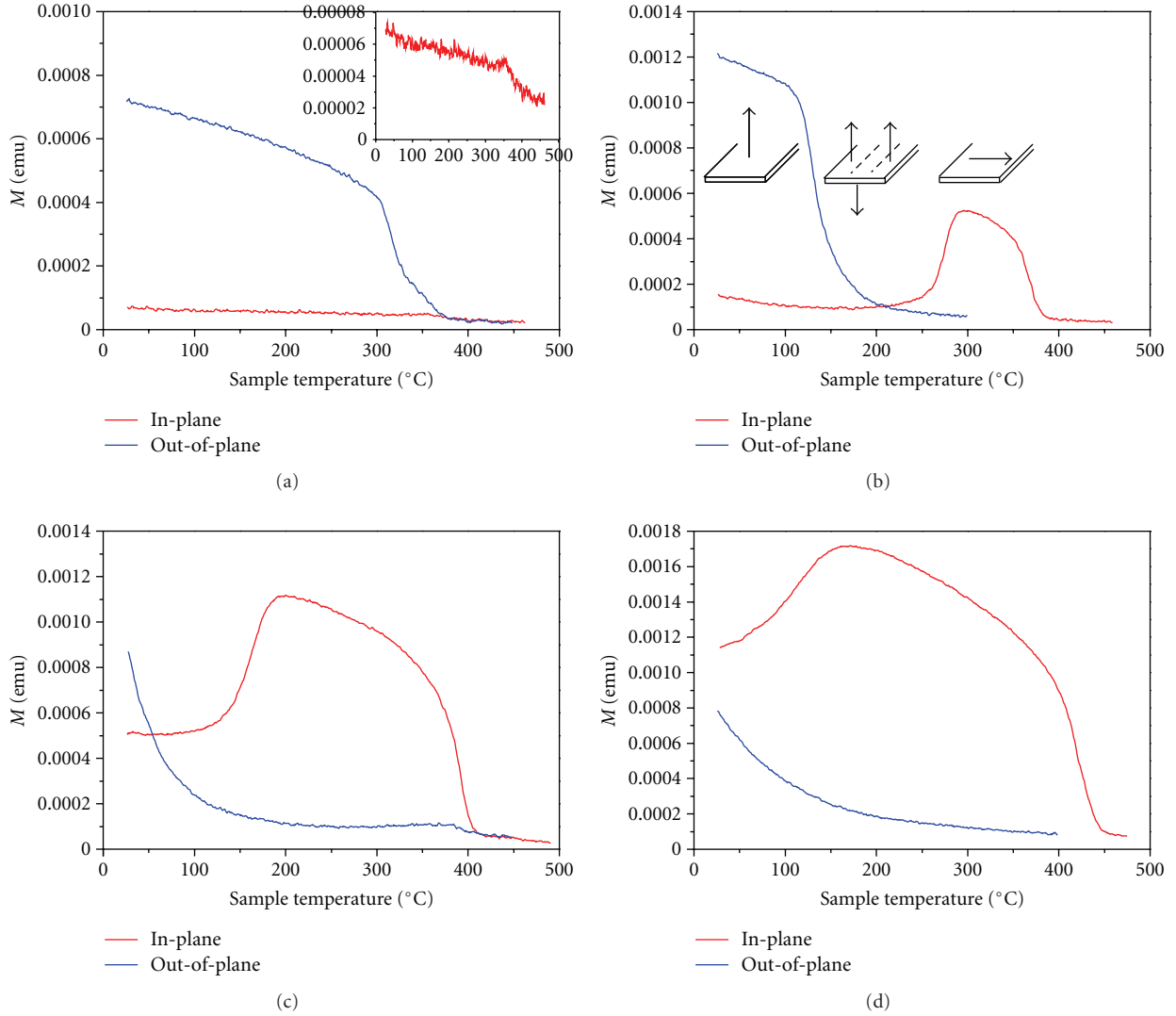


FIGURE 1: In-plane and out-of-plane Magnetization-Temperature (M - T) curves of CoPt/AlN multilayer films with the CoPt layer thickness of 2, 4, 6 and 8 nm for (a), (b), (c), and (d), respectively. The inset image in (a) is the in-plane M - T curve in a small magnetization range. In (b) the corresponding magnetization states are illustrated.

Consequently, the single domain state is destroyed and M_{\perp} rapidly decreases. When thin films become magnetic isotropy ($K_{\text{eff}} = 0$), for example, $d = 4$ nm at 250°C and $d = 6$ nm at 100°C , perpendicular domains become unstable and in-plane domains starts to form. Thus, M_{\parallel} starts a sharp increase. The experimental observation of the evolution of magnetic domain with temperature can be seen in [6]. But a detailed experimental study on the correlation between the change of magnetic anisotropy and the change of remanent magnetization was rarely reported previously. Our work reveals that at the starting temperature of the rapid decrease of M_{\perp} , thin films still possess considerable PMA; at the starting temperature of the rapid increase of M_{\parallel} , thin films exhibit magnetic isotropy.

For a ferromagnetic thin film, K_{eff} (erg/cm^3) can be phenomenologically written as $K_{\text{eff}} = (2K_S/d) + K_V$, where K_S (erg/cm^2) is the interface anisotropy energy density, d is the film thickness, and K_V (erg/cm^3) is the volume contribution,

which is the sum of the magnetocrystalline, magnetoelastic, and shape anisotropies. The factor of 2 in $2K_S/d$ takes into account the two interfaces. $K_{\text{eff}} > 0$ corresponds to perpendicular anisotropy and $K_{\text{eff}} < 0$ in-plane anisotropy. To understand the observed SRT phenomena, temperature dependences of K_S and K_V need to be revealed. The individual values of K_S and K_V can be determined by the linear relationship between $K_{\text{eff}}d$ and d as $K_{\text{eff}}d = 2K_S + K_Vd$, where $2K_S$ is the intercept at $d = 0$ and K_V is the slope. Good linear d dependence of $K_{\text{eff}}d$ is experimentally obtained at each measuring temperature, shown in Figure 4. Hence, the interface and volume anisotropy contributions are separately determined. Note K_S is positive and K_V is negative, indicating the interface and volume anisotropies favor out-of-plane and in-plane magnetization, respectively. The temperature dependences of K_S and K_V are then shown in Figure 5. It can be seen clearly that K_S decreases more rapidly than K_V . Consequently, K_V will become predominant and the

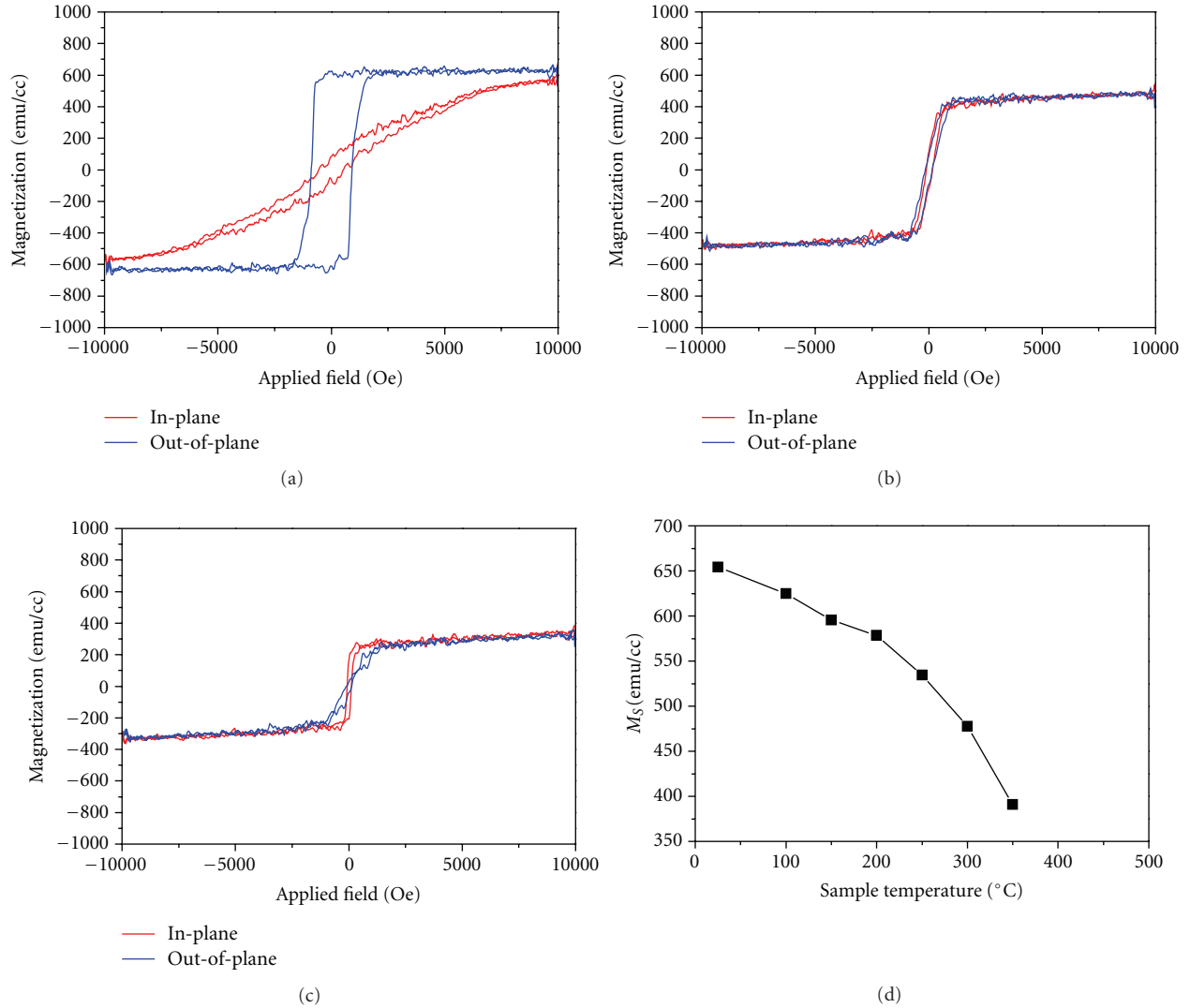


FIGURE 2: In-plane and out-of-plane hysteresis loops of a CoPt/AlN multilayer film with the CoPt layer thickness of 4 nm measured at room temperature (a), 250 $^{\circ}\text{C}$ (b), and 350 $^{\circ}\text{C}$ (c). The saturation magnetizations (M_S) at various temperatures are shown in (d).

magnetic easy axis will turn to the in-plane direction at high temperatures. Thus, an SRT from out-of-plane to in-plane orientation will be induced. When $d = 2$ nm, the absolute value of the effective volume contribution $-K_V d$ remains lower than the interface contribution $2K_S$, whereas their difference is rapidly reduced. That explains why there is no obvious increase in M_{\parallel} with increasing temperature. When $d = 4$ and 6 nm, CoPt thin films become magnetic isotropy at 230 $^{\circ}\text{C}$ and 100 $^{\circ}\text{C}$, respectively (see the intersections in Figure 5). Hence, M_{\parallel} starts a sharp increase near these temperatures for the two films (Figures 1(b) and 1(c)). The volume effect overwhelms the interface effect at room temperature when d is increased to 8 nm. As a result, only IMA is observed in the whole temperature range and SRT should happen below room temperature, as shown in Figure 1(d).

The abrupt decrease of K_S with temperature is quite different from the linear dependence observed in some other systems, for example, Fe/Cu(100) and Gd/W(110) [7, 10], but similar to the results in Ni/Mo multilayers [22], denoting

the importance of stress effect. K_S always contains the Néel interface anisotropy K_N , which originates from the broken symmetry at the interface [26]. Our previous study found the existence of a tensile stress in CoPt layers after postannealing and demonstrated that such tensile stress promotes a large PMA through magnetoelastic effect [23]. The magnetoelastic anisotropy energy K_{me} can be expressed as $K_{me} = -3\lambda\sigma/2$, where λ is the magnetostriction constant and σ is the internal stress [27]. When the parameters are independent of the film thickness, K_{me} can be identified with a volume contribution K_V . However, in some cases, σ is proportional to $1/d$ due to the accommodation of misfit dislocations [27]. Hence, K_{me} is proportional to $1/d$ and $K_{S,me}$, defined as $K_{S,me} = K_{me}d/2$, becomes a part of the interface contribution K_S . It has been revealed that for the 500 $^{\circ}\text{C}$ annealed CoPt/AlN multilayer films, K_{me} contributes to K_S when $d \geq 2$ nm [28]. Based on the above discussion, K_S in the present work should consist of the Néel interface and magnetoelastic anisotropy terms $K_S = K_N + K_{S,me}$. At room temperature, K_S is 1.0 erg/cm 2 , while K_N

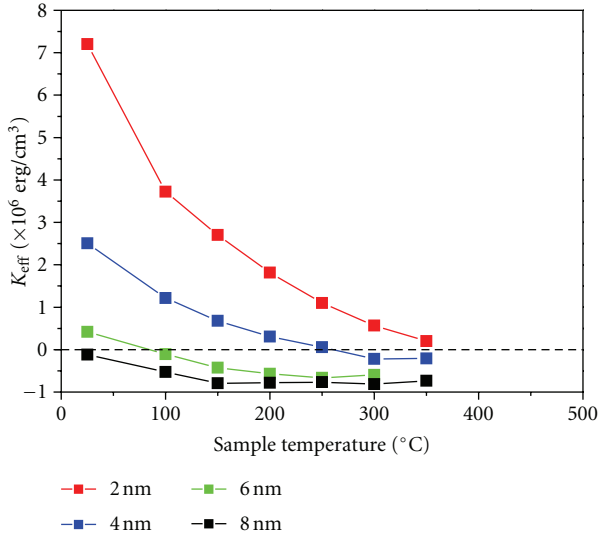


FIGURE 3: Magnetic anisotropy energy K_{eff} versus temperature for CoPt/AlN multilayer films with the CoPt layer thickness as 2, 4, 6, and 8 nm. $K_{\text{eff}} > 0$ and $K_{\text{eff}} < 0$ correspond to perpendicular and in-plane magnetic anisotropy, respectively.

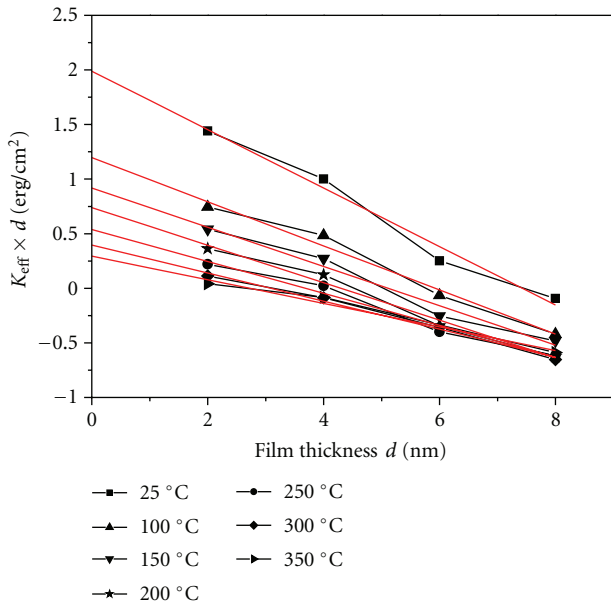


FIGURE 4: $K_{\text{eff}}d$ as a function of CoPt film thickness d at various measuring temperatures. Red lines are linear fit lines to the experiment data.

and $K_{S,\text{me}}$ have been determined to be 0.47 and 0.53 erg/cm² in our previous work, respectively [28]. According to a Néel mean field model, K_N is proportional to M_S^2 , $K_N = AM_S^2$ [22, 29]. The coefficient A is chosen to match the model with the experiment at room temperature. Using the M_S values at various temperatures (Figure 2(d)), the change of K_N with temperature is estimated (Figure 6). Subsequently the temperature dependence of $K_{S,\text{me}}$ is obtained from $K_{S,\text{me}} = K_S - K_N$ (Figure 6). K_N exhibits a much milder temperature

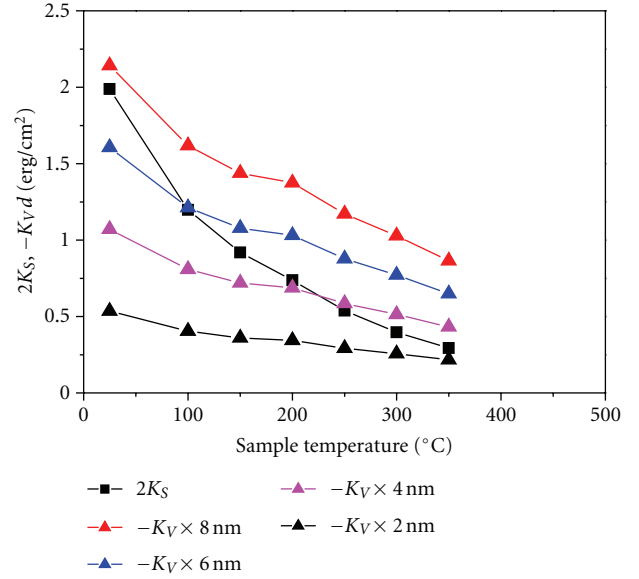


FIGURE 5: $2K_S$ and $-K_V d$ of CoPt/AlN multilayer films with d as 2, 4, 6, and 8 nm against temperature. $2K_S$ is the interface anisotropy energy density and $-K_V d$ is the absolute value of the volume anisotropy energy density.

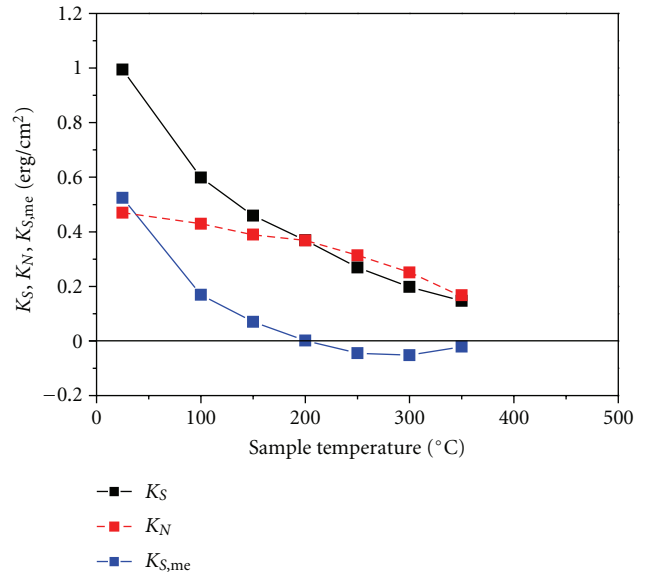


FIGURE 6: K_S , K_N and $K_{S,\text{me}}$ versus temperature. The dash line of K_N denotes it is estimated from a Néel mean field model. $K > 0$ and $K < 0$ correspond to perpendicular and in-plane magnetic anisotropy, respectively.

dependence than $K_{S,\text{me}}$, and thus the rapid decrease of K_S with increasing temperature is dominated by the rapid degradation of $K_{S,\text{me}}$.

The change of $K_{S,\text{me}}$ should be correlated to the change of stress σ , because $K_{S,\text{me}}$ arises from the magnetoelastic effect. At room temperature there exists a large tensile stress in the CoPt film and a compressive strain in the direction of film

normal [23]. When the temperature is increasing, the lattice expands along film normal freely [30]. By contrast, the lattice expansion in the film plane would be restrained to a great extent by adjacent AlN layers through interfacial restriction because of the smaller thermal expansion coefficient and higher elastic modulus of AlN than CoPt [23]. Thus with increasing temperature, the compressive strain along film normal will degrade and further changes to a tensile strain. Therefore, as shown in Figure 6, $K_{S,me}$ rapidly decreases with temperature and reaches nearly zero at 200°C. After that, $K_{S,me}$ becomes negative and favors in-plane magnetization.

4. Conclusions

Temperature dependence of CoPt-AlN interface anisotropy in 500°C annealed CoPt/AlN multilayer films has been investigated. The interface anisotropy in the present work consists of Néel interface anisotropy and the magnetoelastic contribution. Néel interface anisotropy shows a mild temperature dependence, estimated from a Néel mean field model. By contrast, with increasing temperature, the magnetoelastic contribution decreases abruptly and changes its sign above 200°C. Such temperature dependence is owing to the involvement of the stress state in CoPt films. Accordingly, the total interface anisotropy exhibits a rapid degradation with temperature. Due to the milder temperature dependence of volume anisotropy than that of interface anisotropy, interesting temperature driven spin reorientation transition phenomena from out-of-plane to in-plane direction are clearly observed for CoPt/AlN multilayer films with appropriate CoPt layer thickness.

References

- [1] D. P. Pappas, C. R. Brundle, and H. Hopster, "Reduction of macroscopic moment in ultrathin Fe films as the magnetic orientation changes," *Physical Review B*, vol. 45, no. 14, pp. 8169–8172, 1992.
- [2] Z. Q. Qiu, J. Pearson, and S. D. Bader, "Asymmetry of the spin reorientation transition in ultrathin Fe films and wedges grown on Ag(100)," *Physical Review Letters*, vol. 70, no. 7, pp. 1006–1009, 1993.
- [3] S. D. Bader, D. Li, and Z. Q. Qiu, "Magnetic and structural instabilities of ultrathin Fe(100) wedges (invited)," *Journal of Applied Physics*, vol. 76, no. 10, pp. 6419–6424, 1994.
- [4] A. Berger and H. Hopster, "Nonequilibrium magnetization near the reorientation phase transition of Fe/Ag(100) films," *Physical Review Letters*, vol. 76, no. 3, pp. 519–522, 1996.
- [5] D. P. Pappas, K. P. Kämper, and H. Hopster, "Reversible transition between perpendicular and in-plane magnetization in ultrathin films," *Physical Review Letters*, vol. 64, no. 26, pp. 3179–3182, 1990.
- [6] R. Allenspach and A. Bischof, "Magnetization direction switching in Fe/Cu(100) epitaxial films: temperature and thickness dependence," *Physical Review Letters*, vol. 69, no. 23, pp. 3385–3388, 1992.
- [7] A. Enders, D. Peterka, D. Repetto, N. Lin, A. Dmitriev, and K. Kern, "Temperature dependence of the surface anisotropy of Fe ultrathin films on Cu(001)," *Physical Review Letters*, vol. 90, no. 21, Article ID 217203, 4 pages, 2003.
- [8] A. Berger, A. W. Pang, and H. Hopster, "Magnetic reorientation transition in epitaxial Gd-films," *Journal of Magnetism and Magnetic Materials*, vol. 137, no. 1–2, pp. L1–L5, 1994.
- [9] A. Berger, A. W. Pang, and H. Hopster, "Magnetic reorientation transition of Gd(0001)/W(110) films," *Physical Review B*, vol. 52, no. 2, pp. 1078–1089, 1995.
- [10] G. André, A. Aspelmeier, B. Schulz, M. Farle, and K. Baberschke, "Temperature dependence of surface and volume anisotropy in Gd W(110)," *Surface Science*, vol. 326, no. 3, pp. 275–284, 1995.
- [11] R. Allenspach, M. Stampanoni, and A. Bischof, "Magnetic domains in thin epitaxial Co/Au(111) films," *Physical Review Letters*, vol. 65, no. 26, pp. 3344–3347, 1990.
- [12] S. Pütter, H. F. Ding, Y. T. Millev, H. P. Oepen, and J. Kirschner, "Magnetic susceptibility: an easy approach to the spin-reorientation transition," *Physical Review B*, vol. 64, no. 9, Article ID 092409, 4 pages, 2001.
- [13] H. F. Ding, S. Pütter, H. P. Oepen, and J. Kirschner, "Spin-reorientation transition in thin films studied by the component-resolved Kerr effect," *Physical Review B*, vol. 63, no. 13, Article ID 134425, 7 pages, 2001.
- [14] R. Sellmann, H. Fritzsche, H. Maletta, V. Leiner, and R. Siebrecht, "Spin-reorientation transition and magnetic phase diagrams of thin epitaxial Au(111)/Co films with W and Au overlayers," *Physical Review B*, vol. 64, no. 5, Article ID 054418, 2001.
- [15] W. L. O'Brien and B. P. Tonner, "Transition to the perpendicular easy axis of magnetization in Ni ultrathin films found by x-ray magnetic circular dichroism," *Physical Review B*, vol. 49, no. 21, pp. 15370–15373, 1994.
- [16] W. L. O'Brien, T. Droubay, and B. P. Tonner, "Transitions in the direction of magnetism in Ni/Cu(001) ultrathin films and the effects of capping layers," *Physical Review B*, vol. 54, no. 13, pp. 9297–9303, 1996.
- [17] B. Schulz and K. Baberschke, "Crossover from in-plane to perpendicular magnetization in ultrathin Ni/Cu(001) films," *Physical Review B*, vol. 50, no. 18, pp. 13467–13471, 1994.
- [18] M. Farle, W. Platow, A. N. Anisimov, B. Schulz, and K. Baberschke, "The temperature dependence of magnetic anisotropy in ultra-thin films," *Journal of Magnetism and Magnetic Materials*, vol. 165, no. 1–3, pp. 74–77, 1997.
- [19] M. Farle, B. Mirwald-Schulz, A. N. Anisimov, W. Platow, and K. Baberschke, "Higher-order magnetic anisotropies and the nature of the spin-reorientation transition in face-centered-tetragonal Ni(001)/Cu(001)," *Physical Review B*, vol. 55, no. 6, pp. 3708–3715, 1997.
- [20] M. Farle, "Ferromagnetic resonance of ultrathin metallic layers," *Reports on Progress in Physics*, vol. 61, no. 7, pp. 755–826, 1998.
- [21] R. Bergholz and U. Gradmann, "Structure and magnetism of oligatomic Ni(111)-films on Re(0001)," *Journal of Magnetism and Magnetic Materials*, vol. 45, no. 2–3, pp. 389–398, 1984.
- [22] M. J. Pechan, "Temperature dependence of interface anisotropy in Ni/Mo multilayers," *Journal of Applied Physics*, vol. 64, no. 10, pp. 5754–5756, 1988.
- [23] Y. Hodumi, J. Shi, and Y. Nakamura, "Controlling the magnetic anisotropy of CoPt/AlN multilayer films," *Applied Physics Letters*, vol. 90, no. 21, Article ID 212506, 2007.
- [24] Y. Yu, J. Shi, and Y. Nakamura, "Thickness-dependent perpendicular magnetic anisotropy of CoPt top layer on CoPt/AlN multilayer," *IEEE Transactions on Magnetics*, vol. 46, no. 6, pp. 1663–1666, 2010.
- [25] W. P. Cai, J. Shi, Y. Nakamura, W. Liu, and R. H. Yu, "Roles of L1₀ ordering in controlling the magnetic anisotropy and

- coercivity of (111)-oriented CoPt ultrathin continuous layers in CoPt/AlN multilayer films,” *Journal of Applied Physics*, vol. 110, no. 7, Article ID 073907, 2011.
- [26] L. Neel, “Anisotropie magnetique superficielle et surstructures d’orientation,” *Journal de Physique et Le Radium*, vol. 15, no. 4, pp. 225–239, 1954.
- [27] M. T. Johnson, P. J. H. Bloemen, F. J. A. Den Broeder, and J. J. De Vries, “Magnetic anisotropy in metallic multilayers,” *Reports on Progress in Physics*, vol. 59, no. 11, pp. 1409–1458, 1996.
- [28] Y. X. Yu, *Perpendicular magnetic anisotropy in CoPt/AlN layered structures: roles of internal stress and interface roughness*, [Ph.D. dissertation], Tokyo Institute of Technology, 2011.
- [29] U. Gradmann and J. Muller, “Flat ferromagnetic epitaxial 48Ni/52Fe(111) films of few atomic layers,” *Physica Status Solidi*, vol. 27, no. 1, pp. 313–324, 1968.
- [30] W. P. Cai, S. Muraishi, J. Shi, Y. Nakamura, W. Liu, and R. H. Yu, “Curie temperatures of CoPt ultrathin continuous films,” *Applied Physics A-Materials Science & Processing*, vol. 107, no. 3, pp. 519–523, 2012.

Research Article

Electronic Structure of $\text{BiFe}_{1-x}\text{Mn}_x\text{O}_3$ Thin Films Investigated by X-Ray Absorption Spectroscopy

Abduleziz Ablat,^{1,2} Emin Muhemmed,¹ Cheng Si,¹ Jiaou Wang,¹ Haijie Qian,¹ Rui Wu,¹ Nian Zhang,¹ Rong Wu,² and Kurash Ibrahim¹

¹Beijing Synchrotron Radiation Facility, Institute of High Energy Physics, CAS, Beijing 100049, China

²School of Physical Science and Technology, Xinjiang University, Urumqi 830046, China

Correspondence should be addressed to Kurash Ibrahim, kurash@ihep.ac.cn

Received 7 March 2012; Accepted 21 April 2012

Academic Editor: Weichang Hao

Copyright © 2012 Abduleziz Ablat et al. This is an open access article distributed under the Creative Commons Attribution License, which permits unrestricted use, distribution, and reproduction in any medium, provided the original work is properly cited.

Multiferroic polycrystalline $\text{BiFe}_{1-x}\text{Mn}_x\text{O}_3$ ($0 \leq x \leq 0.3$) thin films have been prepared on the Pt(111)/Ti/SiO₂/Si(100) substrates by pulsed laser deposition method. The influence of Mn substitution on the electronic structure and magnetic properties has been studied. X-ray diffraction spectroscopy shows that Mn substitution slightly modulates crystal structure of the $\text{BiFe}_{1-x}\text{Mn}_x\text{O}_3$ system within the same structural phase. According to Fe *L* edge X ray absorption spectroscopy, Fe ions are found to be formally trivalent for doping amount *x* in $\text{BiFe}_{1-x}\text{Mn}_x\text{O}_3$. The enhanced magnetization by increasing Mn content is attributed to an alternation degree of hybridization between Fe 3*d*-O 2*p* and Mn 3*d*-O 2*p* orbitals, basing on the carefully examined Fe *L* and O *K* edge X-ray absorption spectroscopy. The crystal structural and the electronic structural results show a causal relation between them by demonstrating intrinsic mutual dependence between respective variations.

1. Introduction

Multiferroics are a group of materials which simultaneously show up several kinds of ferroic properties such as ferroelectricity, ferromagnetism, and ferroelasticity in the same phase [1]. In ferromagnetic-ferroelectric multiferroics, magnetization can be tuned by an applied electric field and electronic polarization by magnetic field [2]. The magneto-electric (ME) effects of multiferroics imply important technological application perspectives in multifunctional devices like high-temperature transistor gate, memory device, and spintronics. Few multiferroics exhibits as natural occurring phases, examples of which include YMnO_3 , PbVO_3 , BiCrO_3 , BiMnO_3 and BiFeO_3 (BFO) [3, 4]. Among them only the BFO exhibits ME effects at room temperature. Although the BFO is considered to be a room-temperature multiferroics, its ME effect is too low because of weak ferromagnetism. Two different approaches have been used for enhancing the ME effect in BFO. One is to bring the ferroelectric T_C or ferromagnetic T_N transition temperature to around room temperature by cationic substitutions [5]. The other

is first to achieve phase transition from antiferromagnetic to ferromagnetic and then increase magnetic properties while retaining the ferroelectricity through strain modification [6, 7]. Among these, Mn doping is the most common method to achieve an enhanced magnetization. This is because the BiMnO_3 —a Mn centered compound of BiMO_3 series—exhibits ferromagnetism below ~ 105 K and ferroelectric at ~ 450 K [8]. The BiMnO_3 has a large ferromagnetic magnetization, implying that the Mn doping in BFO improves the magnetization and enhances the ME effects more effectively than other element substitution. Mechanisms for the increasing magnetization in Mn-doped BFO systems have been discussed in terms of canting of the antiferromagnetically ordered spins by structural distortion [9], double exchange interaction induced by hole doping effects [10], and variation of Fe^{3+} ion concentration [11]. Investigation in terms of electronic structure is a direct way to understand the macroscopic properties of materials, due to intrinsic relationship between the electronic structure and macroscopic properties.

In this work, we prepared Mn-substituted $\text{BiFe}_{1-x}\text{Mn}_x\text{O}_3$ (BFMO) thin films by pulsed laser deposition (PLD). The crystal structure, surface morphology, magnetic properties, and electronic structure of the Mn-doped BFMO systems were investigated via X-ray diffraction (XRD), scanning electron microscopy (SEM), Alternating Gradient force Magnetometer (AGM), and X-ray absorption spectroscopy (XAS). Origin for the enhanced magnetization of the BFMO system with increased Mn amount of doping is investigated in terms of their electronic structural changes.

2. Experiment

The $\text{BiFe}_{1-x}\text{Mn}_x\text{O}_3$ ($0 \leq x \leq 0.3$) films were prepared by PLD method on the Pt(111)/Ti/SiO₂/Si(100) substrates in a PLD chamber connected to the photoemission spectroscopy (PES) system at 4B9B beam line of the Beijing Synchrotron Radiation Facility. Ceramic BFMO targets of 20 mm diameter 2 mm thick for PLD were prepared by sintering the mixtures of Bi₂O₃ (99.99 at.%), Fe₂O₃ (99.99 at.%), and Mn₂O₃ (99.99 at.%) at 820°C in air, following the solid state reaction routine way. Slight excess of Bi₂O₃ has been added to compensate the preferential loss of bismuth during sintering. The XRD result of the target material indicates that the sample is in single phase of polycrystalline BFMO.

Before deposition, the Pt(111)/Ti/SiO₂/Si(100) substrate was preheated at 700°C to eliminate surface contamination. The substrate temperature and oxygen ambient pressure were maintained at 550°C and 5.6 Pa, respectively. During the deposition, the laser fluence was at 2.3 J/cm² and the pulse repetition rates 1.5 Hz. After deposition, all the films were annealed at same condition for 30 minutes and then transferred under a background pressure of $\sim 10^{-8}$ Pa to the PES chamber to carry out *in situ* XAS measurements. The overall energy resolution was 0.2–0.7 eV, depending on the photon energies. All the spectra were recorded at room temperature, and the XAS measurement was carried out with total electron yield (TEY) detection mode. After the *in situ* measurements, the films were taken for *ex situ* crystal structure characterization by XRD, surface morphology by SEM, and magnetic AGM measurements.

3. Result and Discussion

3.1. Structure and Microstructure Characterization. XRD spectra were recorded at room temperature on an (MSAL-XD2) X-ray diffractometer with a Cu K α source ($\alpha = 1.5418 \text{ \AA}$) in Bragg-Brentano geometry. Figure 1(a) shows the X-ray diffraction patterns of $\text{BiFe}_{1-x}\text{Mn}_x\text{O}_3$ ($x = 0, 0.1, 0.2, \text{ and } 0.3$) thin films deposited on Pt(111)/Ti/SiO₂/Si(100) substrate without buffer layers. The BFO films, which are directly deposited on the Pt-buffered substrates, often exhibit a polycrystalline structure with one or more secondary phases [12, 13]. In comparison, in this work all the films are in single-phase polycrystalline structure with rhombohedral space group (R3c) and no other peak related to secondary phases was detected. It is also interesting to notice that a varied Mn substitution results in the regulation of the crystal

orientation of the $\text{BiFe}_{1-x}\text{Mn}_x\text{O}_3$ thin films. Figure 1(b) shows the enlarged XRD patterns of films in the 2-theta range 20–24. Relative to that of pure BFO film, the (100) peaks of Mn doped show a slight shift to higher angle with a similar peak shapes and structures, confirming that the Fe ion substitution by Mn in BFO films. Except the rigid shift of the peak positions of doped sample compare to the undoped one, and a slight modulation of the (100) peak width in the doping range, crystalline structure of BFO has been affected little by the substitutional doping of Mn, in agreement with the rhombohedral structure of BFO unchanged up to 30% of Mn doping [5, 10].

The morphological SEM images of the $\text{BiFe}_{1-x}\text{Mn}_x\text{O}_3$ ($x = 0, 0.1, 0.2, 0.3$) thin films on Pt(111)/Ti/SiO₂/Si(100) substrate are shown in Figure 2. The SEM image of undoped BFO film, in Figure 2(a), reveals nonuniform growth of grains with wide pores between grains and an averagely different grain sizes. The Mn doping significantly affects the morphologies of BFMO thin films (Figure 2(b), 2(c), and 2(d)), the films become denser, the grain sizes tend to be smaller in (b) and (c), the grain boundaries are blurred, and the pores between grains are reduced. Larger pores between the grains of undoped and 30% Mn-doped thin films are consistent with the weaker diffraction intensity of those films in Figure 1(a).

The XRD peaks and the SEM images, as direct indicators for atomic long-range ordering level and macroscopic morphology of crystal, both provide mutual-revealing clues on what has happened in atomistic level of the systems along with variational condition, such as doping in the underlying case. The grain size variation observed in the SEM images shows a consistent relation with the peak width in the XRD; that is, the larger the grain sizes are, the wider the observed XRD peaks are, though the latter at a poorer statistical level. When all the samples keeping the phase of crystal structure within the same R3c symmetry group, the facts such as the rigid peak positions shift of (100), gradual disappearance of peak (110), and the various morphological show-up of the crystal films against the Mn doping imply the systems undergone certain kind of electronic structural modulation, instead of the results from simple mixing of different radius ball-like elements.

Change in 2θ implies a change in d-spacing of lattice parameters. The (100) lattice parameter a and the diffraction 2θ angle have the relation $\propto 1/\sin \theta$ the small amount up-shift of the 2θ implies a decrease in the a with the Mn doping. The rigidness of the shift by reaching a fixed position all at once reflects that, first of all, the sensitivity of the electronic structure to the doping rather than the doping amount, secondly, the dopant distribution uniformity of the substitution. We attribute the d-spacing decrease and the rigid shift of 2θ to electronic structural effects, rather than a different size elemental mixing effects. If it was the latter effects, as it has been shown clearly for Fe-Al mixing in [14], the smaller size Fe substitution of larger size Al drove a continuous decrease of lattice parameters with their relative percentage, in the underlying case we would have observed a scenario where the lattice parameters were increasing and the 2θ degree decreasing continuously following the fact that

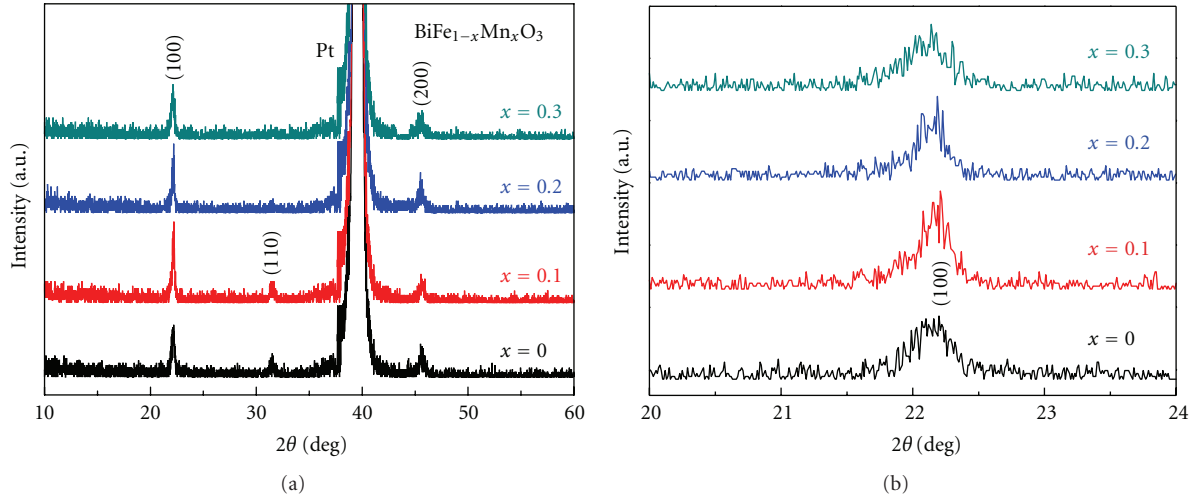


FIGURE 1: X-ray diffraction (XRD) patterns of $\text{BiFe}_{1-x}\text{Mn}_x\text{O}_3$ ($x = 0, 0.1, 0.2, 0.3$) films on Pt(111)/Ti/SiO₂/Si(100) substrate: (a) 2θ from 10 to 60; (b) enlarged 2θ of (100) from 20 to 24.

the Mn atom has a larger radius than that of Fe. All these are clearly in a contrary way of the above simple elemental situation. The disappearance of the (110) indexing surface with the Mn doping can be taken to be a direct result in the electronic structural regulation. This can be due to randomization, distortion or breakdown of the (110) surface, but certainly not due to, continuously changing grain sizes; this is not the case shown in the measured SEM images. The electronic structural effects in the underlying case are mostly by modulation of the hybridization interactions between Fe-O and Mn-O two pair elements, as they are discussed through the XAS results at Fe L edge and O K edge in the following sections. The observed electronic structural variations with doping provide an affirmative standing point for the XRD and SEM observations.

3.2. Fe L Edge X-Ray Absorption Spectroscopy. The Fe $2p$ XAS spectra of BFO system in Figure 3(a), along with the spectra of reference trivalent Fe_2O_3 (Fe^{3+}) and divalent FeO (Fe^{2+}) oxides [15], provide information on the unoccupied Fe $3d$ states. The Fe $3d$ orbitals split by exchange interaction into majority (spin up \uparrow) and minority (spin down \downarrow) states. Each state further splits by the octahedral crystal ligand field into t_{2g} and e_g orbitals. In the Fe L edges XAS spectra, the lower energy shoulder of Fe L_3 corresponds to the unoccupied $t_{2g}\downarrow$ states and the sharper one to the unoccupied $e_g\downarrow$ states. Similar to L_3 edge, the L_2 edge also splits into two $t_{2g}\downarrow$ and $e_g\downarrow$ states. The energy separation between $t_{2g}\downarrow$ and $e_g\downarrow$ states is called octahedral crystal field $10Dq$ value (or the distance between the t_{2g} and e_g). Measured energy separation between $t_{2g}\downarrow$ and $e_g\downarrow$ states for all the samples is ~ 1.6 eV. This leads the Fe $3d$ electrons to stay at high-spin configuration $t_{2g}^3 e_g^2$ (${}^6A_{1g}$), like the Fe $3d$ electrons in LaFeO_3 .

The line shape of the Fe $2p$ XAS provides information on the valence state of the Fe ions. The spectra show that the line shapes of all the doped samples are similar to that of Fe_2O_3 and quite different from that of FeO . These indicate

that the Fe ions keep formally in trivalent (Fe^{3+}) states with the doping, consistent with literature report [16].

The change in peak intensity and peak width reflects a modulation in the electron density of state distribution between the Fe $3d$ and ligand O $2p$ with doping. In Figure 3(b), the $t_{2g}\downarrow$ peak weight estimated by the $I_{t_{2g}}/(I_{t_{2g}} + I_{e_g})$ intensity ratio and the L_3 edge FWHM (full width at half maximum) by arithmetic sum of $t_{2g}\downarrow$ and of $e_g\downarrow$ peaks' FWHM show explicit variation trends. As x increases, the intensity of $t_{2g}\downarrow$ state increases from 0.364 at $x = 0$ to 0.408 at $x = 0.3$; at the same time, the L_3 edge peak width shrinks from 1.63 eV to 1.41 eV. Origin for these variations can be understood in terms of the doping-driven hybridization strength modification between the Fe $3d$ and O $2p$ states. The starting point is put on the valence band state of the $x = 0$ undoped BFO system. The BFO system is assumed to be $\text{Fe } 3d^5 + \text{Fe } 3d^6\bar{L}$ (\bar{L} represents the ligand hole state $\text{O } 2p^5\bar{L}$ formed by a charge transfer from $\text{O } 2p^6$ to $\text{Fe } 3d^5$) mixture states derived by the Fe $3d$ and O $2p$ hybridization. The $\text{Fe } 3d^6\bar{L}$ state is induced by charge transfer from the ligand O $2p$ to Fe $3d$. The $t_{2g}\downarrow$ state intensity change indicates an increase of the Fe $3d^5$ portion with the doping and correspondingly implies a decrease of the Fe $3d^6\bar{L}$ charge transfer state. The simultaneous peak width narrowing can be discussed analogously to the intensity change as result of the hybridization strength decrease. The O $2p$ ligand valence band is of 5.5 to 6 eV wide [17]; a stronger hybridization effect in the pure BFO induces higher portion of $\text{Fe } 3d^6\bar{L}$ in the $\text{Fe } 3d^5 + \text{Fe } 3d^6\bar{L}$ mixed state then gives the observed weaker intensity and larger peak width due to delocalization. At the same time, the reduced hybridization effect along the Mn doping brings about an increase of the Fe $3d^5$ portion in the $\text{Fe } 3d^5 + \text{Fe } 3d^6\bar{L}$ states. Main causes of the current observation at the Fe L edge, in a self-consistent way with an increased hybridization strength between Mn $3d$ -O $2p$, are clearly seen affirmatively through the below O K edge XAS measurement results.

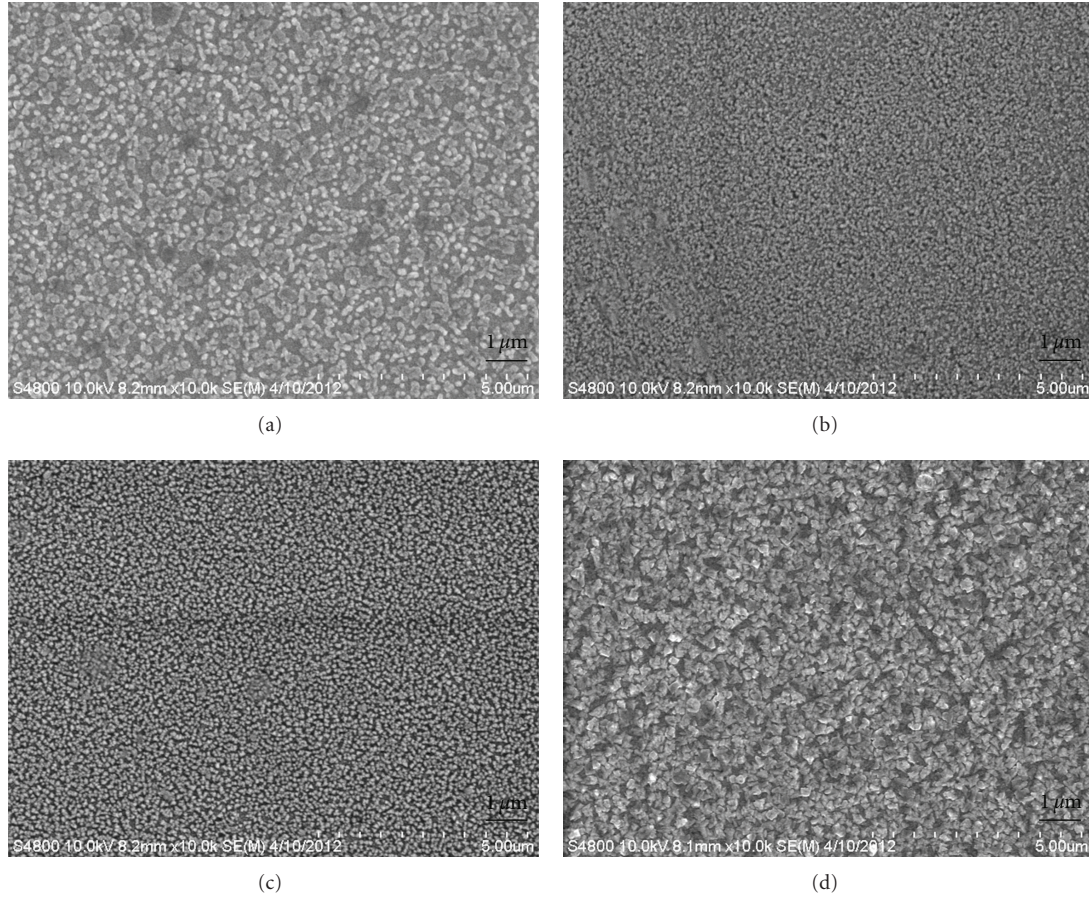


FIGURE 2: SEM images of $\text{BiFe}_{1-x}\text{Mn}_x\text{O}_3$ ($x = 0, 0.1, 0.2, 0.3$) films with the composition of (a) $x = 0$; (b) $x = 0.1$; (c) $x = 0.2$; (d) $x = 0.3$ prepared on Pt(111)/Ti/SiO₂/Si(100) substrate. The images are obtained with weak contrast due to fast saturation charging effect.

3.3. Oxygen K Edge X-ray Absorption Spectroscopy. The O K-edge XAS spectra, shown in Figure 4(a), are labeled a, b, and c. The relative intensity change of the peak a's shoulder and the FWHM of the double-peak a, as shown in Figure 4(b), are obtained with the same way as that of the Fe 2p XAS results shown in Figure 3(b). The M $3d^{n+1}\underline{L}$ characteristic peak intensity increases from ~ 0.1 to ~ 0.21 with the Mn content change 0 through 0.3, and at the same time the peaks' width decreases from 1.95 eV to 1.25 eV.

The O 1s XAS measurement provides holistic information on the O 2p hybridization with transition metals M $3d^n + M 3d^{n+1}\underline{L}$ states where the M $3d^n + M 3d^{n+1}\underline{L}$ represents the $[\text{Fe } 3d^5 + \text{Fe } 3d^6\underline{L}] + [\text{Mn } 3d^4 + \text{Mn } 3d^5\underline{L}]$ mixture states. The spectral structure reflects the density of states of M $3d^{n+1}\underline{L}$ portion in M $3d^n + M 3d^{n+1}\underline{L}$ mixed states, since the hole state \underline{L} of O 2p characteristic orbitals results in the charge transfer *via* hybridization interactions between M $3d$ and O 2p. The a double-peak structure including the arrow pointing shoulder is of the O 2p characteristic M $3d^{n+1}\underline{L}$ part in the M $3d^n + M 3d^{n+1}\underline{L}$ states and these states are about the shoulder $t_{2g}\downarrow$ and the main peak $e_g\downarrow$ states, respectively [18]. When the density of the hole-state \underline{L} at ligand side is high, the higher the intensity of peaks' a is observable. The band b is attributed to the hybridization of O 2p with Bi 6sp states

and the c at ~ 542 eV to the hybridization of O 2p with Fe 4sp, Mn 4sp orbitals.

In this section we pay special attention to the double-peak a due to it is about the M $3d^{n+1}\underline{L}$ state. The above Fe 2p XAS results, which are for the Fe $3d^5$ portion of Fe $3d^5 + \text{Fe } 3d^6\underline{L}$ mixed states, have reached the conclusion that the Fe $3d^6\underline{L}$ density of state decreases and correspondingly the Fe $3d^5$ state increases with the Mn doping. Now at O K edge, we see that the M $3d^{n+1}\underline{L}$ characteristic peak intensity increases, and simultaneously the peaks' width decreases with the Mn doping, as shown in Figure 4(b).

At the O K edge, the increase of $t_{2g}\downarrow$ characteristic M $3d^{n+1}\underline{L}$ intensity with Mn doping reflects the fact that available \underline{L} states at the ligand side are increasing, and this is by an enhanced hybridization effect which drives the charge transfer from ligand to metal ions. The M $3d^{n+1}\underline{L}$ state includes contributions from both states Fe $3d^6\underline{L}$ and Mn $3d^5\underline{L}$. In the underlying system, the decrease of Fe $3d^6\underline{L}$ density of state and correspondingly the increase of Fe $3d^5$ with Mn have been proved by the XAS results at Fe L edge. The intensity increase of the M $3d^{n+1}\underline{L}$ state at O K edge, then, uniquely corresponds to the increase of Mn $3d^5\underline{L}$ density of state, and simultaneously a decrease of Mn $3d^4$ state with the doping. The double-peak width

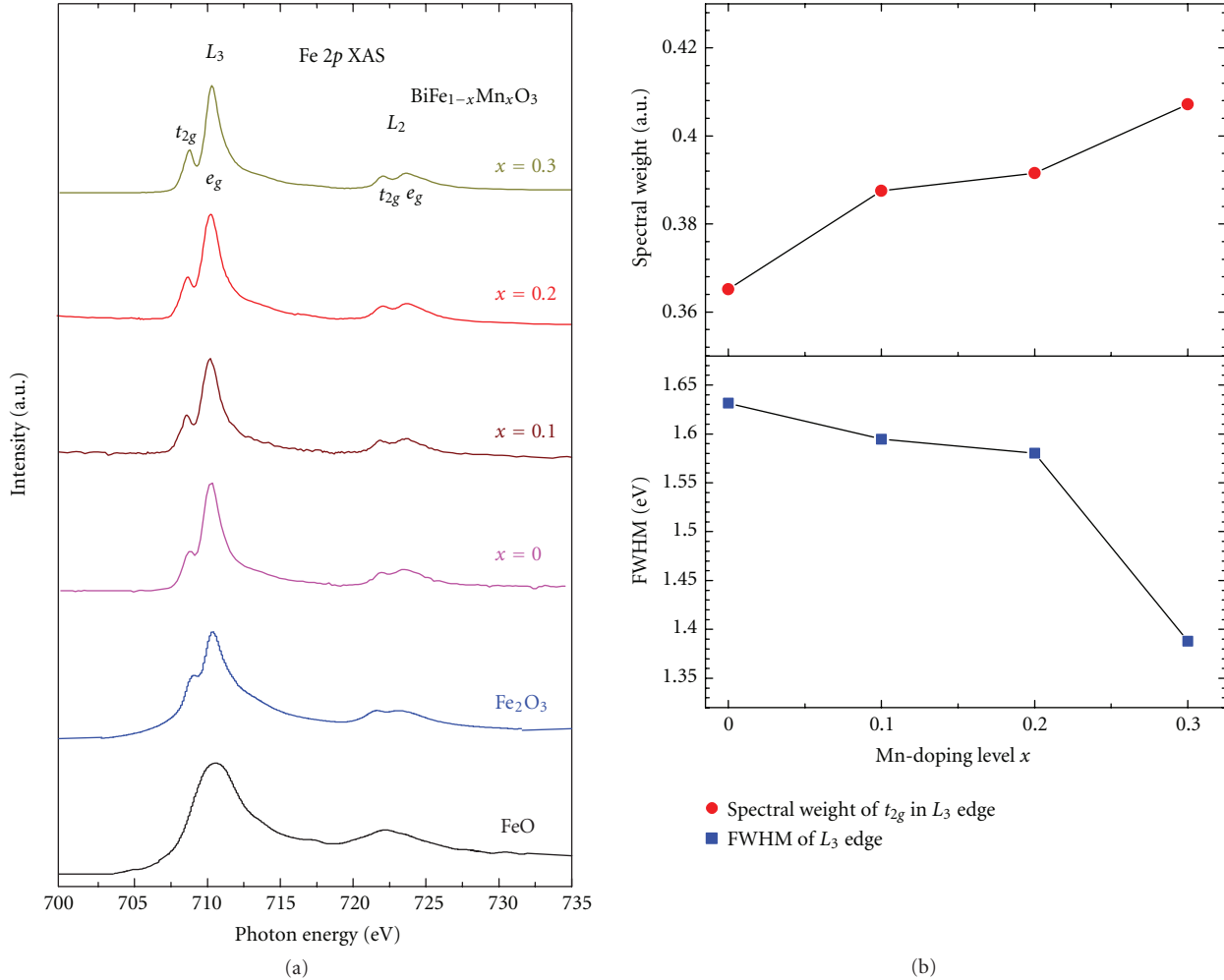


FIGURE 3: (a) Comparison of the Fe 2p XAS of BiFe_{1-x}Mn_xO₃ (0 ≤ x ≤ 0.3) with those of FeO and Fe₂O₃; (b) FWHM of L₃ edge and spectral weight of t_{2g} in L₃ edge as a function of x.

decrease at the O K edge implies that the localization of Mn 3d⁵L states is enhanced with the Mn doping. These results indicate a scenario that the Fe 3d-O 2p hybridization strength weakens with the enhanced Mn 3d-O 2p hybridization effect in the BFMO thin films.

3.4. Magnetic Properties. The magnetic hysteresis (M-H) curves of the films measured at room temperature are shown in Figure 5. The M-H curves indicate typical ferromagnetic characters. The pure BFO thin film shows a weak ferromagnetic behavior in slim magnetic loops (Ms) of 28.7 emu/cm³, since it is in a rhombohedral distorted perovskite structure and allows a weak ferromagnetic ordering due to canting of the spins [19]. The magnetization value of pure BFO films in this work almost same with other reports [7]. The Ms of the samples at x = 0.1, x = 0.2, and x = 0.3 are 31.2, 40.3, and 47.7 emu/cm³, respectively (inset of Figure 5). These values are higher than those of their corresponding bulk samples [20]. This increasing trend of Ms through Mn doping agrees with that of other reports about BFMO thin

films and ceramics [11, 21, 22]. The coercive field (H_C) decreases with the increase of Mn composition.

The increase in macroscopic magnetization with the increase of Mn content (inset of Figure 5) was attributed to either structural transition or exhibition of certain amount of Fe²⁺/Fe³⁺ mixed ions in films [9, 11]. XPS results (not shown here) and the Fe L edge XAS show formal Fe³⁺ only composition and no trace of Fe²⁺ demonstrating. From the XRD results, however, there is no clear evidence for a phase transition such as from rhombohedral to tetragonal or other phases with Mn doping. These imply the BFMO thin films magnetization enhancement could not be from the different valence states of Fe ions. It also does not originate from the misfit strain by different films thickness [7, 23], since all the BFMO films were grown with a same film thickness, that is, the films deposition rates monitored in situ by crystal oscillator during growth process. Enhancement of the Ms with Mn doping is actually due to change in the electron density of state distributions between Fe-O and Mn-O pairs through variation of hybridization interactions, as discussed in section below.

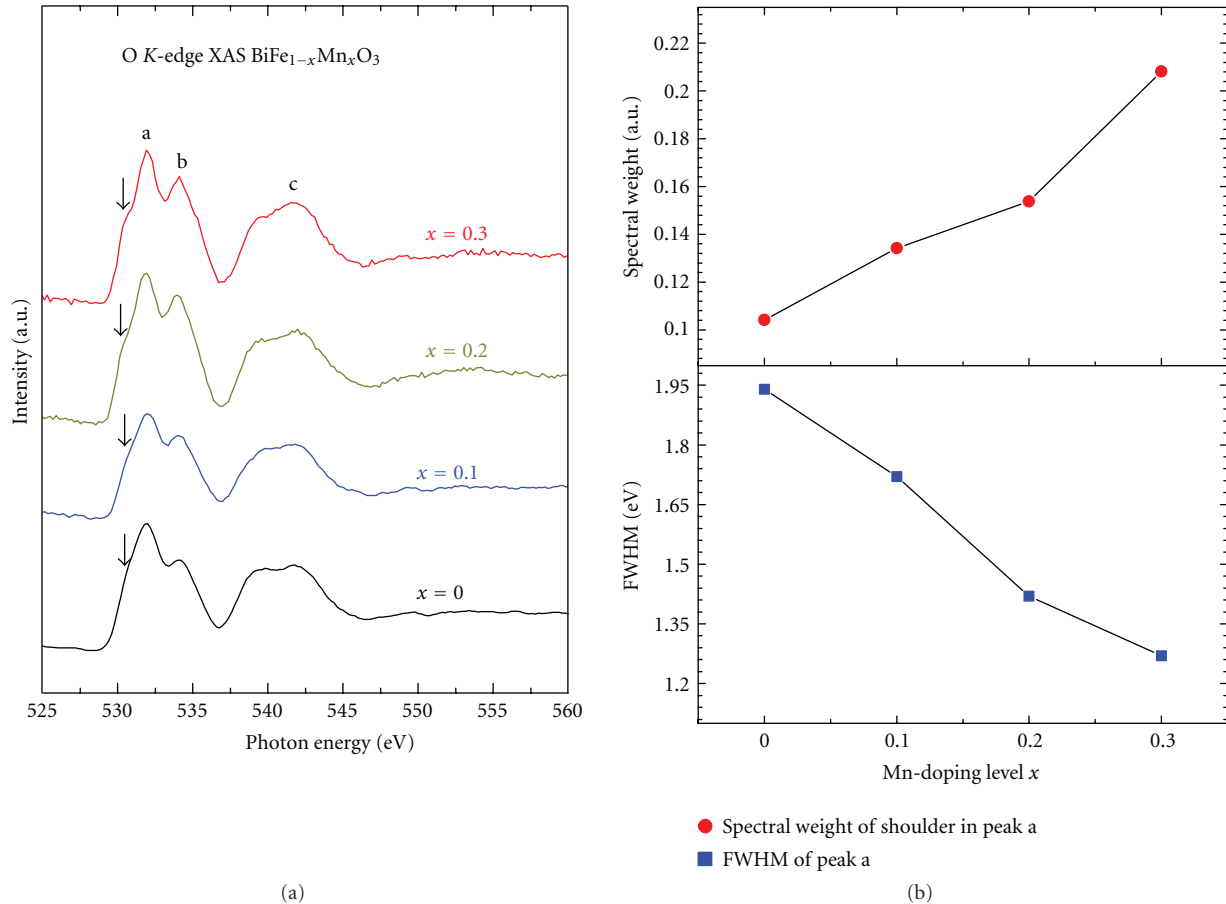


FIGURE 4: (a) O K-edge XAS spectra of BiFe_{1-x}Mn_xO₃ thin films with $x = 0, 0.1, 0.2,$ and 0.3 doping levels. (b) Spectral weight of the shoulder in peak a and the FWHM of peak a as function of x .

Concerning the magnetic property of doped ceramic system, in an early work on the role of covalency in magnetic property of an A-site-doped ABO₃ (e.g., La³⁺ substitution with Sr²⁺ in the LaMnO₃) perovskite-type manganite La_{1-x}Sr_xMnO₃ [24], Goodenough assumed that inhomogeneity in the bonding nature of the central cations Mn³⁺ and Mn⁴⁺ with anion O²⁻ by forming a mixed state of ionic, covalent, or semicovalent bonds could be the major driving force for ferromagnetic property observed in the system. The basic idea behind is that if the Mn³⁺-O²⁻ bond has more ionic character and the Mn⁴⁺-O²⁻ with more covalency or semicovalency, the bonding inhomogeneity with greater separation for ionic bonding and shorter for covalence will ease the barrier of ferromagnetic moment in the Mn³⁺(3d⁴)-O²⁻-Mn⁴⁺(3d³) chain. The observed ferromagnetic results in the underlying BFMO system in the Mn³⁺(3d⁴)-O²⁻-Fe³⁺(3d⁵) chain, analogous to the case suggested for the Mn³⁺(3d⁴)-O²⁻-Mn⁴⁺(3d³) chain, demonstrate a good agreement to the assumption, showing an increase of ionic bond character for Fe³⁺-O²⁻ as observed at Fe 2p edge XAS and an increase of covalence bonding for Mn³⁺-O²⁻ at O K edge XAS. Apparently, the increase of the magnetism in the underlying system with the Mn doping

associates closely to the bonding inhomogeneity created in the Mn³⁺(3d⁴)-O²⁻-Fe³⁺(3d⁵) chains with the Mn doping.

4. Conclusion

In summary, the polycrystalline multiferroic BiFe_{1-x}Mn_xO₃ ($0 \leq x \leq 0.3$) thin films were grown by PLD techniques. The X-ray diffraction spectroscopy shows Mn content up to $x = 0.3$ is in single phase having a rhombohedral crystalline structure. The crystal structural variation with Mn doping is attributed to the electronic structural modulation, instead of different size elemental mixing. Mn doping brings about an increase of the Fe 3d⁵ portion in the Fe 3d⁵ + Fe 3d⁶L states and spontaneous decrease of Mn 3d⁴ portion in the Mn 3d⁴ + Mn d⁵L mixed states. The observed increase in Ms with increasing Mn concentration was closely related with the electronic density of state distribution changes. Increase in the Mn concentration reduces the charge transfer between the Fe 3d and O 2p and leads to the bond inhomogeneity in the Fe-O-Mn chains; these change driven by the hybridization interactions are responsible for the magnetization enhancement, as well as the observed slight modulation in crystal structures.

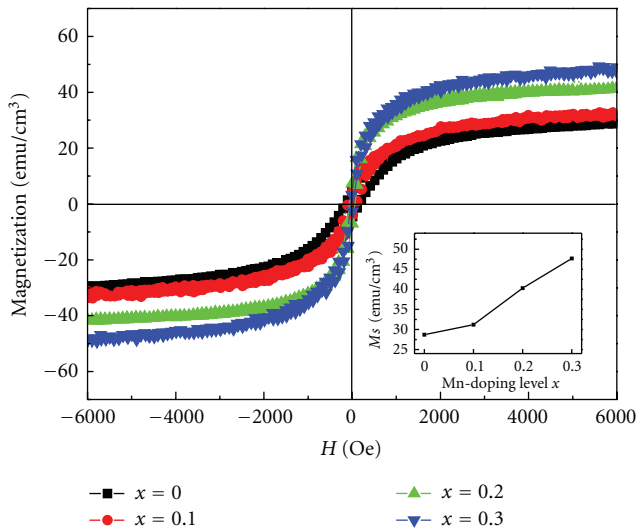


FIGURE 5: Magnetic hysteresis (M-H) curves measured at room temperature for the $\text{BiFe}_{1-x}\text{Mn}_x\text{O}_3$ thin films with $x = 0, 0.1, 0.2,$ and 0.3 . The inset shows the magnetization (M_s) plotted as a function of Mn-doping level.

Acknowledgments

The authors acknowledge the financial support from Chinese Academy of Sciences under Grant no. H91G750Y21, and National Natural Science Foundation of China (Grant no. 11164026).

References

- [1] W. Eerenstein, N. D. Mathur, and J. F. Scott, "Multiferroic and magnetoelectric materials," *Nature*, vol. 442, no. 7104, pp. 759–765, 2006.
- [2] M. Fiebig, T. Lottermoser, D. Frohlich, A. V. Goltsev, and R. V. Pisarev, "Observation of coupled magnetic and electric domains," *Nature*, vol. 419, no. 6909, pp. 818–820, 2002.
- [3] N. A. Hill, "Why are there so few magnetic ferroelectrics?" *Journal of Physical Chemistry B*, vol. 104, no. 29, pp. 6694–6709, 2000.
- [4] R. Ramesh and N. A. Spaldin, "Multiferroics: progress and prospects in thin films," *Nature Materials*, vol. 6, no. 1, pp. 21–29, 2007.
- [5] C. H. Yang, T. Y. Koo, and Y. H. Jeong, "How to obtain magnetocapacitance effects at room temperature: the case of Mn-doped BiFeO_3 ," *Solid State Communications*, vol. 134, no. 4, pp. 299–301, 2005.
- [6] M. S. Kartavtseva, O. Y. Gorbenko, A. R. Kaul, and T. V. Murzina, "The influence of epitaxial strain on magnetic and electrical properties of BiFeO_3 thin films," *Thin Solid Films*, vol. 518, no. 16, pp. 4750–4752, 2010.
- [7] F. Z. Huang, X. M. Lu, W. W. Lin et al., "Thickness-dependent structural and magnetic properties of BiFeO_3 films prepared by metal organic decomposition method," *Applied Physics Letters*, vol. 97, no. 22, Article ID 222901, 2010.
- [8] A. M. dos Santos, S. Parashar, A. R. Raju, Y. S. Zhao, A. K. Cheetham, and C. N. R. Rao, "Evidence for the likely occurrence of magnetoferroelectricity in the simple perovskite, BiMnO_3 ," *Solid State Communications*, vol. 122, no. 1–2, pp. 49–52, 2002.
- [9] K. Takahashi and M. Tonouchi, "Influence of Mn doping on ferroelectric-antiferromagnet BiFeO_3 thin films grown on $(\text{LaAlO}_3)_{0.3}(\text{Sr}_2\text{AlTaO}_6)_{0.7}$ substrates," *Japanese Journal of Applied Physics Part 2*, vol. 45, no. 29–32, pp. L755–L757, 2006.
- [10] M. Kumar and K. L. Yadav, "Rapid liquid phase sintered Mn doped BiFeO_3 ceramics with enhanced polarization and weak magnetization," *Applied Physics Letters*, vol. 91, no. 24, Article ID 242901, 2007.
- [11] J. J. Gu, G. L. Zhao, F. W. Cheng, J. R. Han, L. H. Liu, and H. Y. Sun, "Magnetoelectric properties of Mn-substituted BiFeO_3 thin films with a TiO_2 barrier," *Physica B*, vol. 406, no. 23, pp. 4400–4403, 2011.
- [12] M. H. Lee, J. S. Park, D. J. Kim et al., "Ferroelectric properties of Mn-doped BiFeO_3 thin films," *Current Applied Physics*, vol. 11, no. 3, supplement, pp. S189–S192, 2011.
- [13] T. Kawae, Y. Terauchi, H. Tsuda, M. Kumeda, and A. Morimoto, "Improved leakage and ferroelectric properties of Mn and Ti codoped BiFeO_3 thin films," *Applied Physics Letters*, vol. 94, no. 11, Article ID 112904, 2009.
- [14] B. Huang, K. N. Ishihara, and P. H. Shingu, "Metastable phases of Al–Fe system by mechanical alloying," *Materials Science and Engineering A*, vol. 231, no. 1–2, pp. 72–79, 1997.
- [15] J. P. Crocombette, M. Pollak, F. Jollet, N. Thromat, and M. Gautier-Soyer, "X-ray-absorption spectroscopy at the Fe $L_{2,3}$ threshold in iron oxides," *Physical Review B*, vol. 52, no. 5, pp. 3143–3150, 1995.
- [16] G. Anjum, R. Kumar, S. Mollah, P. Thakur, S. Gautam, and K. H. Chae, "NEXAFS studies of $\text{La}_{0.8}\text{Bi}_{0.2}\text{Fe}_{1-x}\text{Mn}_x\text{O}_3$ ($0.0 \leq x \leq 0.4$) multiferroic system using x-ray absorption spectroscopy," *Journal of Physics D*, vol. 44, no. 7, Article ID 075403, 2011.
- [17] R. L. Kurtz and V. E. Henrich, "Surface electronic structure and chemisorption on corundum transition-metal oxides: V_2O_3 ," *Physical Review B*, vol. 28, no. 12, pp. 6699–6706, 1983.
- [18] R. Sæterli, S. M. Selbach, P. Ravindran, T. Grande, and R. Holmestad, "Electronic structure of multiferroic BiFeO_3 and related compounds: electron energy loss spectroscopy and density functional study," *Physical Review B*, vol. 82, no. 6, Article ID 064102, 2010.
- [19] R. Ramesh, J. Wang, J. B. Neaton et al., "Epitaxial BiFeO_3 multiferroic thin film heterostructures," *Science*, vol. 299, no. 5613, pp. 1719–1722, 2003.
- [20] Q. Y. Xu, S. Q. Zhou, Z. Wen et al., "Magnetic characterization of $\text{Bi}(\text{Fe}_{1-x}\text{Mn}_x)\text{O}_3$," *Physics Letters A*, vol. 375, no. 8, pp. 1209–1212, 2011.
- [21] L. H. Yin, Y. P. Sun, F. H. Zhang et al., "Magnetic and electrical properties of $\text{Bi}_{0.8}\text{Ca}_{0.2}\text{Fe}_{1-x}\text{Mn}_x\text{O}_3$ ($0 \leq x \leq 0.5$)," *Journal of Alloys and Compounds*, vol. 488, no. 1, pp. 254–259, 2009.
- [22] M. Azuma, H. Kanda, A. A. Belik, Y. Shimakawa, and M. Takano, "Magnetic and structural properties of $\text{BiFe}_{1-x}\text{Mn}_x\text{O}_3$," *Journal of Magnetism and Magnetic Materials*, vol. 310, no. 2, pp. 1177–1179, 2007.
- [23] D. S. Rana, K. Takahashi, K. R. Mavani et al., "Thickness dependence of the structure and magnetization of BiFeO_3 thin films on $(\text{LaAlO}_3)_{0.3}(\text{Sr}_2\text{AlTaO}_6)_{0.7}$ (001) substrate," *Physical Review B*, vol. 75, no. 6, Article ID 060405, 2007.
- [24] J. B. Goodenough, "Theory of the role of covalence in the perovskite-type manganites $[\text{La},\text{M}(\text{II})]\text{MnO}_3$," *Physical Review*, vol. 100, no. 2, pp. 564–573, 1955.

Research Article

Effects of Annealing Temperature on Structure and Magnetic Properties of $Tb_xY_{3-x}Fe_5O_{12}$ ($x = 0.2$ and 0.4) Thin Films

N. B. Ibrahim, Ftema W. Aldbea, and Mustaffa Hj Abdullah

School of Applied Physics, Faculty of Science and Technology, Universiti Kebangsaan Malaysia, 43600 Bangi, Malaysia

Correspondence should be addressed to N. B. Ibrahim, baayah@ukm.my

Received 14 January 2012; Revised 15 February 2012; Accepted 29 March 2012

Academic Editor: Weichang Hao

Copyright © 2012 N. B. Ibrahim et al. This is an open access article distributed under the Creative Commons Attribution License, which permits unrestricted use, distribution, and reproduction in any medium, provided the original work is properly cited.

Terbium-substituted yttrium iron garnet ($Tb_xY_{3-x}Fe_5O_{12}$ ($x = 0.2$ and 0.4)) thin films have been successfully prepared by a sol-gel method followed by spin-coating process. The annealing of the films was performed at different temperatures like 700, 800, and 900°C and found that the films annealed at 900°C turned out to be crystallized into a pure garnet phase. All of the films were bearing grains of nanometer in size. Increasing the annealing temperature gave extra energy to the grains causing to be agglomerates. The lattice contraction occurred as the grain's sizes were decreased due to the decrease of Fe^{2+} formation. The magnetic measurements show that all of the films are soft magnetic materials with low saturation magnetization values. The hysteresis loops of the films which were annealed at 900°C were found angular in shape similar to the single crystal-like YIG film.

1. Introduction

Yttrium iron garnet ($Y_3Fe_5O_{12}$, YIG) and its rare-earth-substituted films have been progressively studied due to their wide potential applications, such as in telecommunication and magneto-optical devices [1]. Y site in YIG has been substituted with different materials such Bi, Ca, and Ce [2–4]. Bulk Tb-substituted YIG (Tb-YIG) has the potential in sensor application. However there are few published reports on it [5–7] and none of them report the material in the thin film form. Marins et al. [5] have reported that the magnetic properties of $Tb_{(3-x)}Y_xFe_5O_{12}$ powder calcined at 1000°C depend on the sintering temperature, and also the small coercive field value is related to the increased sintering temperature. Guillot et al. [6] have studied the magnetization of $Tb_xY_{3-x}Fe_5O_{12}$ in polycrystalline and single crystal form at magnetic field of 180 kOe. They found that, in case of the polycrystalline ($x = 2, 1, 0.37$), the compensation points depend on the Tb concentration while for the single crystals ($x = 2, 1, 0.37$) a strong magnetic anisotropy was observed with the change of easy direction of magnetization from [111] to [100] when x was decreased. They also reported occurrence of abrupt field-induced transitions at low temperature when the external field was applied along the [100] direction. Rodić et al. [7] reported that the compensation

temperature of $Tb_xY_{3-x}Fe_5O_{12}$ ($x = 1, 1.98, 2.5,$ and 3) powder was proportional to the concentration of the terbium ion.

This paper reports the preparation of $Tb_xY_{3-x}Fe_5O_{12}$ ($x = 0.2$ and 0.4) thin films by a cheap, and simple method, that is a sol-gel method followed by spin coating process. In order to obtain crystalline films, annealing process was employed. The effects of annealing temperature on the structures and magnetic properties of the films were studied.

2. Experimental Procedure

Yttrium (III) nitrate hexahydrate $Y(NO_3)_3 \cdot 6H_2O$ with 99.99% purity and iron (III) nitrate nanohydrate $Fe(NO_3)_3 \cdot 9H_2O$ with 98.0% purity were first dissolved in 2-methoxyethanol and refluxed at 80°C for 3 hours. The doping agent in the form of $Tb(COOCH_3)_3 \cdot H_2O$ with 99.9% purity was first dissolved in 1 mL acetic acid and then added to the yttrium and iron solution. The ratio of yttrium and terbium was altered in order to obtain $Tb_{0.2}Y_{2.8}Fe_5O_{12}$ and $Tb_{0.4}Y_{2.6}Fe_5O_{12}$ solution followed by addition of 1 mL distilled water and 3 mL of nitric acid. Diethylamine was added to the solution to obtain a pH 3 solution. The solution was again refluxed at 80°C for 3 hours.

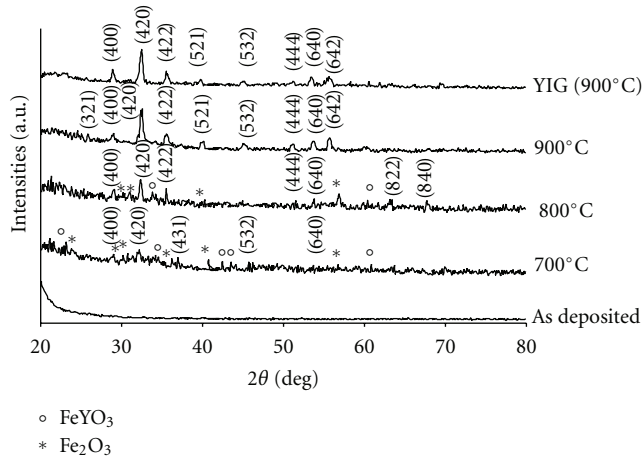


FIGURE 1: XRD spectrum for series 1 film.

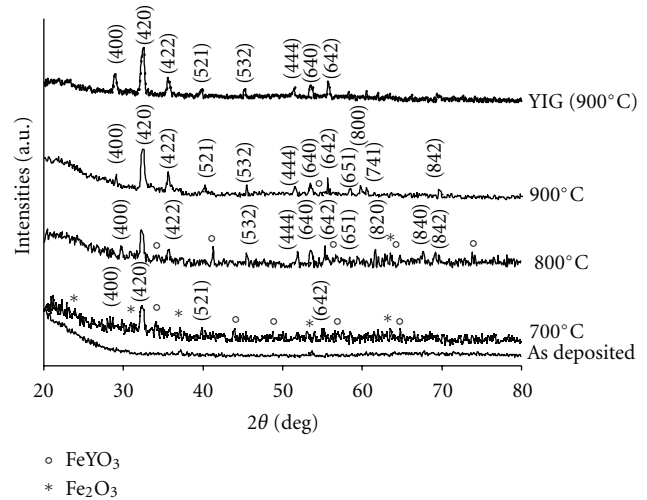


FIGURE 2: XRD spectrum for series 2 film.

To obtain the films, $25 \mu\text{L}$ of the gel was dropped onto a clean quartz substrate. Using a spin coater, the substrate was spin first at 500 rpm for 15 seconds, then at 3500 rpm for 30 seconds. The film was heated at 90°C for 2 hours to get rid of residual solvent, and followed by 350°C for 15 min at heating rate of $3^\circ\text{C}/\text{min}$ to burn-off the organic compounds. Then both $\text{Tb}_{0.2}\text{Y}_{2.8}\text{Fe}_5\text{O}_{12}$ and $\text{Tb}_{0.4}\text{Y}_{2.6}\text{Fe}_5\text{O}_{12}$ films were annealed at 700, 800 and 900°C in order to study the effect of the annealing temperature on their physical properties. The films were identified as series 1 for $\text{Tb}_{0.2}\text{Y}_{2.8}\text{Fe}_5\text{O}_{12}$ and series 2 for $\text{Tb}_{0.4}\text{Y}_{2.6}\text{Fe}_5\text{O}_{12}$ films.

An X-ray diffractometer (XRD) with $\text{Cu-K}\alpha$ radiation was used to study the film's structures and phases. A field emission scanning electron microscopy (FE SEM) was used to measure the grain's size and thicknesses of the films. A vibrating sample magnetometer (VSM) was used to study the in-plane magnetic properties of the films.

3. Results and Discussion

The XRD results in Figures 1 and 2 show that both series were crystallized into pure YIG phase after being annealed at 900°C . The films which were annealed at temperatures less than 900°C were displaying mixed phases of YIG, Fe_2O_3 , and YFeO_3 because of incomplete crystallization. No peaks belonging to Tb_2O_3 were found in the results, thus indicating the incorporation of Tb atoms in the garnet structure.

The lattice parameters for both series were calculated from the XRD spectra and Bradley and Jay's extrapolation method was employed to minimize the errors [8]. The lattice parameter value for each 2θ was obtained and a graph presenting the lattice parameter versus $\cos^2\theta$ was plotted. The extrapolated value at the y -axis was considered as the desired value. While the films annealed at 700 and 800°C were displaying mixed phases, only the 2θ of Tb-YIG was used to calculate the lattice parameter. Figure 3 shows the results for both series. The lattice parameter of both series was increased with the increase in annealing temperature. Similar results have also been reported for nanoparticle oxide system [9, 10].

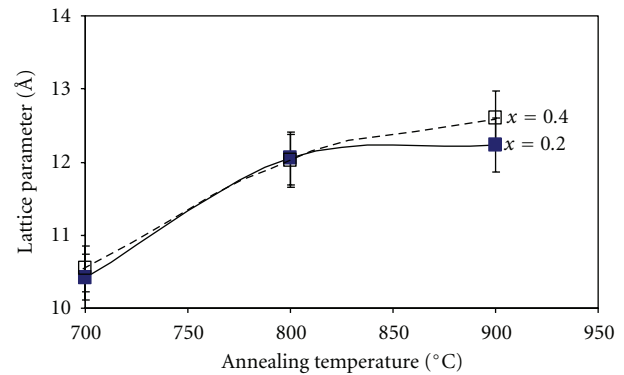


FIGURE 3: The plot of lattice parameter versus annealing temperature for series 1 and 2.

According to Rajendran et al. [11], oxygen vacancies can occur at the particle's surface during the film preparation and may cause the formation of Fe^{2+} . The oxygen vacancies could occur due to the preparation condition. The annealing processes were carried out in air; thus increasing the annealing temperature could promote the formation of Fe^{2+} ions. As Fe^{2+} ions are larger than Fe^{3+} , the increment of their formation will further expand the unit cell. To confirm this, XPS measurements were performed on the films annealed at 900°C . Figure 4 is clearly exhibiting the results confirming the formation of Fe^{2+} in both films.

The thickness of the films was measured from the film's cross section. The films were cut and the back scattered images from the cross sections were taken using the FESEM. Figure 5 shows the typical FESEM cross-section a micrograph of a Tb-YIG film showing different contrast of the film and substrate. Figure 6 shows that the thickness decreases as the temperature increases for series 1 ($x = 0.2$). The thinning of the films as the temperature increases could be due to the densification process, where the small empty spaces or pores were filled by the grains [12]. However for series 2 ($x = 0.4$), increasing annealing process from 700 to 800°C increases

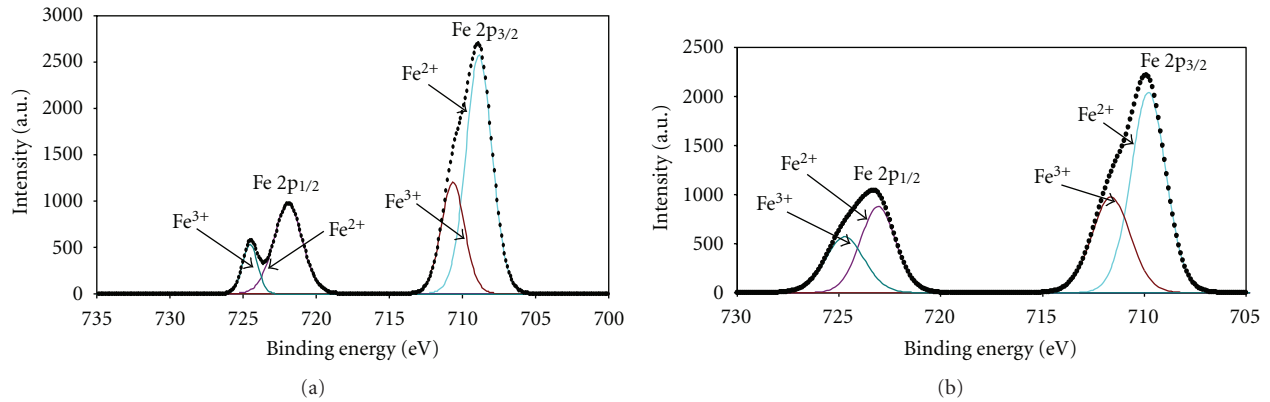


FIGURE 4: The XPS spectra for films annealed at 900°C.

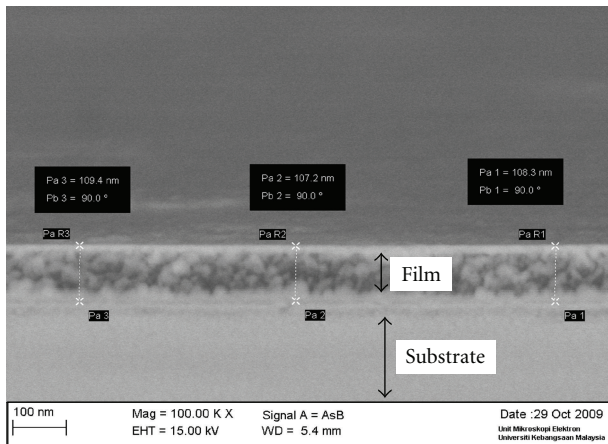


FIGURE 5: A typical cross-sectional view of a Tb-YIG film ($x = 0.2$) showing the contrast (back scattered electron) between the film and substrate.

the film thickness due to the increment of the grains (see Figure 8). Further temperature increment to 900°C decreases the film thickness due to the densification process.

The grains sizes were measured from the surface micrographs obtained from the FESEM. Figure 7 shows the FESEM micrographs of $\text{Tb}_{0.2}\text{Y}_{2.8}\text{Fe}_5\text{O}_{12}$ and $\text{Tb}_{0.4}\text{Y}_{2.6}\text{Fe}_5\text{O}_{12}$ films annealed at 900°C. The relation between grain size and annealing temperature is shown in Figure 8. All of the films have grains sizes in nanometer range (9–60 nm). Both series show a similar graph pattern. The grains become larger as the annealing temperature increases. The nanometer size grains possess large overall surface area which means that their total surface energy is also high. However the energy can be minimized when the annealing process was carried out, thus allowing the grains to agglomerate. Further increasing the annealing temperature reduced the surface energy of the grains and thus allowed them to become more agglomerate.

The VSM was used to measure the in-plane magnetic properties of both series at room temperature (25°C). No demagnetization corrections were required as the films were very thin compared to the lateral dimensions; hence the

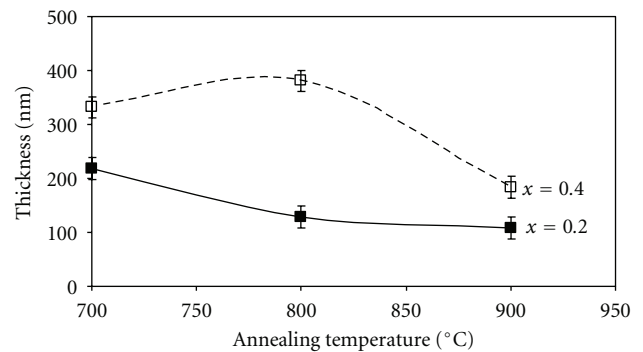
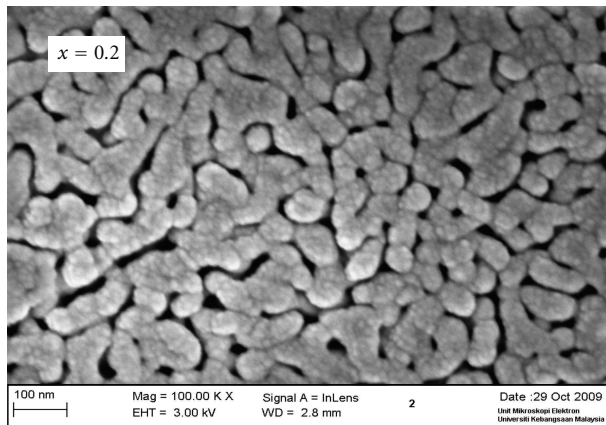
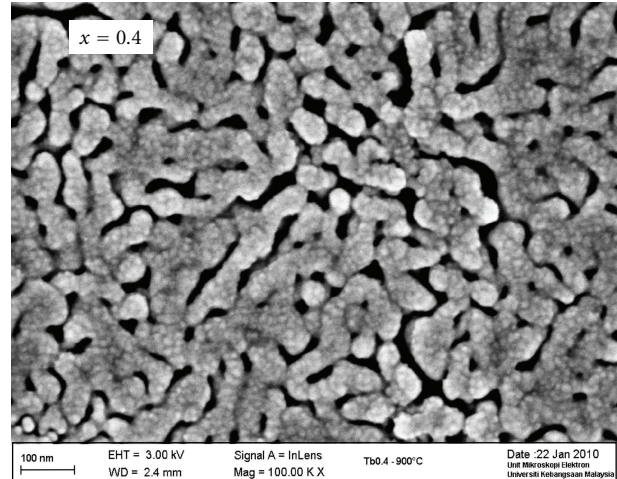


FIGURE 6: The relation between film thickness and annealing temperature for series 1 and 2.

in-plane demagnetization was leaned towards zero. However the linear ramp due to the paramagnetic quartz substrate was subtracted from the data. Figures 9 and 10 show the hysteresis loops of series 1 and 2, respectively. The samples are soft magnetic materials with low saturation magnetization (M_s) values. Also the films annealed at 900°C show angular shape hysteresis loops which are similar to those reported by Ibrahim et al. [4] for their single crystal-like YIG film. Their film's easy axis does not lie in the film plane. The angular hysteresis shows that it is possible to magnetize in-plane up to certain limit (M_{easy}) by growth of easy domains giving the initial steep region. Further magnetization would need rotation away from the easy directions giving the second stage which is the harder process. As shown in Figure 11 the M_s of both series increase with the annealing temperature. $\text{Tb}_{0.2}\text{Y}_{2.8}\text{Fe}_5\text{O}_{12}$ and $\text{Tb}_{0.4}\text{Y}_{2.6}\text{Fe}_5\text{O}_{12}$ films annealed at 700 and 800°C have similar M_s ; the low values of magnetization could be due to the existence of the antiferromagnetic Fe_2O_3 phase in the samples. Increasing the annealing temperature improves the film crystallization and thus increases the M_s ; however it is lower than 138.3 emu/cm³ for YIG film containing micrometer grain size range [13]. Similar reduction has also been reported by Sánchez et al. for their nanograin YIG. Nanograin YIG possesses high surface-to-volume ratio; thus increasing the surface spin effects the films [14].



(a)



(b)

FIGURE 7: FESEM micrographs of $Tb_{0.2}Y_{2.8}Fe_5O_{12}$ and $Tb_{0.4}Y_{2.6}Fe_5O_{12}$ films, annealed at $900^\circ C$.

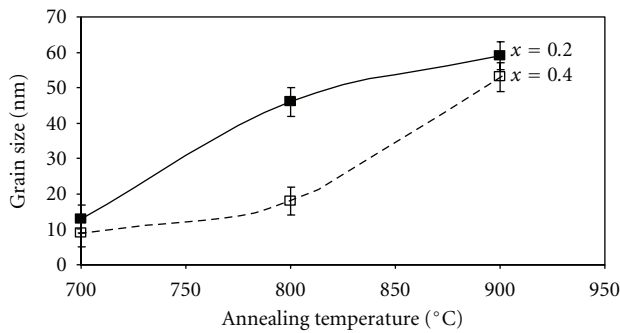


FIGURE 8: The relation between particle size and annealing temperature for series 1 and 2.

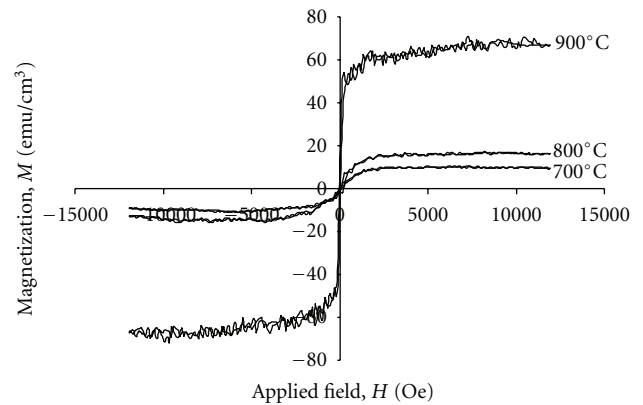


FIGURE 10: The hysteresis loop of series 2.

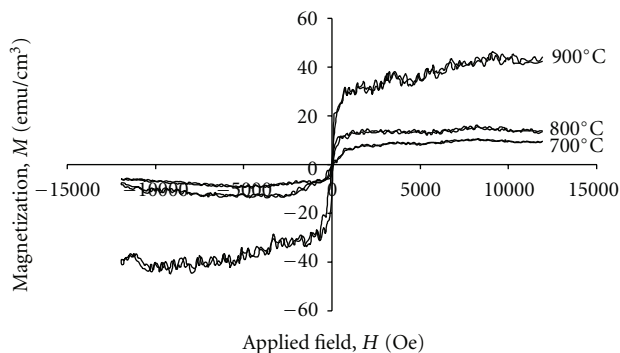


FIGURE 9: The hysteresis loop of series 1.

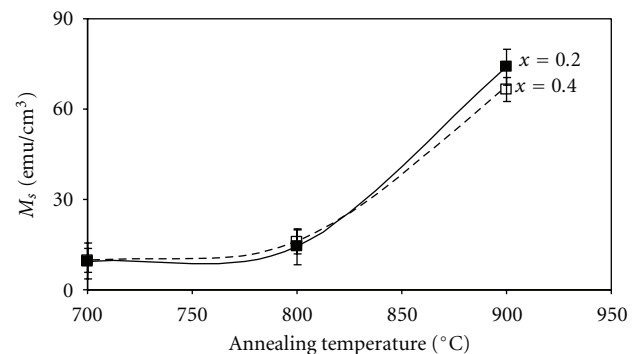


FIGURE 11: The plot of M_s versus annealing temperature of both series.

Figure 12 shows the plot of coercivity field (H_c) versus annealing temperature of both series. It can be clearly seen that both series show similar trends. The H_c becomes smaller as the annealing temperature increases. As measured from the FE SEM images, the increment in annealing temperature led to bigger grain sizes. Theoretically it has been proved that the coercivity of small particle (H_c) is proportional to $1/L^v$

(L is the particle size and v is a constant that lies between 1/2 and 1) [15]. The increment of grain size with the annealing temperature also reduced the strain in the films resulting in reducing the H_c values.

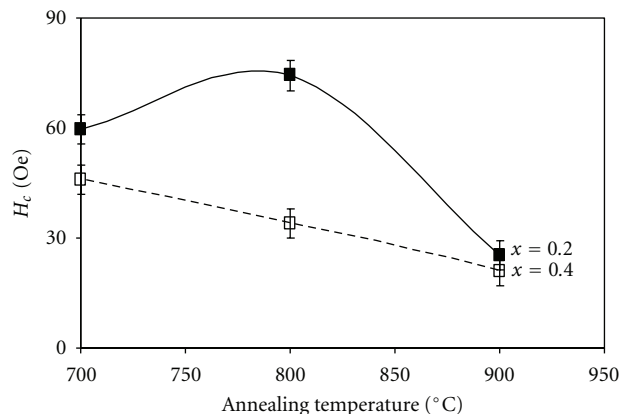


FIGURE 12: The plot of H_c versus annealing temperature of both series.

4. Conclusion

The structure and magnetic properties of $Tb_{0.2}Y_{2.8}Fe_5O_{12}$ and $Tb_{0.4}Y_{2.6}Fe_5O_{12}$ films prepared onto quartz substrates by a sol-gel method followed by spin-coating process have been reported. The films subjected to the annealing temperature of 900°C were found to be crystallized into pure garnet phase. The films have grains sizes in the range of 9–60 nm. Increment in the annealing temperature from 700 to 900°C led to the increased formation of Fe^{2+} . The films annealed at 900°C show hysteresis loops similar to the single crystal-like YIG. Although the substitution of Tb ions into YIG films reduced their M_s values, the films have potential in microwave application due to their low coercivity values and soft magnetic nature.

Acknowledgments

This work was supported by Malaysian Ministry of Science, Technology and Innovation via science fund Grant 03-01-02-SF0538. The authors would like to thank Mr. Mohamad Azri Tukimon for XPS analysis and Mr. Mohamad Hasnul Naim for FE-SEM measurements.

References

- [1] R. Shaiboub, N. B. Ibrahim, M. Abdullah, and F. Abdulhade, "The physical properties of erbium-doped yttrium iron garnet films prepared by sol-gel method," *Journal of Nanomaterials*, vol. 2012, Article ID 524903, 5 pages, 2012.
- [2] Q. Yang, H. Zhang, and Y. Liu, "Study of magnetic and magneto-optical properties of heavily doped bismuth substitute yttrium iron garnet (Bi:YIG) film," *Rare Metals*, vol. 25, no. 6, pp. 557–561, 2006.
- [3] Y. J. Song, G. B. Turpin, R. E. Bornfreund, H. Aoyama, and P. E. Wigen, "Effects of oxygen vacancies on the magnetic and electrical properties of Ca-substituted yttrium iron garnet," *Journal of Magnetism and Magnetic Materials*, vol. 154, no. 1, pp. 37–53, 1996.

- [4] N. B. Ibrahim, C. Edwards, and S. B. Palmer, "Pulsed laser ablation deposition of yttrium iron garnet and cerium-substituted YIG films," *Journal of Magnetism and Magnetic Materials*, vol. 220, no. 2, pp. 183–194, 2000.
- [5] S. D. S. Marins, T. Ogasawara, and A. S. Ogasawara, "Terbium-yttrium-iron garnet revisited," *Journal of Alloys and Compounds*, vol. 436, no. 1-2, pp. 415–420, 2007.
- [6] M. Guillot, A. Marchand, J. M. Desvignes, H. Le Gall, T. Merceron, and M. Guillaud, "High magnetic field properties of mixed terbium-yttrium ferrite garnets," *Zeitschrift für Physik B Condensed Matter*, vol. 74, no. 3, pp. 335–339, 1989.
- [7] D. Rodić, A. Szytuła, Z. Tomkowicz, M. Guillot, and H. Le Gall, "Temperature dependence of lattice constants and thermal expansion coefficient of terbium-yttrium ferrites garnets," *Journal of Magnetism and Magnetic Materials*, vol. 75, no. 1-2, pp. 79–87, 1988.
- [8] V. K. Percharksky and P. Y. Zavalij, *Fundamenta of Powder Diffraction and Structural Characterization of Metals*, Springer, New York, NY, USA, 2009.
- [9] P. Ayyub, M. Multani, and R. Vijayaraghavan, "Anomalous behaviour of the magnetic hyperfine field in the microcrystalline $YFeO_3$ - Fe_2O_3 mixed phase system," *Physics Letters A*, vol. 119, no. 2, pp. 95–99, 1986.
- [10] P. Ayyub, M. Multani, M. Barma, V. R. Palka, and R. Vijayaraghavan, "Size-induced structural phase transitions and hyperfine properties of microcrystalline Fe_2O_3 ," *Journal Physics C*, vol. 21, article 2229, 1988.
- [11] M. Rajendran, S. Deka, P. A. Joy, and A. K. Bhattacharya, "Size-dependent magnetic properties of nanocrystalline yttrium iron garnet powders," *Journal of Magnetism and Magnetic Materials*, vol. 301, no. 1, pp. 212–219, 2006.
- [12] M. P. Bole and D. S. Patil, "Effect of annealing temperature on the optical constants of zinc oxide films," *Journal of Physics and Chemistry of Solids*, vol. 70, no. 2, pp. 466–471, 2009.
- [13] T. Boudiar, B. Payet-Gervy, M. F. Blanc-Mignon, J. J. Rousseau, M. Le Berre, and H. Joisten, "Magneto-optical properties of yttrium iron garnet (YIG) thin films elaborated by radio frequency sputtering," *Journal of Magnetism and Magnetic Materials*, vol. 284, no. 1–3, pp. 77–85, 2004.
- [14] R. D. Sánchez, J. Rivas, P. Vaqueiro, M. A. López-Quintela, and D. Caeiro, "Particle size effects on magnetic properties of yttrium iron garnets prepared by a sol-gel method," *Journal of Magnetism and Magnetic Materials*, vol. 247, no. 1, pp. 92–98, 2002.
- [15] G. Rowlands, "The variation of coercivity with particle size," *Journal of Physics D*, vol. 9, no. 8, article 013, pp. 1267–1269, 1976.

Research Article

Dilute Magnetic Semiconductor $\text{Cu}_2\text{FeSnS}_4$ Nanocrystals with a Novel Zincblende Structure

Xiaolu Liang,^{1,2} Xianhua Wei,¹ and Daocheng Pan²

¹ State Key Laboratory Cultivation Base for Nonmetal Composites and Functional Materials, Southwest University of Science and Technology, Mianyang 621010, China

² State Key Laboratory of Rare Earth Resource Utilization, Changchun Institute of Applied Chemistry, Chinese Academy of Sciences, 5625 Renmin Street, Changchun 130022, China

Correspondence should be addressed to Xianhua Wei, weisansao@yahoo.com.cn and Daocheng Pan, pan@ciac.jl.cn

Received 15 February 2012; Revised 13 April 2012; Accepted 17 April 2012

Academic Editor: Weichang Hao

Copyright © 2012 Xiaolu Liang et al. This is an open access article distributed under the Creative Commons Attribution License, which permits unrestricted use, distribution, and reproduction in any medium, provided the original work is properly cited.

Diluted magnetic semiconductor $\text{Cu}_2\text{FeSnS}_4$ nanocrystals with a novel zincblende structure have been successfully synthesized by a hot-injection approach. Cu^+ , Fe^{2+} , and Sn^{4+} ions occupy the same position in the zincblende unit cell, and their occupancy possibilities are 1/2, 1/4, and 1/4, respectively. The nanocrystals were characterized by means of X-ray diffraction (XRD), transmission electron microscopy (TEM), selected area electron diffraction (SAED), energy-dispersive spectroscopy (EDS), and UV-vis-NIR absorption spectroscopy. The nanocrystals have an average size of 7.5 nm and a band gap of 1.1 eV and show a weak ferromagnetic behavior at low temperature.

1. Introduction

During the past three decades, transition metal ion-doped diluted magnetic semiconductors (DMSs) have attracted great interest because of their outstanding the optical, electronic, and magnetic properties [1–5]. Fe^{2+} , Ni^{2+} , Mn^{2+} , and Co^{2+} are commonly used as intentional impurities and incorporated in group II-VI and III-V semiconductors; ZnO, ZnS, ZnSe, CdS, CdSe, and GaN are the frequently used host materials [6–8]. However, the magnetic ion concentration in these doped DMS nanocrystals is generally less than 2 mol% [9–13]. It is well known that the magnetic properties of DMSs are strongly dependent on the magnetic ion concentration. Nonetheless, a high magnetic ion concentration is detrimental to the magnetic properties for binary DMSs due to the strong antiferromagnetic (AFM) interactions between nearest-neighbor-doping ions [14].

The quaternary $\text{Cu}_2\text{FeSnS}_4$ with a high magnetic ion concentration is being considered as an ideal material for avoiding large AFM exchange interactions [14]. However, $\text{Cu}_2\text{FeSnS}_4$ usually crystallizes in a stannite structure (space group *I-42m*, no. 121), and Cu^+ , Fe^{2+} , and Sn^{4+} cations have a fixed position in the stannite unit cell [15]. In the previously reports, quaternary $\text{Cu}_2\text{FeSnS}_4$ magnetic semiconductor

with a stannite structure exhibited an antiferromagnetic behavior with a Néel temperature (T_N) of 6~8 K [15–17]. To the best of our knowledge, there are no reports on the synthesis of $\text{Cu}_2\text{FeSnS}_4$ nanocrystals with a zincblende structure in the literature. In this paper, we adopted a hot-injection approach to synthesize quaternary $\text{Cu}_2\text{FeSnS}_4$ nanocrystals with a metastable zincblende structure. In zincblende structure, all of cations have a random distribution instead of ordered distribution, which may lead peculiar magnetic properties by controlling both metal distribution and metal-metal distance. The magnetic properties of zincblende $\text{Cu}_2\text{FeSnS}_4$ nanocrystals were investigated by a superconducting quantum interference device (SQUID).

2. Experimental

2.1. Chemicals. $\text{CuCl}_2 \cdot 2\text{H}_2\text{O}$, $\text{FeCl}_3 \cdot 6\text{H}_2\text{O}$, $\text{SnCl}_4 \cdot 5\text{H}_2\text{O}$, sulfur powder (99.999%), thiourea, and oleylamine (OM, 80% ~ 90%) were purchased from Aladdin Inc. All chemicals were used as received.

2.2. Preparation of Sulfur Precursors. 1.0 M S/OM solution was prepared by dissolving 0.64 g (20 mmol) of sulfur powder in 20.0 mL of OM at 120°C.

2.3. Synthesis of Zincblende $\text{Cu}_2\text{FeSnS}_4$ Nanocrystals. In a typical synthesis, 17.0 mg (0.1 mmol) of $\text{CuCl}_2 \cdot 2\text{H}_2\text{O}$, 17.0 mg (0.05 mmol) of $\text{SnCl}_4 \cdot 5\text{H}_2\text{O}$, 13.5 mg (0.05 mmol) of $\text{FeCl}_3 \cdot 6\text{H}_2\text{O}$, and 5.0 mL of OM were added to a 50 mL three-neck flask, and the reaction mixture was heated to 120°C . The inside of the flask was degassed by a vacuum pump for 10 min, and argon gas was charged. This procedure was repeated three times. Then the temperature was increased to 270°C , and 0.5 mL of S/OM solution was injected into the flask. After 30 min, the crude solution was cooled to 60°C and then precipitated with 30 mL of ethanol. Finally, the nanocrystals were dispersed in toluene.

2.4. Characterization. X-ray diffraction (XRD) patterns were recorded by a Bruker D8 FOCUS X-ray diffractometer using $\text{Cu K}\alpha$ radiation, and the accelerating voltage and current were 40 kV and 40 mA, respectively. UV-vis-NIR absorption spectrum was measured by Shimadzu UV-3600. Transmission electron microscopy (TEM) and selected area electron diffraction (SAED) images were taken on a FEI Tecnai G2 F20 with an accelerating voltage of 200 kV. Energy dispersive X-ray spectroscopy (EDS) spectrum was obtained by using a scanning electron microscope (Hitachi S-4800) equipped with a Bruker AXS XFlash detector 4010. The magnetization of $\text{Cu}_2\text{FeSnS}_4$ nanocrystals was obtained by SQUID (MPMS-XL-7, Quantum Design, Ltd.) between 2 and 100 K using zero-field-cooled (ZFC) and field-cooling (FC) procedures in an applied field of 50 Oe.

3. Results and Discussion

In contrast to the tetragonal stannite structure, the space symmetry of zincblende structure significantly decreases by the random arrangement of Cu^+ , Fe^{2+} , and Sn^{4+} cations in the cubic zincblende unit cell of $\text{Cu}_2\text{FeSnS}_4$. As shown in the inset of Figure 1, the zincblende unit cell of $\text{Cu}_2\text{FeSnS}_4$ is completely the same as that of ZnS (space group $F-43m$, no. 216). Note that only Zn^{2+} position is replaced by $1/2 \text{Cu}^+$, $1/4 \text{Fe}^{2+}$, and $1/4 \text{Sn}^{4+}$. Figure 1 shows the XRD pattern for as-synthesized $\text{Cu}_2\text{FeSnS}_4$ nanocrystals. Obviously, our XRD pattern did not match those reported in the literature [15–17] and the standard JCPDS card database (stannite structure, JCPDS no. 44-1476). We therefore simulated the diffraction pattern for zincblende $\text{Cu}_2\text{FeSnS}_4$ and compared it with the experimental pattern. The simulated and experimental patterns match very well, signifying that these nanocrystals possess a zincblende structure with a space group $F-43m$ and unit cell parameter $a = 5.429 \text{ \AA}$. In addition, the zincblende structure of $\text{Cu}_2\text{FeSnS}_4$ nanocrystals can be further confirmed by SAED image Figure 2(b). It should be noted that the lattice parameters of zincblende $\text{Cu}_2\text{FeSnS}_4$ nanocrystals measured from SAED images are very close to those calculated from the XRD patterns.

Low-resolution TEM image of zincblende $\text{Cu}_2\text{FeSnS}_4$ nanocrystals is shown in Figure 2(c). The $\text{Cu}_2\text{FeSnS}_4$ nanocrystals are nearly spherical in shape and have the average diameter of 7.5 nm. In addition, the nanocrystals exhibit a very narrow size distribution and have a standard

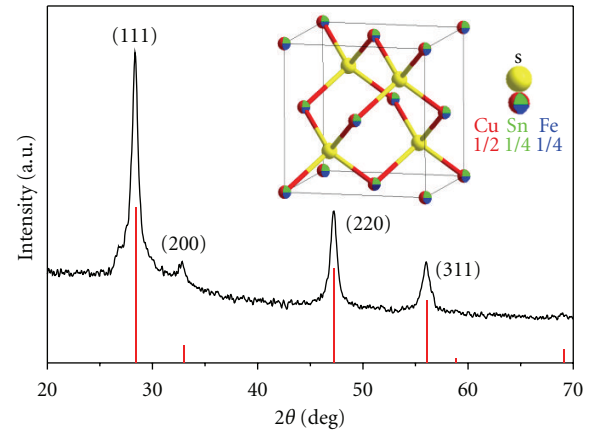


FIGURE 1: The simulated (red line) and experimental (black line) XRD patterns of $\text{Cu}_2\text{FeSnS}_4$ nanocrystals with a zincblende structure; the inset is the unit cell of zincblende $\text{Cu}_2\text{FeSnS}_4$.

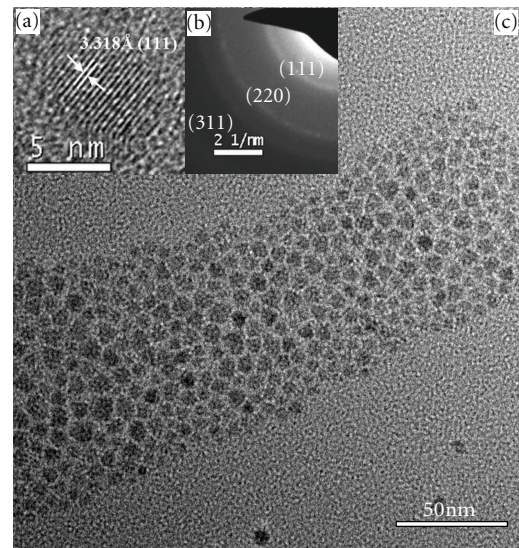


FIGURE 2: TEM (a and c) and SAED (b) images of $\text{Cu}_2\text{FeSnS}_4$ nanocrystals.

deviation of 7.4%. The high-resolution TEM image clearly revealed the continuous lattice fringes, and the calculated d spacing corresponding to (111) plane is 3.138 \AA , which is in good agreement with that value determined by XRD pattern (3.136 \AA) or SAED image (3.140 \AA).

Figure 3(a) displays UV-vis-NIR absorption spectrum of as-synthesized $\text{Cu}_2\text{FeSnS}_4$ nanocrystals. We calculated the optical band gap (E_g) by extrapolating the linear portion of the absorption spectrum to $h\nu$ axis, and the calculated optical band gaps for $\text{Cu}_2\text{FeSnS}_4$ nanocrystals are around 1.1 eV. As demonstrated in Figure 3(b), the chemical composition of the nanocrystals is $\text{Cu}_2\text{FeSnS}_4$. The molar ratio of Cu/Fe/Sn/S is close to 2 : 1 : 1 : 4, which is well consistent with stoichiometric composition of $\text{Cu}_2\text{FeSnS}_4$.

The magnetic properties of $\text{Cu}_2\text{FeSnS}_4$ nanocrystals were characterized by a SQUID magnetometer. As shown in Figure 4(a), a clear separation between the ZFC and FC curves is observed at low temperature region which indicates

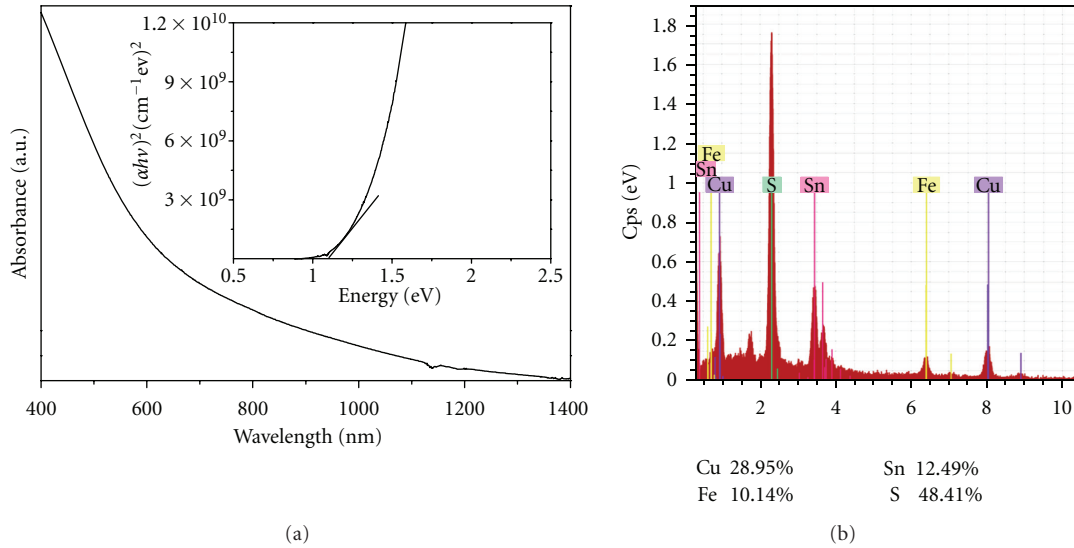


FIGURE 3: UV-vis-NIR absorption (a) and EDS (b) spectra of $\text{Cu}_2\text{FeSnS}_4$ nanocrystals.

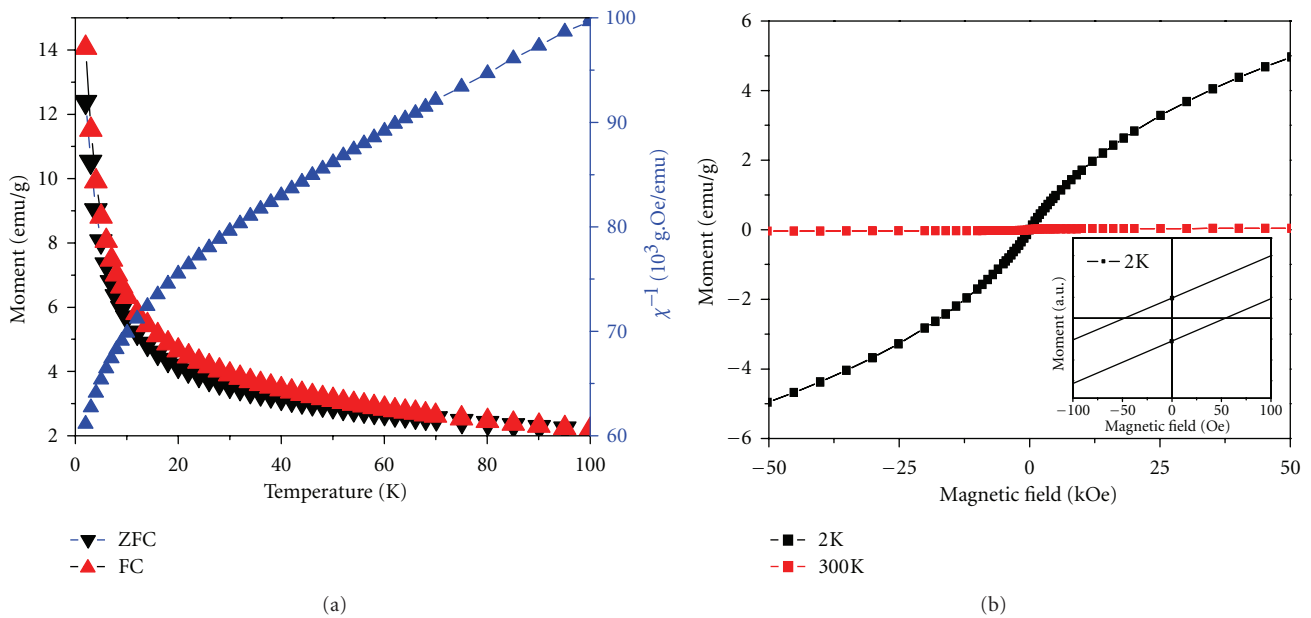


FIGURE 4: (a) Temperature dependence of the magnetization for $\text{Cu}_2\text{FeSnS}_4$ nanocrystals. (b) The field dependence of the magnetization for $\text{Cu}_2\text{FeSnS}_4$ nanocrystals at 2 k and 300 k; inset: the magnification of the hysteresis loop at 2 K.

the absence of a magnetic ordering transition. The plot of $\chi^{(-1)-T}$ (blue line in Figure 4(a)) indicates classical Curie-Weiss behavior of this sample at high temperature region. The magnetic susceptibility, $\chi(T)$, at the high-temperature limit can be represented by the Curie-Weiss law, $\chi(T) = C/(T - \Theta)$, where C is the Curie constant, T is the temperature in Kelvin, and Θ is the Curie temperature. The isothermal magnetization curves of $\text{Cu}_2\text{FeSnS}_4$ nanocrystals at 2 k and 300 k in magnetic fields up to ± 50 kOe are shown in Figure 4(b). The “s” shape hysteresis loop at 2 K is shown in the inset of Figure 4(b), with a coercive force of 56 Oe and relatively large residual magnetization. It can be concluded that these $\text{Cu}_2\text{FeSnS}_4$ nanocrystals exhibit ferromagnetic

behavior at this temperature. The hysteresis loop obtained at 300 K does not show hysteresis behavior and is weakly field dependent and linear, indicating that the nanocrystals become a paramagnetic material at 300 K. Note that the stannite $\text{Cu}_2\text{FeSnS}_4$ usually exhibited an antiferromagnetic behavior in the literatures [15–17]. It is well known that the unit cell parameter is 2.91 \AA in iron which shows ferromagnetic behavior. In the stannite $\text{Cu}_2\text{FeSnS}_4$, the interaction Fe-Fe could be super-exchange interaction with the aid of nonmagnetic ions due to the large nearest distance of Fe-Fe (5.45 \AA). However, the nearest distance of Fe-Fe is only 3.86 \AA in the zincblende $\text{Cu}_2\text{FeSnS}_4$ nanocrystals, and the electron clouds overlap of Fe-Fe is more larger than that

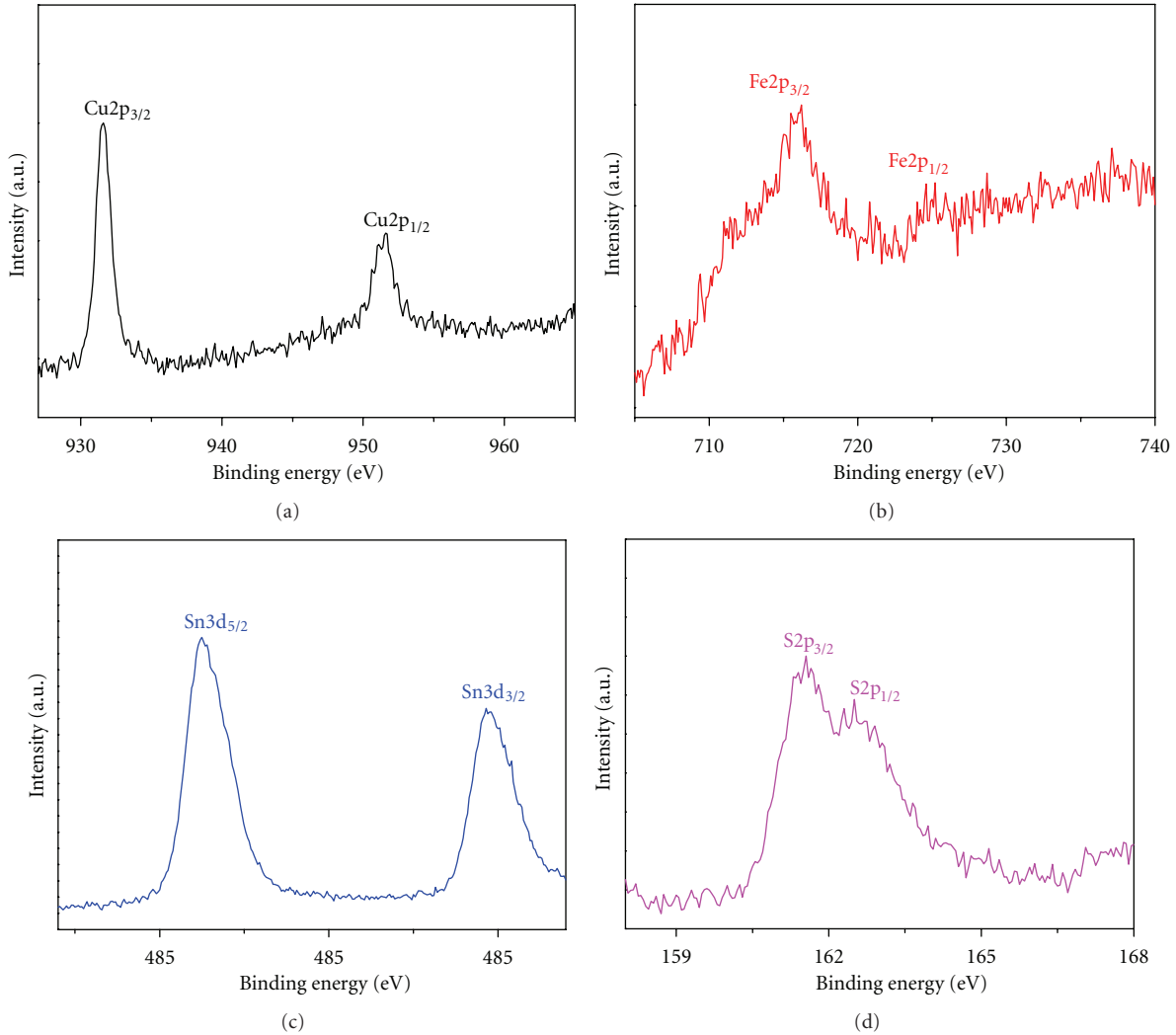


FIGURE 5: The X-ray photoelectron spectroscopy (XPS) spectra of as-synthesized $\text{Cu}_2\text{FeSnS}_4$ nanocrystals; (a) Cu2p; (b) Fe2p; (c) Sn3d; (d) S2p.

of stannite $\text{Cu}_2\text{FeSnS}_4$, enabling the exchange interaction at low temperature. As a result, $\text{Cu}_2\text{FeSnS}_4$ nanocrystals with a zincblende structure exhibit a ferromagnetic behavior.

In addition, X-ray photoelectron spectroscopy (XPS) was applied to determine the chemical composition and valence states of $\text{Cu}_2\text{FeSnS}_4$ nanocrystals. In Figure 5(a), the Cu 2p core splits into 2p_{3/2} (931.6 eV) and 2p_{1/2} (951.6 eV) peaks, which are characteristic of Cu^+ . Two peaks of Fe2p and Sn3d, located at 716.0 eV and 725.7 eV, 486.4 eV and 494.7 eV, suggesting that the valence states of Fe and Sn ions in the nanocrystals are +2 and +4, respectively.

4. Conclusion

In summary, dilute magnetic semiconductor $\text{Cu}_2\text{FeSnS}_4$ nanocrystals with a novel zincblende structure have been successfully synthesized. The optical and magnetic properties were characterized, and the nanocrystals have a band gap of 1.1 eV and exhibited a ferromagnetic behavior at low temperature. The ferromagnetic properties may be attributed to

the novel zincblende structure; that is, Cu^+ , Fe^{2+} , and Sn^{4+} ions occupy the same site in the unit cell and have a random distribution. Moreover, these dispersible and low-cost DMS nanocrystals have a high potential for thin film solar cells, spintronics, magnetic switching, magnetic recording, and Li-ion batteries.

Acknowledgments

This work was supported by the National Natural Science Foundation of China (Grant nos. 21071142 and 51172229), the Fund for Creative Research Groups (Grant no. 20921002), and the Natural Science Foundation for Young Scientists of Jilin Province (20100105).

References

- [1] D. J. Norris, A. L. Efros, and S. C. Erwin, "Doped nanocrystals," *Science*, vol. 319, no. 5871, pp. 1776–1779, 2008.

- [2] D. J. Norris, N. Yao, F. T. Charnock, and T. A. Kennedy, "High-quality manganese-doped ZnSe nanocrystals," *Nano Letters*, vol. 1, no. 1, pp. 3–7, 2001.
- [3] J. Zheng, X. Yuan, M. Ikezawa et al., "Efficient photoluminescence of Mn^{2+} ions in MnS/ZnS core/shell quantum dots," *Journal of Physical Chemistry C*, vol. 113, no. 39, pp. 16969–16974, 2009.
- [4] Y. Zhang, C. Gan, J. Muhammad, D. Battaglia, X. Peng, and M. Xiao, "Enhanced fluorescence intermittency in Mn-doped single ZnSe quantum dots," *Journal of Physical Chemistry C*, vol. 112, no. 51, pp. 20200–20205, 2008.
- [5] H. Kim, M. Achermann, L. P. Balet, J. A. Hollingsworth, and V. I. Klimov, "Synthesis and characterization of Co/CdSe core/shell nanocomposites: bifunctional magnetic-optical nanocrystals," *Journal of the American Chemical Society*, vol. 127, no. 2, pp. 544–546, 2005.
- [6] J. K. Furdyna, "Diluted magnetic semiconductors," *Journal of Applied Physics*, vol. 64, no. 4, pp. R29–R64, 1988.
- [7] N. Pradhan, D. M. Battaglia, Y. Liu, and X. Peng, "Efficient, stable, small, and water-soluble doped ZnSe nanocrystal emitters as non-cadmium biomedical labels," *Nano Letters*, vol. 7, no. 2, pp. 312–317, 2007.
- [8] I. Sarkar, M. K. Sanyal, S. Kar et al., "Ferromagnetism in zinc sulfide nanocrystals: dependence on manganese concentration," *Physical Review B*, vol. 75, no. 22, Article ID 224409, 2007.
- [9] M. L. Reed, M. K. Ritums, H. H. Stadelmaier et al., "Room temperature magnetic (Ga,Mn)N: a new material for spin electronic devices," *Materials Letters*, vol. 51, no. 6, pp. 500–503, 2001.
- [10] Y. M. Kim, M. Yoon, I. W. Park, Y. J. Park, and J. H. Lyou, "Synthesis and magnetic properties of $Zn_{1-x}Mn_xO$ films prepared by the sol-gel method," *Solid State Communications*, vol. 129, no. 3, pp. 175–178, 2004.
- [11] Z. Deng, L. Tong, M. Flores et al., "High-quality manganese-doped zinc sulfide quantum rods with tunable dual-color and multiphoton emissions," *Journal of the American Chemical Society*, vol. 133, no. 14, pp. 5389–5396, 2011.
- [12] Y. W. Jun, J. H. Lee, J. S. Choi, and J. Cheon, "Symmetry-controlled colloidal nanocrystals: nonhydrolytic chemical synthesis and shape determining parameters," *Journal of Physical Chemistry B*, vol. 109, no. 31, pp. 14795–14806, 2005.
- [13] K. M. Hanif, R. W. Meulenberg, and G. F. Strouse, "Magnetic ordering in doped $Cd_{1-x}Co_xSe$ diluted magnetic quantum dots," *Journal of the American Chemical Society*, vol. 124, no. 38, pp. 11495–11502, 2002.
- [14] T. Fries, Y. Shapira, F. Palacio et al., "Magnetic ordering of the antiferromagnet Cu_2MnSnS_4 from magnetization and neutron-scattering measurements," *Physical Review B*, vol. 56, no. 9, pp. 5424–5431, 1997.
- [15] A. Caneschi, C. Cipriani, F. Di Benedetto, and R. Sessoli, "Characterisation of the antiferromagnetic transition of Cu_2FeSnS_4 the synthetic analogue of stannite," *Physics and Chemistry of Minerals*, vol. 31, no. 3, pp. 190–193, 2004.
- [16] G. P. Bernardini, D. Borrini, A. Caneschi et al., "EPR and SQUID magnetometry study of Cu_2FeSnS_4 (stannite) and Cu_2ZnSnS_4 (kesterite)," *Physics and Chemistry of Minerals*, vol. 27, no. 7, pp. 453–461, 2000.
- [17] U. Ganiel, E. Hermon, and S. Shtrikman, "Studies of magnetic ordering in Cu_2FeSnS_4 by Mossbauer-spectroscopy," *Journal of Physics and Chemistry of Solids*, vol. 33, pp. 1873–1878, 1972.